Flamelet modelling of soot formation in diffusion flames

Dederichs, Anne Simone

2004

Flamelet Modelling of
Soot Formation in
Diffusion Flames

Anne S. Dederichs

Department of Fire Safety Engineering
Lund Institute of Technology

Doctoral thesis

Lund 2004

Ecce Homo

Ja, ich weiss, woher ich stamme!
Ungesättigt gleich der Flamme
Glühe und verzehr ich mich.
Licht wird alles, was ich fasse,
Kohle alles was ich lasse:
Flamme bin ich sicherlich!

Friedrich Nietzsche

Abstract

In this work the steady and unsteady flamelet models have been applied to soot formation in laminar and turbulent diffusion flames. The aim was to study how different model parameters affect soot formation in diffusion flames. It was shown that certain assumptions are more crucial in laminar diffusion flames than in turbulent ones. The soot formation in turbulent diffusion flames is more sensitive to the surface dependence of the particle and altering the active site parameter, than in laminar flames. This is due to the fact that the flame is laminar and the turbulent mixing, which supplies the particle with radicals, does not affect the process. The active site parameter decreases in the absence of radicals [1]. The modelling of complex diffusivity of all species is more relevant in laminar diffusion flames than in turbulent diffusion flames. All transient effects investigated in this work were shown to affect soot formation, which is itself transient. It was shown that these effects are more relevant for laminar flames than for turbulent flames. The steady flamelet model allows the inclusion of many transient processes and thereby loses in accuracy compared with the unsteady model. Finally, the process of the formation of agglomerates was included in the unsteady model and it was shown that the soot volume fraction is affected when this process is considered.

Contents

Nomenclature

c	mol/m^3	Molar concentration
c_p	$J/kg\ K$	Heat capacity
d	m	Particle diameter
$d*$	m	Critical particle diameter
D	m^2/s	Diffusion
D^f	$-$	Fractal dimension
E	J/mol	Activation energy
f	$-$	Branching coefficient
f_V	$m^3/(m^3)$	Soot volume fraction
g	$-$	Termination coefficient
g_0	$1/s$	Collapse of soot nucleus due to collision
h	kJ/kg	Enthalpy
I_I	W/m^2	Turbulence intensity
k_B	JK^{-1}	Bolzmann constant
$k_i,\ i = b, f$	(mol, s, m)	Reaction velocity of reaction i,
		backward (b) or forward (f) reaction
k_I	J	Turbulence kinetic energy
L	m	Macroscale, length of a vortex
		under laminar conditions
l_I	m	Integral scale,
		length of the largest turbulent vortex
l_λ	m	Taylor microscale
l_K	m	Kolmogorov microscale
M_r	$1/m^3$	Statistical moment of soot particles
		of rth order
$n_0(T)$	$1/s$	Rate of spontaneous formation of soot nuclei
N	$1/m^3$	Number density

PAH	−	Polyaromatic hydrocarbon
PSA	−	Particulate secondary aerosol
PM	−	Particulate matter
$[P_{i,j}]$	mol/m^3	PAH concentration of polymerization stage i and structure j
P_r	$1/m^3$	Statistical moment of primary soot particles of rth order
P	bar	Pressure
Q	-	conditional mean
r	m	Radius
R	$J/mol\ K$	Universal gas constant
S	m^2/m^3	Soot surface density
S_r	J/s	Radiation source
S_L	m/s	Laminar flame velocity
S_T	m/s	Turbulent flame velocity
S_Ψ	$1/s$	Source term of variable Ψ
t	s	Time
t_c	s	Chemical time scale
t_L	s	Laminar time scale
t_K	s	Kolomogrov time scale
t_I	s	Macroscopical time scale
TSI	−	Threshold sooting intensity
u	m/s	Velocity
$\overline{u}$	m/s	Reynolds averaged velocity
$\overline{u}$	m/s	Reynolds averaged velocity
u'	m/s	Reynolds velocity fluctuations
$u"$	m/s	Favre velocity fluctuations
$u'_{rms} = \sqrt{\overline{u'^2}}$	m/s	Velocity root mean square
u_K	m/s	Kolmogorov velocity
v'	m/s	Integral, fluctuation velocity
y	-	Fluctuation
Y	-	Temporal fluctuation
Y_i	kg/kg	Mass fraction for species i
X_i	mol/mol	Mole fraction for species i
$\mathbf{x} = (x_i, i = 1, 2, 3)$	m	Spatial vector
x_i	m	Spatial coordinate
Z	−	Mixture fraction
$\tilde{Z}$	−	Mean of the mixture fraction
$\widetilde{Z''^2}$	−	Variance of the mixture fraction

Sub- and Superscripts

pin	-	Particle inception
sg	-	Surface growth
ox	-	Oxidation
ac	-	Agglomerate coagulation
$coag$	-	Coagulation
r	-	Order of statistical moment
c	-	Continuum regime
f	-	Free molecular regime
pp	-	Primary particle
S	-	Soot

Numbers

Da	-	Damköhler number
Ka	-	Karlovitz number
Kn	-	Knudsen number
Le	-	Lewis number
Pr	-	Prandtl number
Re	-	Reynolds number

Greek letters

δ_L	m	Laminar flame thickness
δ_T	m	Turbulent flame thickness
ϵ	J/s	Energy dissipation
λ	$W/(m\ K)$	Thermal conductivity
μ_τ	$kg/(m\ s)$	Dynamic viscosity
$\mu_{i,j}$	$-$	reduced mass
$\nu_\tau = \mu_\tau/\tilde{\rho}$	m^2/s	Turbulent viscosity
ν	m^2/s	Characteristic kinematic viscosity
$\dot{\omega}$	mol/s	reaction rate i terms of concentration
Ψ	$-$	Extensive variable
ρ	kg/m^3	Density
ρ_I	kg/m^3	Density
$\rho_\mathbf{S} = 1860 kg/m^3$	kg/m^3	Soot density
τ_τ	$-$	Reynolds stress tensor
ε	W/s	Velocity of the turbulent energy dissipation

Chapter 1

Introduction

The universe was born out of fire and explosion. Taming fire and making use of it has been very important for mankind. The earliest known evidence of fire used by hominids is from 700,000 BCE [2]. The first to study fire was the philosopher and scientist Empedocles (484 BCE) [3] who defined the species of all matter to be the four elements: fire, earth, air and water. He identified fire to be the rarest and most powerful of the elements, the soul of the world. Since then combustion has been of great interest to philosophers and scientists from many fields.

1.1 General Background

Combustion serves as an important energy source but is also the source of a large number of emissions such as soot. The effect of combustion on humankind and the environment is the subject of this section.

1.1.1 Combustion - A Source of Energy

The energy released in combustion processes has been the fundament of our society and technical development. As shown in figure 1.1 combustion accounted for 89% of the total global energy consumption in 1987. The energy gained from combustion serves us in our homes, for transportation, industrialization and in wars. Developing combustion devices as well as fuels has always occupied scientists and engineers. The world energy demand has increased from 3.5 $Gtoe$[1] in 1960 to about 10 $Gtoe$ at 2001 [4]. The Western world consumes

---

[1] $1\ PJ = 10^6\ GJ = 2.778\ GWh = 0.2388\ toe$, $[toe] \sim$ tons of oil equivalent

almost half of the commercial fuels (Table 1.1.1). The average citizen in the USA consumes more than 23 times the amount of commercial fuel of an African citizen. Our increasing dependence on energy, combustion and fuel can be seen in the latest wars.
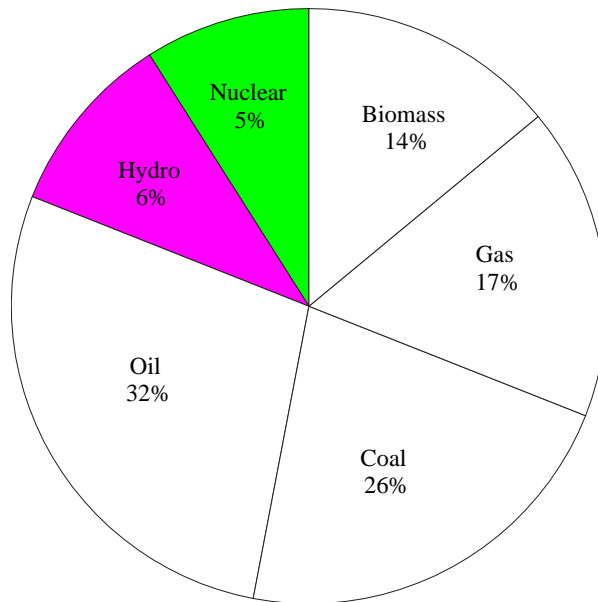
Figure 1.1: Distribution of the world energy consumption in 1987 [5].

1.1.2   Soot Particles and the Greenhouse Effect

Emissions have a considerable impact on health and the environment [6, 7]. They can be classified into two groups: gasified species and particulate matter (PM) of different sizes, such as soot. Soot particles constitute a large fraction of aerosols (airborn particles). Aerosols affect the earth's temperature and climate by altering the radiative properties of the atmosphere. Black elemental carbon is of special interest because it absorbs sunlight, heats the air, and contributes to global warming, unlike most aerosols, which reflect sunlight and have a global cooling effect [8]. The lifetime of soot in the atmosphere is limited, since it is affected by rainout or washout or is removed by sedimentation. In the troposphere, soot particle lifetimes are generally 1-3 weeks. Small soot particles may reach the stratosphere, where their lifetime is significantly extended, since rainout does not occur there. These lifetimes are still

Table 1.1: World Resources Consumption 1988.

Country, Continent	Per capita consumption of commercial fuels [PJ]	Consumption [GJ]	Share in total world consumption [%]
Africa	12	7109	2.6
USA	278	60760	22.0
South America	30	8109	3.0
Asia	20	58114	21.0
Europe	130	64177	23.0
UDSSR	187	52671	19.0
World	56	273201	100.0

less than that of CO_2 (50-95 years) since soot particles in the stratosphere are still subject to sedimentation, whereas CO_2 molecules are not. In a recent study, Jacobsen [7] predicted that eliminating all fossil fuel black carbon and organic matter could eliminate 20-45% of the earth's net warming within 3-5 years due to the short lifetime of soot in the atmosphere. It would take 50-200 years to reach the same result by CO_2 reduction, if emissions are reduced to one third. Jacobsen has shown [9] that the magnitude of the direct radiative forcing (direct forcing is the enhancement of the greenhouse effect due to the molecule) itself exceeds that due to CH_4, suggesting that black carbon may be the second most important component in global warming after CO_2 in terms of direct forcing. Jacobsen claims that the multiple-distribution direct forcing for soot of 0.55 Wm^{-2} falls between estimates for CH_4 of 0.47 Wm^{-2} and CO_2 of 1.56 Wm^{-2}. The Kyoto protocol of 1997 does not consider the emissions of soot at all [10].

1.1.3 Combustion Affects Environment and Health

It has been shown that lung function and bronchitis symptoms are associated with PM and PSA (particulate secondary aerosol). Furthermore it has been shown that exposure to traffic-related air pollution is related to fatal respiratory health diseases. Large particles are responsible for inflammatory disorders, while small particles can be even more harmful. Mortality may result from ultrafine particles with a diameter smaller than 4 μm, which are able to penetrate deep into the respiratory system. Ultrafine particles have the ability to pass

through the body barrier by translocation from the lungs into the interstitium and beyond [6]. New studies have linked PM exposure to cardiac diseases [11]. Several studies have shown associations between lung function and respiratory symptoms and ambient PM air pollution or traffic-related air pollution. Depending on its size and the weather conditions, particulate matter, including soot particles smaller than 3.2 μm, has the ability to travel in air from 2 up to 60 hours. High concentrations of PM are detected in urban areas. The PM content in air varies greatly with geography and season. Research shows that the particle source types associated with mortality are vehicle emissions, coal burning and vegetative burning [6]. The understanding of reactive flows is therefore highly relevant for the design of combustion devices and the definition of fuel.

1.1.4 Combustion Devices

The production of soot and other emissions indicates poor combustion efficiency, since a larger amount of the energy gained is used to produce and heat soot particles. Using knowledge of combustion mechanisms in order to reduce soot increases the effect. In combustion devices sot is deposited on the walls and injectors. These deposits harm the device and disturb the combustion process.

1.1.5 Fire

Combustion is not always a desirable phenomenon. The understanding of flame spread in fires is crucial to save lives. The field of flame spread is dominated by research on turbulent flow. The mortality rate in fires is dominated by intoxication [12]. Hence, the chemical perspective of combustion modelling is needed in combination with studies of turbulent flow. The toxic properties of soot do not play such a significant role in fires as the physical properties. Flame spread velocities and flame height from solid fuels have been studied among other parameters since the early 1970s [13]. The presence of soot in fires lowers the visibility and reduces the possibility of evacuation. The radiative heat of soot particles affects flame spread. Hence research on reactive flows is of great interest also in this field [14]. Besides life-threatening effects, there are considerable economic consequences of the emission of soot from fires on buildings and electronic equipment. Soot particles are small enough to enter any installation. They are then adsorbed onto surfaces shortening the lifetime of the object.

1.1.6 Soot Formation in outer Space

Carbon atoms, the main component of soot, are generated by nuclear fusion reactions in evolved stars, which later turn into red giants. Astronomers such as Feigelson and Frenklach [15] state that stellar winds transport the so-called interstellar dust, molecules containing carbon, from the giants into outer space. These interstellar clouds are very dense, have masses up to 10^6 times the solar mass and temperatures of about $1000\ K$. Spectral lines of PAH's (polyaromatic hyrdocarbons) and light scattered by particles thought to be soot are detected on earth. Simulations [15] using the PAH mechanism developed by Frenklach [16] for combustion processes, show that soot could be formed in interstellar clouds under the prevailing conditions.

Interstellar clouds cease to exist due to either the gravitational collapse of the cloud or due to the dispersion of the cloud resulting in the birth of young stars. This is the way our solar system was born about $4\frac{1}{2}$ billion years ago.

1.1.7 The Carbonblack Industry

Soot is not only an undesirable product. Soot is produced by the carbonblack industry and used for the reinforcement of materials in tyres and shoes [17].

1.2 Experimental Research

Another important role in combustion research is played by experimentalists. Experimental data are used to help out where models fail to give results within reasonable time. Semi-empirical models are of interest in several areas, such as fire spread and the definition of the soot point [18, 19]. Experimental results furthermore serve validation purposes. Various experimental techniques have been developed and applied in order to measure physical and chemical properties. Some techniques useful for measuring parameters and relevant for the formation of pollutants such as soot will be presented briefly in this section. Measurements of mixture fraction, scalar dissipation rate, species concentrations, density, temperature, soot volume fraction and soot size distribution, as well as the size and shape of agglomerates, are of great interest in this field. They are needed for the validation and the development of combustion models. Measuring soot volume fraction is a relevant but difficult task, since soot particles reduce the transmission of all wavelengths and non-spherical soot agglomerates scatter light diffusely.
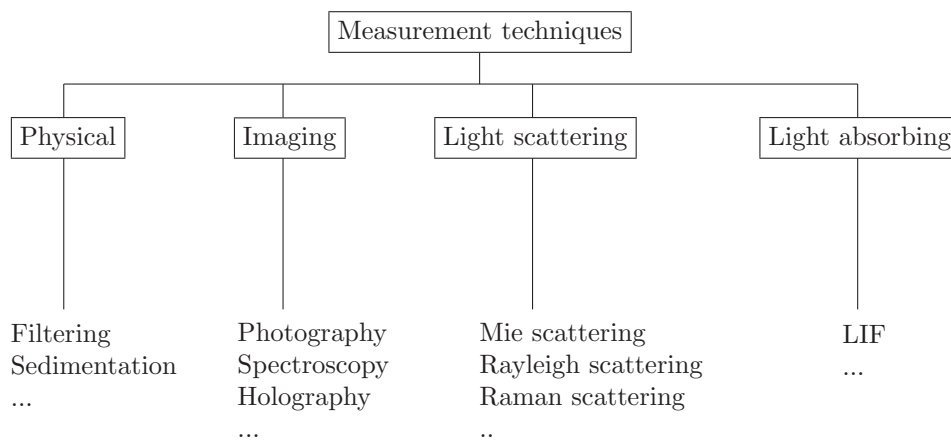
```
                          ┌─────────────────────────┐
                          │  Measurement techniques │
                          └─────────────────────────┘
```

```
┌──────────┐      ┌──────────┐      ┌─────────────────┐      ┌─────────────────┐
│ Physical │      │ Imaging  │      │ Light scattering│      │ Light absorbing │
└──────────┘      └──────────┘      └─────────────────┘      └─────────────────┘
```

Filtering   Photography   Mie scattering   LIF
Sedimentation   Spectroscopy   Rayleigh scattering   ...
...   Holography   Raman scattering
                      ...   ..

Figure 1.2: Particle size measurements, after [20].

1.2.1   Experimental Techniques and their Applications

Experimental techniques can be subdivided into five groups, see Figure 1.2. Some of the methods will be presented in this section.

Light scattering and absorbtion measurements

The light scattering and absorbing measurements discussed in this section are based on lasers as light sources (Mie, Rayleigh and Raman scattering) and scattering by electron beams (mass spectroscopy and electron microcopy). The measurements are based on recording the intensity or the change in wavelength of scattered or transmitted light. Some techniques e.g. Mie scattering and electron microscopy are applicable for larger objects such as particles. Techniques such as Rayleigh and Raman scattering, and mass spectroscopy are tools successfully applied to molecules extracted from the gas phase.

Mie scattering: This is a process in which light emitted from a light source is elastically scattered by particles. The scattered light has the same wavelength as the incident light. The light intensity is proportional to the fourth power of

the diameter of the scattering particles:

$$I \propto \left(\frac{d}{\lambda}\right)^4 \qquad (1.1)$$

There is a strong angular dependency of the scattered intensity. The method requires that the particle size is large compared with the wavelength. The technique can be used to analyse particle size, distribution and, to a certain degree, particle shape. The method is applicable for flow and spray analysis including particle size distribution and spray geometry. Mountain and Mulholland [21] applied Mie scattering to measure two parameters, which are required to determine the number of primary particles in an agglomerate, (see Equation 2.65):

1. the radius of gyration [22], $R_g = \sqrt{\frac{1}{n}\sum_i r_i^2}$, where r_i is the distance from the ith primary particle to the centre of mass of the aggregate,

2. the fractal dimension d_f of agglomerates.

Soot particles sizes and number densities were measured by Bonczyk et al. in 1991 using Mie scattering [23].

Rayleigh scattering: This is also a process in which radiation is emitted from a light source and scattered by molecules. As in Mie scattering, the scattered light has the same wavelength as the incident light, but targets are small compared with the wavelength. The light intensity is proportional to the intensity of incident light, a material-dependent constant and the number density of particles. The method is well suited for gases. The signal from Rayleigh scattering is much weaker than that from Mie scattering.

The method has applications in the detection of pollutant formation and in investigations of the total gas density and temperature fields, see Section 1.2.1.

Raman spectroscopy: In contrast to Rayleigh scattering, energy exchange takes place in this inelastic scattering process. Light from a UV laser is scattered by molecules, that have been excited into vibrational modes. The emitted wavelength differs from the incoming wavelength, and the molecule gains energy. Spectral analysis of the scattered light shows spectral lines positioned below the Rayleigh scattering peak at the incident frequency, the so-called Stokes lines. The spectral response of the molecules is shifted from the laser line. This shift is characteristic of Raman active molecules and allows measurements of species concentrations as well as temperatures and mixture fraction.

Laser-induced fluorescence: Laser-induced fluorescence (LIF) differs from Mie, Rayleigh and Raman scattering in that it is an absorption and wavelength conversion process, measuring spontaneous emission. A molecule is excited by electromagnetic radiation of a precise wavelength originating from a laser. This induces a molecular energy jump from the fundamental lower to a higher electronic energy level. The excited molecule spontaneously emits radiation of another wave-length in all directions. The energy of the emitted photons corresponds to the energy difference between the two levels. Hence, it generates a species-unique spectrum, which allows to detect and identify molecules. The intensity of the fluorescence indicates the species concentration. The LIF signal is weakened by internal and external processes such as the conversion between different vibrational and rotational electronic states of the molecule as well as through collision processes. The technique can be used to identify species and thereby pollutant formation. It is used for rotational or vibrational temperature measurements. Laser-induced fluorescence is a tool for species concentration measurements. Temporal resolution down to ns as well as spacial resolution down to 0.1-1.0 mm can be obtained [24]. The LIF technique has been used to perform PAH measurements [25]. Sutton et al. [26] and Su [27] extracted information about the scalar dissipation rate from planar laser induced fluorescence (PLIF) measurements of the mixture fraction.

Laser-induced incandescence: Laser-induced incandescence (LII) is a technique in which a laser beam is focussed onto particulate matter such as soot. The soot particles absorb energy and emit black-body radiation up to the point where vaporization occurs. Recording the emitted radiation gives information on the soot volume fraction, see for example Axelsson et al. [28] and Walewski et al. [29].

Mass spectrometry: This is a technique in which a sample of gas is extracted and bombarded with an electron beam fragmenting the molecule. The positively charged fragments are accelerated in a vacuum through a magnetic field and sorted on the basis of mass-to-charge ratio. Since the majority of the ions produced in the mass spectrometer carry a unit positive charge, the value is equivalent to the molecular weight of the fragment. Species can then be identified.

Transmission electron microscopy: In order to apply transmission electron microscopy (TEM), a sheet of matter must be extracted from the combustion chamber. This can be done via thermophoresis, by allowing matter, e.g. soot particles, to condense on a cold plate. The sample irradiated with a

monochromatic, focussed electron beam. Since the light beam is transmitted through certain parts of the sheet, a negative picture of the matter is produced and can be enlarged. The size of particles can be determined down to nanometres. Zhang et al. studied the morphology of soot agglomerates [30]. A series of studies on soot nucleation, surface growth and oxidation using TEM was performed by Faeth et al. [31, 32, 33, 34]. Furthermore, Faeth et al. performed studies on the shape, structure and size of agglomerates and primary particles [33, 35].

Other techniques

A number of relevant measurement techniques, which don't involve optical equipment are presented in this section.

Thermocouples: The method of thermocouples was first introduced by Nichols in 1900 [36], and is still in use today. A thermocouple consists of two metals, joined together at one end, which produce a certain voltage at a given temperature. This voltage is measured and interpreted by a thermocouple thermometer. Thermocouples consist of combinations of different metals. Depending on the material and diameter of the wires, thermocouples can indicate different temperature ranges.

Filters: Measurements of particle densities and sizes can be made with filters made of materials such as paper, tissue quartz [37] or silicon nitrid/parylene with pore sizes down 6 μm [38]. Another filtering technique are Micro-Orifice Uniform Deposit Impactors (MOUDI), cascade impactors. The filter makes use of the mass and diameter dependent centrifugal forces of the soot particles. The impactor consist of up to 10 impactor stages, walls, which are parallel aligned and perpendicular to the air-flow in a tube. The particles are transported in an air-flow through the tube. Since larger particles are more inert than smaller particles, they are more likely to attach to the walls. This way particles of a certain diameter are filtered and their mass ratio can be determined. The cut-off diameter in each stage depends on the air velocity and geometry of the walls. The MOUDI impactor can separate particles down to a size of 0.4 μm [39]. Filters, such as electrostatic filters [40], and traditional centrifugal filters [41], are used to remove soot particles reduce emissions.

Measuring relevant parameters

The determination of some of the relevant parameters often involves experiments based on the combination of the of several techniques mentioned above.

Some of the relevant parameters are presented here.

- Species concentrations have been measured successfully by combining LIF and Raman imaging [42].

- Mixture fractions in terms of the fuel mass fraction, $Y_{F,fuel}$, and the enthalpy assuming unity Lewis number and one-step chemistry were measured by Starner et al. [43]. $Y_{F,fuel}$ was determined using Raman and Rayleigh imaging.

- Investigations on soot formation in an acetylene/air premixed flame were performed by Choi et al. [44]. The experiments compared light extinction techniques such as LII with gravimetric techniques such as filters. The error in the light extinction technique was determined to be less than 6%.

- The size of uniform primary particles in agglomerates and the fractal dimensions of the agglomerates were the subject of experiments involving Rayleigh scattering performed by Dobbins and Megaridis [45].

- Measurements of temperature, gas species and soot volume fraction involving probe methods such as thermocouples and gas sampling techniques as well as Rayleigh scattering, were performed by McEnally et al. [46] 1998.

- An experimental group whose experimental set-up and choice of techniques is directed towards model development rather than the development of sophisticated measuring techniques is that of Moss at Cranfield University, UK . Their studies include temperature measurements with thermocouples, mixture fraction determination using mass spectroscopy and soot volume fraction with laser extinction measurements [47, 48, 49, 50]. These are very valuable for the validation of models and furthered the development of semi-empirical soot models.

1.2.2   Experiments used for Validation

The modelling described in this thesis was validated using experimental measurements of soot formation in turbulent and laminar diffusion flames. The work was performed using two different combinations of the above mentioned techniques.

Table 1.2: Mole fraction and flow rate for the laminar acetylene/nitrogen/air diffusion flame.

	Mole fraction	Flow rate
C_2H_2	16.85%	4.4
N_2	83.15%	21.7
Air	100.00%	94.7

1.2.3   Measuring the Characteristics of a Turbulent Ethylene/Air Diffusion Flame

The experiments were performed by Young et al. [49]. The set-up was a rim-stabilized C_2H_4 turbulent jet diffusion flame with a fuel nozzle diameter of 3.1 mm and a flow velocity of 24.5 m/s, and an initial temperature of 298 K at atmospheric pressure. The soot volume fraction was measured by laser absorption. Microprobe sampling was used to measure the mixture fraction. Temperature measurements were performed applying fine wire thermocouples.

1.2.4   Measuring the characteristics of a Laminar Acetylene/Nitrogen/Air Diffusion Flame

The experiments were performed by Xu and Faeth [33]. The experimental set-up was an air-co-flow-stabilized C_2H_2/N_2 laminar diffusion flame. The burner was 300 mm long. It had an inner port with a diameter of 34.8 mm and a co-annular port with a diameter of 60 mm. The purpose of the air co-flow was to prevent flame oscillations. The flame compositions and flow rates are given below. The measurements were done at an initial temperature of 294±2 K and a pressure of 98±1 kPa. The burner exit consisted of a honeycomb element that allowed lithium chloride particles to pass through, which were needed for the measurement of H concentrations. The honeycomb had 1 mm cell sizes with a length of 20 mm. The experiments were limited to measurements along the axes of buoyant laminar co-flowing jet-diffusion flames. The soot volume fraction was determined by deconvoluting laser extinction measurements at 632.8 nm. Species concentrations were determined by iso-kinetic sampling and analysis of gas chromatography.

1.3   Numerical Modelling

Combustion models for premixed combustion and non-premixed combustion differ. In premixed combustion a blend of oxidizer and fuel is ignited, whereas in non-premixed combustion the fuel and oxidizer are mixed during the combustion process. A stoichiometric mixture is reached in a domain between the two flows. This thin zone has a high chemical reactivity which leads to heat release and an increase in temperature. Combustion is possible in this domain, defined as the reaction zone. There is a fast decrease in temperature outside the reaction zone, caused by the diffusive mixture of the hot and the cold gas. This retards the reaction and puts an end to the combustion process. This work focuses on non-premixed combustion. In this section laminar combustion is considered to be a grade of turbulence.

There are two primary constituents in a numerical turbulent combustion model:

- models describing the physics of flow,

- and models describing the interaction between the chemical reaction zone and physical flow.

Numerical models are based on a set of equations describing the conservation of the extensive variable $\psi(t)$. Depending on the system ψ may denote energy, momentum or an other characteristic variable. In general, $\Psi(t)$ can be defined as follows:

$$\Psi(t) = \int_{\Omega} \psi(\mathbf{x}, t) dV \tag{1.2}$$

where $\mathbf{x}$ is the spatial coordinate vector. The density of $\Psi(t)$ is defined as:

$$\psi(\mathbf{x}, t) = \frac{d\Psi(t)}{dV} \tag{1.3}$$

The general definition of the conservation equation is given by:

$$\frac{\partial}{\partial t}(\rho\psi) = -\frac{\partial}{\partial x_j}(u_i\rho\psi) + \frac{\partial}{\partial x_j}(\mathbf{D_{ij}}\frac{\partial \psi}{\partial x_i}) + S_{\Psi} \tag{1.4}$$

in words the tidal variation of Ψ is: - the convective transport of Ψ + the diffusion of Ψ + the source term of Ψ,
where $\mathbf{D}_{ij}$ is the diffusion, S_{Ψ} is the source term. The specific conservation equations for relevant extensive variables are defined in Equation 1.5, 1.6 and 1.7.

$$\frac{\partial \rho u_j}{\partial t} = -\frac{\partial \rho u_i u_j}{\partial x_j} - \frac{\partial p}{\partial x_i} + \frac{\partial \tau_{ij}}{\partial x_j} \tag{1.5}$$

The continuity equation is:

$$\frac{\partial \rho}{\partial t} = -\frac{\partial \rho u_j}{\partial x_j} \tag{1.6}$$

The energy equation, in terms of enthalpy h is:

$$\rho \frac{\partial h}{\partial t} = -\rho v_i \frac{\partial h}{\partial x_i} + \frac{\partial}{\partial x_i}\left(\rho D_Z \frac{\partial h}{\partial x_i}\right) + \frac{\partial p}{\partial t} + S_r \tag{1.7}$$

The species conservation equation, for species I is:

$$\rho \frac{\partial Y_I}{\partial t} = -\rho u_i \frac{\partial Y_I}{\partial x_i} - \frac{\partial}{\partial x_i}\left(\rho Y_I V_{iI}\right) + \dot{\omega}_I \tag{1.8}$$

1.3.1 Turbulent Scales

In order to describe turbulent systems several length and time scales, as well as three dimensionless numbers, the Reynolds number, the Karlowitz number and the Damköhler number, are introduced. The Reynolds number is a measure of turbulence. A system in which the Reynolds number is greater than 1500 is a turbulent system. It is defined as the ratio of inertial forces to viscous forces [51], or as:

$$Re = \frac{Velocity \ \cdot \ Length \ scale}{Kinematic \ viscosity} \tag{1.9}$$

Length scales

Length scales relevant for physical and chemical interactions are:

L	the macroscale
l_I	the integral scale or the Taylor macroscale
l_λ	the Taylor microscale
l_K	the Kolmogorov microscale
l_c	the scale for chemical reactions
δ_L	the laminar flame thickness
δ_T	the turbulent flame thickness

The macroscale, L, is the largest possible diameter of an eddy, e.g. the diameter of the pipe wherein the flow is contained. Being the size of the space wherein the flow is contained, it is no longer a measure of turbulence but of laminar flow. The Reynolds number based on the mean flow velocity can be defined using this length scale. It is not, however, a measure of turbulence. The largest

turbulence length scale is the Taylor macroscale or integral length scale l_I. This scale is a measure of the largest wrinkles and the largest turbulent eddies in the system are:

$$l_I = \int_0^\infty R_x(x)dx \tag{1.10}$$

where:

$$R_x(x) = \frac{\overline{u_i'(0)u_i'(x)}}{u_{i,rms}'(0)u_{i,rms}'(x)} \tag{1.11}$$

The definition of Taylor's microscale l_λ was his attempt to find the smallest turbulent scale [52]. Instead he defined the mean size of the eddies in a flow. It has the same magnitude as l_I. Taylor's microscale (Equation 1.12) represents the maximum distance between two points at which there is still a correlation between the fluctuating velocities [53].

$$l_\lambda = \frac{\nu l_0}{v'} = \frac{l_0^2}{R_l} \tag{1.12}$$

It is related to the energy dissipation per unit volume in an isotropic turbulent system as:

$$\epsilon \propto \nu \frac{\overline{u_x^2}}{l_\lambda^2} \tag{1.13}$$

The Kolmogorov microscale scale, l_K, is the smallest turbulent length scale. It represents the scale at which the dissipation of the turbulent kinetic energy to internal fluid energy occurs. Molecular interactions are relevant on this scale. This is a domain of unity Reynolds number (see Section 1.3.1). The Kolmogorov length scale is related to the energy dissipation by:

$$l_K \approx \left(\frac{\nu^3}{\epsilon}\right)^{\frac{1}{4}} \tag{1.14}$$

where ν is the molecular kinematic viscosity. The energy dissipation is related to the turbulent kinetic energy per unit mass, ke_{turb} as follows [52]:

$$\epsilon \equiv \frac{\partial(ke_{turb})}{\partial t} \approx \frac{3v_{rms}'^3}{2l_I} \tag{1.15}$$

The smallest length scale l_c is the scale at which chemical reactions can occur without being disturbed by turbulence. It is smaller than the smallest eddy and is thus unaffected by the turbulence of the flow.

The flame thickness: The flame thickness is not a classical length scale. However, it is a measure of the size of the reaction zone. The laminar and turbulent flame thickness are differentiated as described below. The laminar flame thickness, δ_L, is related to the chemical reactions and the flame velocity S_L [54]:

$$\delta_L \approx \frac{a}{S_L} \tag{1.16}$$

where $a = \frac{\lambda}{\rho c_p}$ is the thermal diffusion coefficient, λ is the thermal conductivity, ρ the density and c_p the heat capacity. The turbulent flame thickness, δ_T, is mainly controlled by the turbulent diffusion. Using the maximum gradient method the flame thickness an be estimated to be a function of density:

$$\delta_T = \frac{\rho_u - \rho_b}{\left(\frac{d\overline{\rho}}{dx}\right)_{max}} \tag{1.17}$$

where ρ_u is the density of the unburned mixture and ρ_b is the density of the burned mixture.

Time scales

Chemical and physical events occur on different time scales and in different time intervals (see Figure 1.3). There is an interval where physical events such as flow affect the chemical reactions. Relevant turbulent time scales are defined in relation to the largest and the smallest length scales. The integral time scale is approximated by:

$$t_I \approx \frac{l_I}{u'} \tag{1.18}$$

where the integral velocity u' is a function of velocity fluctuations u_i'':

$$u' = \sqrt{\frac{1}{2}\widetilde{u_i''^2}}$$

The Kolmogorov time scale is defined as a function of the molecular kinematic viscosity and the dissipation rate.

$$t_K = \sqrt{\frac{\nu}{\epsilon}} \tag{1.19}$$

The Kolmgorov length scale and velocity are related to the kinematic viscosity:
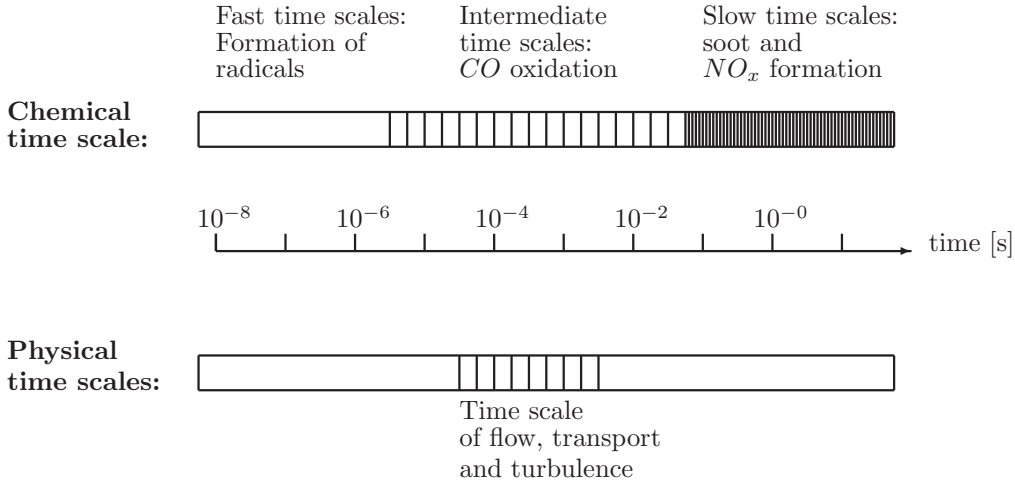
$$l_K = \sqrt[1/4]{\frac{\nu^3}{\epsilon}} \tag{1.20}$$

Fast time scales: Intermediate   Slow time scales:
Formation of   time scales: soot and
radicals CO oxidation NO_x formation

**Chemical
time scale:**

10^{-8} 10^{-6} 10^{-4} 10^{-2} 10^{-0}

time [s]

**Physical
time scales:**

Time scale
of flow, transport
and turbulence

Figure 1.3: Chemical and physical time scales (after Maas and Pope [55]).

and:

$$u_K = \frac{l_K}{t_K} = \sqrt[1/4]{\nu\epsilon} \tag{1.21}$$

The chemical time scale is related to the flame thickness and is approximated by [52]:

$$t_c \approx \frac{\delta_L}{S_L} \tag{1.22}$$

where t_c depends on the scalar dissipation rate, χ, as follows [56]:

$$t_c = \frac{Z_{st}^2(1 - Z_{st})^2}{\chi_{st}} \tag{1.23}$$

Velocities: The definitions of lengths and times lead to the a number of corresponding velocity estimates. The laminar flame speed is defined as [53]:

$$S_L \approx \sqrt{\frac{\lambda\dot{\omega}}{\rho^2 c_p}} \tag{1.24}$$

The turbulent flame velocity [54] can be expressed as the laminar flame velocity with an additional fluctuation term by:

$$S_T = S_L + u'$$

(1.25)

where the turbulence fluctuation velocity reads [54]:

$$u' = 4\sqrt{\frac{2k_I}{\rho_I}}$$

(1.26)

here, k_I is the turbulence kinetic energy and ρ_I the density.

Dimensionless numbers

Three dimensionless numbers indicate different domains of combustion: the Reynolds number, the Karlowitz number and the Damköhler number. Three different turbulent Reynolds numbers can be defined by the turbulent length scales. The Reynolds number of the integral scale:

$$Re_{l_I} \equiv u'_{rms}\frac{l_I}{\nu}$$

(1.27)

The Reynolds number of the Taylor microscale:

$$Re_{l_\lambda} \equiv u'_{rms}\frac{l_\lambda}{\nu}$$

(1.28)

The Reynolds number of the Kolmogorov scale:

$$Re_{l_K} \equiv u'_{rms}\frac{l_K}{\nu}$$

(1.29)

The three turbulent length scales are related through the Reynolds number of the macroscale.

$$\sqrt{Re_{l_I}} = \frac{l_I}{l_\lambda}$$

(1.30)

$$\sqrt[3/4]{Re_{l_I}} = \frac{l_I}{l_K}$$

(1.31)

Another measure of turbulence is the dimensionless Karlowitz number, K_a. It provides an expression for the relation between the largest time scale, the integral time scale, and the smallest, the Kolmogorov time scale:

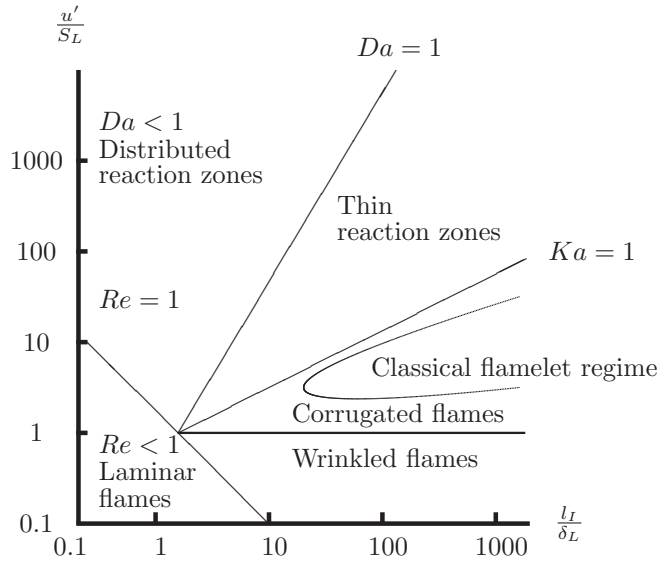$$K_a = \frac{t_I}{t_K}$$

(1.32)

Figure 1.4: Borghi diagram: Different zones of combustion in a space as a function of turbulent *vs.* laminar velocity length scale (after [53]).

The smallest eddies penetrate the laminar flamelet preheated zones at Karlowitz numbers close to unity. In this region the flame thickness and the flame velocity are those of the smallest scales: $\delta_L \cong l_K$ and $S \cong u_K$.

The Damköhler number indicates whether chemistry is fast, $(D_a \gg 1)$, or slow, $(D_a \ll 1)$, relative to the turbulence time scales. The Damköhler number expresses the relation between the integral timescale and the timescale wherein the chemical reactions occur as:

$$D_a = \frac{t_{flow}}{t_{chem}} \tag{1.33}$$

The Damköhler number can be given in terms of the velocity ratio $\frac{S_L}{u'_{rms}}$ and the length scale ratio $\frac{l_0}{\delta_L}$.

$$D_a = \frac{t_0}{t_L} = \left(\frac{l_0}{\delta_L}\right)\left(\frac{S_L}{u'_{rms}}\right) \tag{1.34}$$

These turbulent dimensionless numbers help in defining limits for different domains in combustion. The Borghi diagram illustrates the different regimes for premixed combustion distributed in space (Figure 1.4). The space coordinates

are defined the turbulent vs. laminar velocity- and the turbulent vs. laminar length axis.

In the domain where $Re < 1$, the flame front is laminar and undisturbed. For large Reynolds numbers four different zones can be identified by their turbulence intensities $\frac{u'}{S_L}$, Ka and Da [51]. Before analysing the different regimes it should be mentioned that the following classification only presents a quantitative estimate, which is based on some additional simplifications such as neglecting transient effects. Studies show that the classification defined here can not strictly be limited to the domains. Nevertheless they provide some understanding of the validity of the existing models.

Laminar flame regime: $Re \rightarrow 0$

The laminar flame represents combustion in a non-turbulent flow field. Chemical reactions takes place undisturbed by turbulent interactions. The differential diffusion of species affects the chemistry in this domain. Figure 1.5 shows an example of a laminar diffusion flame, a candle.
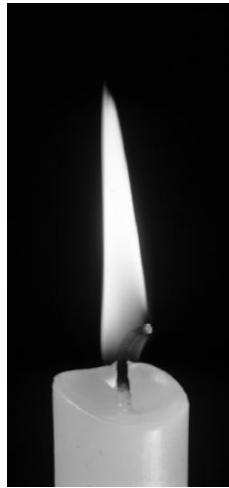

Figure 1.5: Laminar diffusion flame [57].

Wrinkled laminar flame regime: $Da > 1$, $Ka < 1$ and $\delta_L \leq l_K$.

In this domain the chemical reactions occur in thin sheets. Depending on the turbulent Reynolds number, Re_{l_I}, the fast chemistry assumption is valid. This implies that the chemical reactions are faster than the influence of the turbulent flow field. For moderate Reynolds and Damköhler numbers the turbulent

velocity is of the order of the laminar flame speed, $u' \approx S_L$. The only effect of the turbulence is the wrinkling of the flame. Figure 1.6 shows an example for a wrinkled flame. The limit $Ka = 1$ is used to define the Klimov-Williams criterion, separating two combustion domains. Peters has shown for domains where $Ka > 1$ that the inner structure of the flames, but not necessarily the reaction zone, are affected by turbulence [58].

Figure 1.6: Turbulent flame [57].

Flamelet regime: $Ka < 1$ and $Da > 1$

The flame is divided into an ensemble of small laminar flames in the flow field. The conservation equations are solved for the ensemble. For turbulent Reynolds number numbers converging to 0 the flame turns into a laminar flame and the approach is exact. For higher Reynolds numbers, the concept is valid for fast chemistry. This approach was studied in the present work and ways were sought to expand it to a larger domain. Methods will be introduced to model slow chemistry and other transient effects with this method. The approach will be analysed in more detail below.
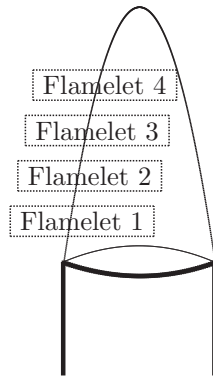
Figure 1.7: Diagram of a diffusion flame consisting of a family of flamelets.

Distributed reaction regime: $l_I/\delta_L < 1$ and $Da < 1$
The turbulence length scales in this domain are within the reaction zones. The process can be described by a well stirred reactor. It is questionable whether flames have a chance to survive in this region.

Flamelet in eddies regime: $Da \approx 1$, $I_T \gg 1$ and $l_I > \delta_L > l_K$
The flow in this domain can be divided into two zones. A large-scale zone and a zone containing the reaction zone, which is smaller than a Kolmogorov eddy. Combustion occurs within a quasi laminar flow inside an eddy. Fluctuations may be neglected in this domain. The scalar dissipation rate, χ, defined in Section 3.2.5 and its statistical distribution must be considered. The fluctuations for the larger scales are removed by applying a filter to the original conservation equations [56]. This leads to conservation equations in the flamelet space wherein fluctuating variables, among those the reaction rate, are neglected. Hence, the conserved variable, the mixture fraction, Z, and the density ρ, can be averaged within large scales. This domain occurs in practical combustion devices. The flamelet model, which is the subject of this work is valid for large Damköhler numbers and small Karlowitz numbers. The flame changes its shape depending on its thickness:

1.3.2   Numerical Modelling of Turbulent Flows

Turbulent flows can be characterized by the presence of random vortices, the so-called eddies. Eddies vary temporally in size and direction. Large eddies contain small eddies. They obtain turbulence energy from the flow field, the largest scale comparable to the characteristic system dimensions. The kinetic energy is redistributed in the so-called turbulence energy cascade through non-linear instabilities. It is dispersed through a hierarchy of smaller and smaller flow structures. Ultimately, it is dissipated at the smallest scale, the Kolmogorov dissipation scale. The energy associated with the eddy of scale $l = \frac{2\pi}{k}$ is:

$$kE(k) \tag{1.35}$$

The velocity is given by:

$$u(k) = \sqrt{kE(k)} \tag{1.36}$$

And the strain is defined by:

$$s(k) = \sqrt{kE(k)}\frac{1}{l} = \sqrt{k^3 E(k)}\frac{1}{2\pi} \tag{1.37}$$

where:

$$E(k) \approx k^{-5/3} \tag{1.38}$$

so that:

$$s(k) \approx k^{2/3} \tag{1.39}$$

An increase in strain at the smallest scales results in heat production. Different approaches can be found in the literature to describe turbulent flows. The models can be coupled to detailed chemical calculations, as described in Section 1.3.3.

Reynolds averaged Navier-Stokes concept

The Reynolds averaged Navier-Stokes (RANS) concept is based on time averaging the conservation equations and modelling the remaining, the so-called Reynolds stress terms. By doing this the turbulent field is separated into a mean and a fluctuation component [51]. This can be done by resolving the extensive variable Ψ into it's mean $\overline{\Psi}$ and a fluctuating part Ψ' by Reynolds decomposition as:

$$\Psi(x_i, t) = \overline{\Psi}(x_i, t) + \Psi'(x_i, t) \tag{1.40}$$

For flows with non-constant density the Favre average, a mass-weighted average, $\tilde{\Psi}$, is introduced as:

$$\tilde{\Psi} = \frac{\overline{\rho\Psi}}{\overline{\Psi}} \tag{1.41}$$

$$\Psi(x_i, t) = \tilde{\Psi}(x_i, t) + \Psi''(x_i, t) \tag{1.42}$$

where Ψ'' is the fluctuating part. This method removes turbulent fluctuations by constructing the average value. The fluctuations are then accounted for through the Reynolds stress tensor.

$$-\overline{\rho u_i'' \Psi_j''} \tag{1.43}$$

A general formulation of the averaged Navier-Stokes equation for the extensive variable Ψ is given below.

$$\frac{\partial}{\partial t}\overline{\rho}\tilde{\Psi} = -\frac{\partial}{\partial x_i}(\overline{\rho}\tilde{u}_i\tilde{\Psi}) + \frac{\partial}{\partial x_i}(\overline{\rho})(\mathbf{D_{ij}}\frac{\partial \tilde{\Psi}}{\partial x_i} - \overline{\rho u_i''\Psi_j''}) + \overline{S} \tag{1.44}$$

Closure problem: The RANS method has the advantage that it is based on the main flow symmetry and it therefore only requires the steady-state solution of the mean flow field. This implies that the method is not able to consider time-dependent phenomena, which are frequent in turbulent fields. Another problem is that new correlations appear due to the process of averaging [52]. An example is the averaged non-linear momentum flux.

$$\overline{\rho u \circ u} = \overline{\rho}\tilde{u} \circ \tilde{u} + \overline{\rho u'' \circ u''} \tag{1.45}$$

The correlation between the velocity fluctuations in the turbulent stress tensor is:

$$\tau_\tau = \overline{\rho u'' \circ u''} \tag{1.46}$$

cannot generally be expressed analytically as a function of the mean field variables such as $\tilde{u}$. The goal is to derive a closed system of equations for the mean quantities. This has not yet been achieved. To obtain a system with a sufficient number of equations for all unknowns, closure approximations are introduced. They replace the unknown correlations with explicit functions of the mean quantities. A number of heuristic closure approximations have been developed in recent years. These models rely on a gradient diffusion approximation for the turbulent transport terms. The Reynolds average Navier-Stokes concept was originally developed to describe the the physics of flow. However, more general approaches including equations for mass and energy have been introduced. The flamelet model is an applicable approach to supply the model with information on combustion chemistry.

Algebraic turbulence models: Algebraic turbulence models are also-called 0-equation models since they do not introduce additional conservation equations in order to solve the closure problem. Algebraic turbulence models divide the system into compact packets of turbulent fluids, which traverse a characteristic length, l_{mix}, relative to the mean flow [59]. The packets carry fluctuations of extensive variables such as the energy and momentum to other fluid regions. Energy and momentum are strongly dependent on the mixing length and the amplitude of the fluctuations in the small field. The system is closed relative to the mixing length, a term which has to be modelled. Different heuristic models exist to determine the mixing length and they cannot be considered as turbulent flow closures. Most algebraic models are designed for special systems and are not applicable for more general multi-dimensional flow situations. Algebraic models are also linear eddy viscosity models, which follow:

$$\epsilon = \mu_t \rho \tag{1.47}$$

$$\frac{\mu_t}{\rho} \propto \langle velocity \rangle \langle length \rangle \tag{1.48}$$

One-equation models.   One-equation models are based on the Reynolds- or Favre- averaged equations. They are closed by one additional partial differential equation. Those models assume that the turbulent kinetic energy critically influences the net turbulent transport. The definition of a characteristic length, l_τ, or time scale, t_τ, of turbulence leads to the determination of the turbulent viscosity, ν_τ, Equation 1.50, as a function of the kinetic energy k:

$$\nu_\tau = \frac{\mu_\tau}{\overline{\rho}} \tag{1.49}$$

$$\nu_\tau \sim l_\tau \sqrt{k} \tag{1.50}$$

$$\tilde{k} = \frac{1}{2} \frac{\overline{\rho \sum u_i^{2"}}}{\overline{\rho}} \tag{1.51}$$

One-equation models give the possibility to derive an equation for the turbulent kinetic energy, as done by Wilcox [60].

$$\overline{\rho}\frac{\partial k}{\partial t} + \overline{\rho}\tilde{u} \cdot \nabla k \quad = \quad \overline{\rho}\tau_\tau : \nabla\tilde{u} - \overline{\rho\tau : \nabla u"} \tag{1.52}$$

$$+ \nabla \cdot \left(\overline{\rho\tau \cdot \nabla u"} - \overline{\rho u" \frac{u^2}{2}} - \overline{p'u"} \right)$$

$$- \overline{u"} \cdot \nabla \overline{p} + \overline{p'\nabla \cdot u"}$$

Part of the closure model can be based on exact information. A number of terms in the system must again be modelled. One- and two-equation models differ in the way in which they obtain the second missing dimensional characteristic length scale l_τ or t_τ. One-equation models assess the mixing length through an algebraic formula (similar to algebraic models). This formula must generally explicitly incorporate some specific reference to the flow configuration considered [59]. One-equation models are not closed in a general way. They cannot be solved by supplying initial and boundary conditions. The model equations must be changed from one set of input to another through adjustment of the mixing length and the associated variations in the turbulent transport coefficients.

Two-equation models; the k–ϵ model: Two-equation models introduce an additional transport equation for the mixing quantity [59]. Existing approaches vary from modelling the characteristic turbulent mixing length, l, to the product kl or the inverse, ω, of a characteristic turbulent time scale. [61, 62, 63]. These lead to k–l, k–kl or k–ω models. The most popular approach is the k–ϵ model. The k–ϵ model describes the specific turbulence kinetic energy k, and its dissipation rate, ϵ, by one PDF (see Section 1.3.4) as.

$$k = \frac{1}{2}\widetilde{u_i''^2} = \frac{2}{3}u'^2 \tag{1.53}$$

$$\epsilon = \nu\widetilde{\frac{\partial u_i''^2}{\partial x_k}} \tag{1.54}$$

Here k and ϵ are modelled with one PDF each in addition to the averaged versions of the continuity and momentum equations

$$\frac{\partial \overline{\rho} k}{\partial t} + \widetilde{u}_j \frac{\partial \overline{\rho} k}{\partial x_j} = -\overline{\rho \widetilde{u_i'' u_j''}} \frac{\partial \widetilde{u}_i}{\partial x_j} - \overline{\rho}\epsilon \tag{1.55}$$
$$+ \frac{\partial}{\partial x_j}\left(\left(\mu + \frac{\mu_T}{Pr_k}\right)\frac{\partial k}{\partial x_j}\right) - \frac{\mu_T}{\overline{\rho}^2}\frac{\partial \overline{\rho}}{\partial x_i}\frac{\partial \overline{p}}{\partial x_i}$$

$$\frac{\partial \overline{\rho}\epsilon}{\partial t} + \widetilde{u}_j \frac{\partial \overline{\rho}\epsilon}{\partial x_j} = -C_{\epsilon 1}\frac{\epsilon}{k}\left(\overline{\rho\widetilde{u_i'' u_j''}}\frac{\partial \widetilde{u}_i}{\partial x_j} + \frac{\mu_T}{\overline{\rho}^2}\frac{\partial \overline{\rho}}{\partial x_i}\frac{\partial \overline{p}}{\partial x_i}\right) \tag{1.56}$$
$$- C_{\epsilon 2}\overline{\rho}\frac{\epsilon^2}{k} + \frac{\partial}{\partial x_j}\left(\left(\mu + \frac{\mu_T}{Pr_k}\right)\frac{\partial \epsilon}{\partial x_j}\right)$$

The turbulent Prandtl numbers, $Pr_k = 1.0$ and $Pr_\epsilon = 1.3$, as well as $C_{\epsilon 1} = 1.44$ and $C_{\epsilon 2} = 1.92$ are model constants [64]. The eddy viscosity equation is given

by:

$$\mu_T = \overline{\rho} C_\mu \frac{k^2}{\epsilon} \qquad (1.57)$$

The constant C_μ is set at 0.09. This equation satisfies a governing equation containing unclosed terms that are difficult to measure or define. The method is generally valid for homogeneous, isotropic systems with no abrupt changes in the strain. This method can be extended to non-constant density and weakly compressible flows, if equations describing mass and energy balances are introduced. A number of new effects arise that lead to new unclosed terms [59] such as:

- turbulent heat fluxes,

- dilatation-induced dissipation of kinetic energy, for $\nabla \cdot v \neq 0$, and

- pressure changes due to velocity fluctuations.

Since there are more unknowns than equations the system cannot be closed. Different methods have been suggested in order to solve this problem. The most common is the Reynolds stress model, which will be described below.

The Reynold stress model: Reynolds stress models (RSM) solve transport equations for the unclosed terms. Conservation equations for quantities $\overline{\rho u_i'' u_j''}$ in all directions are added to the mass, momentum and energy balances. This approach is much more general than those mentioned in previous sections. It offers a wide range of applicability without fine tuning. The stress transport equations are derived from the original equations. In addition, the transport equation for the Reynolds stresses follows the Wilcox [60] formulation:

$$\frac{\partial \tau_\tau}{\partial t} + \overline{\mathbf{u}} \cdot \nabla \tau_\tau = -\tau_\tau \cdot \overline{\mathbf{u}} - (\tau_\tau \cdot \nabla \overline{\mathbf{u}})^t + \epsilon - \Pi + \nabla \cdot (\nu \nabla \tau_\tau + C) \qquad (1.58)$$

where:

$$\Pi = \overline{\frac{p'}{\rho}(\nabla u' + (\nabla u')^t)} \qquad (1.59)$$

with:

$$\epsilon = \overline{2\nu(\nabla u')^t \cdot \nabla u'} \qquad (1.60)$$

and

$$\rho \nabla \cdot C = \overline{\rho u' \circ u'(\nabla \cdot u')} + \nabla(\overline{p'u'})(\nabla(\overline{p'u'}))^t \qquad (1.61)$$

The Reynolds stress transport model accounts for effects that are lost in the simplified algebraic, one- and two-equation models. The model provides the desired enhanced capabilities and more general applicability. These include [59]:

- effects of flow history,

- convection, production and body force effects, and

- unequal normal stresses, allowing proper adjustment under sudden non-isotropic changes in strain rates.

Closure is required for the determination of parameters Π, C and ϵ. The most popular Reynolds stress model introduces explicit closure for the pressure strain and triple correlations covered by Π and C, but retain an additional dynamic equation for the dissipation tensor ϵ_{ij}. In order to obtain the full dissipation tensor, ϵ_{ij}, it is necessary to model the time evolution of its trace, ϵ, from Equation 1.57. This is done by including either a dissipation evolution equation, as in a k–ϵ model, or by modelling the evolution of a characteristic turbulence time scale, $y_t \sim 1/\omega$, through an ω equation. This method has a much higher accuracy than the algebraic, one- and two-equation models but requires much more computational effort.

Large eddy simulations

Large eddy simulations (LES) model the physics of flow by solving the conservation equations in a discretized field. This implies that the large scales are resolved, while small scales, scales smaller than the size of the mesh, are removed by applying a spacial grid filter before the equations are discretized. Defining the mesh size is equivalent to defining the smallest scale wherein homogeneity and isotropy are assumed. The accuracy of the model can be increased by decreasing the mesh size, which implies a significant increase in CPU time. The contribution of small-scale turbulent fluctuations and other unsteady turbulence phenomena is accounted for by introducing the sub-grid scale model (SGS) into the balance equations. The SGS represents the interaction between resolved, large scales and unresolved, small scales. The concept of filtering is a characteristic of all LES models. Given a filter definition one can proceed to derive new governing equations for the filtered quantities (the new LES variables) by applying the filter to the original conservation equations. The filter defines the boundary between the larger and the smaller structures of the system. The turbulent energy cascade is assumed to be valid and model fluctuations are ignored, while energy dissipation is considered. The model can be coupled to detailed chemical calculations, as described in Section 1.3.3. The LES has its disadvantages, however, since it requires considerable computational effort, especially for the description of large-scale systems. Another problem is that the concept of the energy cascade, the fundamental assumption of the method, is not valid for all systems, such as multiple fluid phases.

Direct numerical simulation

Direct numerical simulation (DNS) [65] is the most detailed approach for describing combustion systems. All scales are resolved in both time and space down to the smallest scale, the Kolmogorov scale. DNS has been applied to studies on flame-flow interactions. For a flow characterized by the Kolmogorov scale, l_K, the number of uniformly spaced nodes N_{nodes} is of the order of $\left(\frac{l_L}{l_k}^3\right) \approx Re_{l_I}^{9/4}$. DNS is very expensive in CPU time and is thereby limited to low Reynolds numbers, small grid size and thicker flame zones. The CPU time needed for the simplest models exceeds the order of Re^3 (see Table 1.3.2). Because of its limitations due to high computational cost, DNS is not very practical. Other methods make use of assumptions in order to speed up the computation process.

Table 1.3: Estimates for nodes and time step requirements for DNS simulation of a channel flow [57].

Re_{l_λ}	N_{nodes}	$N_{\Delta t}$
12 300	$6.7 \cdot 10^6$	32 000
30 800	$4.0 \cdot 10^7$	47 000
61 600	$1.5 \cdot 10^8$	63 000
230 000	$2.1 \cdot 10^9$	114 000

1.3.3 Interface for flow and chemical models

The previously introduced flow models do not consider non-linear phenomena such as the chemical reactions occurring in all combustion process. The flamelet model is a suitable way to introduce chemical models into the physics of the flow. The chemistry considered in this work is based on the unsteady and the steady flamelet models (Section 3.2 and 3.3). The approaches couple differently to the flow calculations. A detailed description of their implementation can be found in Sections 3.2.6 and 3.3.2. A general coupling strategy is schematically described in Figure 1.8. Parameters relevant for the interface, such as the scalar dissipation rate, mixture fraction and enthalpy, are determined by the flow code and introduced into the flamelet calculations where chemical terms are calculated.

- The unsteady flamelet model (Section 3.2) solves time-dependent conservation equations, among these, the species conservation equation. The species are formed through detailed chemical reactions. The approach
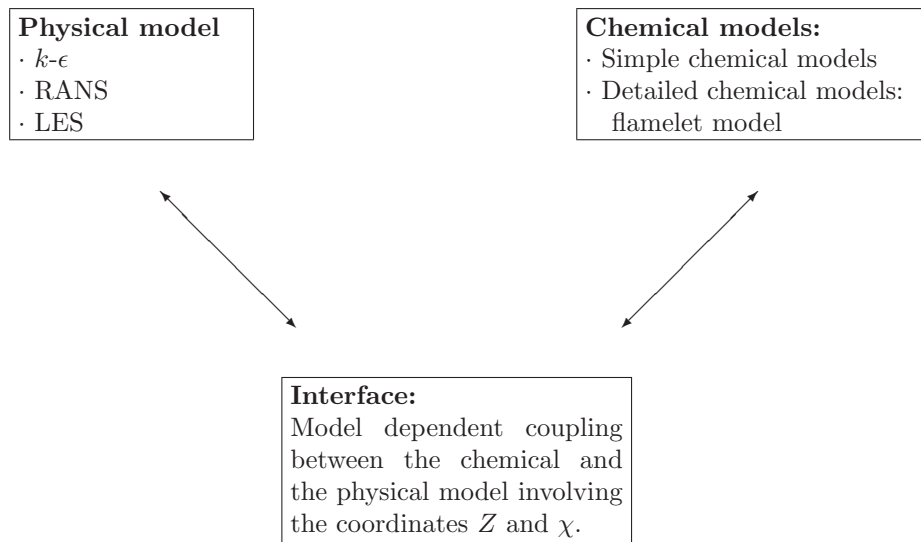
Physical model
· k-ϵ
· RANS
· LES

Chemical models:
· Simple chemical models
· Detailed chemical models:
  flamelet model

Interface:
Model dependent coupling
between the chemical and
the physical model involving
the coordinates Z and χ.

Figure 1.8: Coupling detailed chemical models to flow models.

considers transient effects such as the process of soot formation and radiation effects. Transport and diffusion effects are included to the model via the time-dependent scalar dissipation rate at stoichiometry, calculated by the flow code. The conditional scalar dissipation rate, $\chi_{st}(t)$, is a parameter describing the evolution of the flamelet.

- The steady flamelet model, Section 3.3, is a special case of the general formulation, the unsteady flamelet model, omitting the time derivative. The model is based on the fast chemistry assumption. Emissions such as soot and NO_x are formed slowly and therefore the steady flamelet approach is used to calculate source terms for these species and store them in libraries. The concentrations and volume fractions are then determined by the flow code, where transport equations for these species are solved. The model ca be implemented as shown in Figure 1.9.

  1. The mass fraction, $Y_i(Z, \chi, \alpha)$, for species i is precalculated in flamelet space, Z, χ, using the flamelet method. The α denotes the radiation factor, which is of special interest for soot formation. $Y_i(Z, \chi)$ can be stored in libraries.

2. The precalculated species mass fractions are averaged with a β-PDF for the mixture fraction, Z, (Equation 1.74) and the log-normal distribution or delta function of χ.

3. The chemistry is introduced into the flow model.

A more schematic example of the coupling to large eddy simulation is presented in Figure 1.9. [66, 67]. Filtered reaction rates, $\bar{\bar{\omega}}_i$, for species i for the LES code are calculated from flamelet libraries as functions of the precalculated species mass fractions and the β-PDF for the mixture fraction, Z, as well as the log-normal distribution or delta function of χ.

- The coupling to the steady flamelet library approach can be further simplified by compressing the libraries using e.g. polynomial fits. Subroutines containing the polynomials can then be introduced into the CFD-code and easily provide the chemical information.

1.3.4   Numerical Modelling of Reactive Flows

The chemical source term of species i, $\dot{\omega}_i$ is needed in order to solve the conservation equations, describing combustion processes. The basis of this investigation is the simple irreversible reaction between species A and B which forms the single product P.

$$A + B \rightarrow P \qquad (1.62)$$

The instantaneous chemical source term is given by:

$$k_P = AT^{\beta} \exp(-E_P/RT) \qquad (1.63)$$

where k_P is given by the Arrhenius expression:

$$\dot{\omega_A} = \dot{\omega_B} = -k_P Y_A Y_B \qquad (1.64)$$

The mass fraction, Y_i, of species i is a function of the partial molar mass of species i, m_i, and the total molar mass, $m = \sum_{i=1}^{n} m_i$:

$$Y_i \equiv \frac{m_i}{m} \qquad (1.65)$$

The mass fraction can be expressed as a function of the molar mass X_i, the average mass, M, and the molar mass of species i, M_i.

$$Y_i = \frac{M}{M} X_i \qquad (1.66)$$

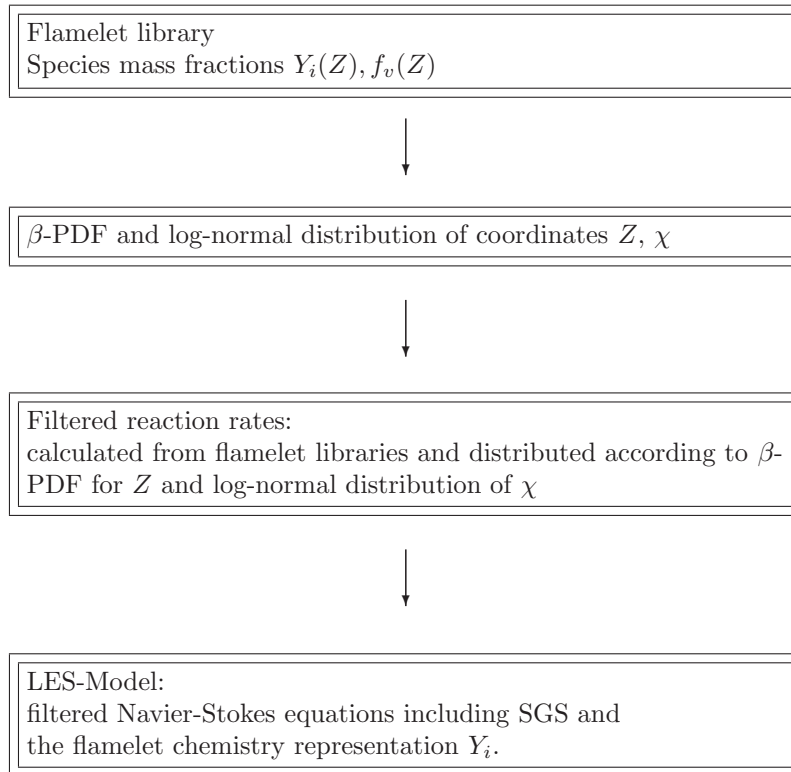Different models exist to close the chemical source terms $\dot{\omega}_i$.

```
┌──────────────────────────────────────────────────────────┐
│ Flamelet library                                          │
│ Species mass fractions Y_i(Z), f_v(Z)                     │
└──────────────────────────────────────────────────────────┘
                            │
                            ▼
┌──────────────────────────────────────────────────────────┐
│ β-PDF and log-normal distribution of coordinates Z, χ     │
└──────────────────────────────────────────────────────────┘
                            │
                            ▼
┌──────────────────────────────────────────────────────────┐
│ Filtered reaction rates:                                  │
│ calculated from flamelet libraries and distributed        │
│ according to β-PDF for Z and log-normal distribution of χ │
└──────────────────────────────────────────────────────────┘
                            │
                            ▼
┌──────────────────────────────────────────────────────────┐
│ LES-Model:                                                │
│ filtered Navier-Stokes equations including SGS and        │
│ the flamelet chemistry representation Y_i.                │
└──────────────────────────────────────────────────────────┘
```

Figure 1.9: Coupling of the flamelet method to large eddy simulations.

Conserved scalar: Bilger was the first to define species concentration as a function of a coupling variable, the so-called mixture fraction [68]. Assuming that the system can be restricted to a stream of pure fuel and a stream of pure oxidizer, the mixture fraction, Z, can be defined:

$$Z = \frac{Mass\ of\ material\ having\ its\ origin\ in\ the\ fuel\ stream}{Mass\ of\ mixture} \qquad (1.67)$$

Since Equation 1.67 applies to an infinitesimally small value, Z is simply a special kind of mass fraction, formed in relation to fuel mass, oxidizer mass and product mass.

$Z = 0$ in the oxidizer stream

$Z = 1$ in the fuel stream

The mixture fraction can be expressed in terms of the mass fractions of species j:

$$Z_j = \sum_{i=1}^{n} \frac{a_{ij} M_j}{M_i} Y_i \qquad (1.68)$$

A more detailed derivation of Equation 1.68 can be found in Section 3.1.2. The mixture fraction is a conserved scalar, since it has the characteristic property that it is conserved throughout the flow field. The conserved scalar concept greatly simplifies the chemical question, posed by the reacting flow. After the mixture fraction was defined, conservation equations for species as a function of the mixture fraction were developed.

Eddy dissipation models

Eddy dissipation models are empirical and applicable for fast chemistry as well as for moderate reaction rates. They are defined in a domain with $Re \gg 1$ and $Da \gg 1$. The reaction rate is controlled by turbulence dissipation rates. The reaction zone is considered to be a mixture of unburned and burned zones. The reaction rate was derived by Spalding [69]:

$$\overline{\omega_i} = -\frac{\overline{\rho} C_F}{\overline{M}} \sqrt{\omega_i^{''2}} \frac{\tilde{\epsilon}}{\tilde{k}} \qquad (1.69)$$

where $C_F \sim 1$ is an empirical variable. The model does not treat chemical characteristics in detail. It is applied in combination with many commercial flow codes.

Probability density function method

The Probability density function approach (PDF) focuses on the statistical properties of turbulent combustion systems. Such method assumes that the

variables describing the chemical systems are statistically independent and not correlated [70]:

$$P(\rho, T, .., Y_1, ..., Y_n) = P(\rho) \cdot P(T) \cdot ... \cdot P(Y_1) \cdot ... \cdot P(Y_n) \tag{1.70}$$

with the norm:

$$\int P(x)dx = 1 \tag{1.71}$$

The approach enables the modelling of the temporal evolution of reactive and thermodynamical scalars as well as flow velocities. Hence, integrating the appropriate moments of the PDF, $P(\mathbf{Y}, p, \rho, T, v; \mathbf{x}, t)$ gives information on the statistical means and correlations. The functions are based on empirical data and often modelled as clipped *Gauss* function (Equation 1.72):

$$P(x) = \alpha \cdot \delta(x) + \beta \cdot \delta(1-x) + \gamma \cdot \exp\left[-\frac{(x-\zeta)^2}{2\sigma^2}\right] \tag{1.72}$$

where:

$$\gamma = \frac{(1-\alpha-\beta)\sqrt{\frac{2\sigma}{\pi}}}{erf\left(\frac{1-\zeta}{\sqrt{2\sigma}}\right) + erf\left(\frac{\zeta}{\sqrt{2\sigma}}\right)} \tag{1.73}$$

or a β function (Equation 1.74):

$$P(x) = \gamma x^{\alpha-1} x^{\beta-1} \tag{1.74}$$

where:

$$\gamma = \frac{\Gamma(\alpha+\beta)}{\Gamma(\alpha) \cdot (\beta)} \tag{1.75}$$

where the constants α and β are determined by the average and variance of x:

$$\overline{x} = \frac{\alpha}{\alpha+\beta} \tag{1.76}$$

and:

$$\overline{x'^2} = \frac{\overline{x}(1-\overline{x})}{1+\alpha+\beta} \tag{1.77}$$

Conditional moment closure

The conditional moment closure (CMC) method [68] expresses species production by conditional averages and the approximate conditional moment. $\langle Y_i(\mathbf{x}, t) | Z(\mathbf{x}, t) = \eta \rangle$. The evolution of species concentrations is considered along a conditional, e.g. stoichiometric iso-Z surface. The transport equations,

the instantaneous mass fraction, Y_i, and the mixture fraction terms (defined in Section 3.1.2) can thus be solved as:

$$\rho\frac{\partial Y_i}{\partial t} + \rho u \cdot \nabla Y_i - \nabla \cdot \rho D_i \nabla Y_i = \dot{\omega}_i \qquad (1.78)$$

$$\frac{\partial Z}{\partial t} + \rho u \cdot \nabla Z - \nabla \cdot \rho D_Z \nabla Z = 0 \qquad (1.79)$$

The instantaneous mass fraction, Y_i, is decomposed into the conditional mean, Q, and the fluctuation, y, around the conditional mean. This can be within a certain mixture fraction range. The result is a function, Q, which is dependent on the mixture fraction, Z, and the position in the flow field x. The fluctuations around the conditional mean, Q, are much smaller than the temporal fluctuation, Y. Angular brackets denote conditional averaging of Y under the condition to the right of the vertical bar, $Z(\mathbf{x}, t) = \eta$.

$$Y_i(\mathbf{x}, t) = Q_i(\eta, \mathbf{x}, t) + y(\mathbf{x}, t) \qquad (1.80)$$

where:

$$Q_i(\eta, \mathbf{x}, t) \equiv \langle Y_i(\mathbf{x}, t)|Z(\mathbf{x}, t) = \eta\rangle \qquad (1.81)$$

and $y \ll Y'$. Assuming $Re \gg 1$, the CMC transport equations for species i are derived via conditional averaging:

$$\langle\rho|\eta\rangle\frac{\partial Q_i}{\partial t} = \langle\rho\mathbf{u}|\eta\rangle \cdot Q - \frac{1}{2}\frac{D_i}{D_\xi}\langle\rho\mathbf{x}|\eta\rangle\frac{\partial^2 Q_i}{\partial\eta^2} \qquad (1.82)$$

$$+ \nabla \cdot [\rho(D_i - D_\xi)\nabla\xi]\frac{\partial Q_i}{\partial\eta} + \epsilon_{y,i}$$

where the fluctuation term ϵ_y is given by:

$$\epsilon_{y,i} \equiv -\langle[\rho\frac{\partial y}{\partial t} + \rho\mathbf{u} \cdot \nabla y - \rho D_i \nabla^2 y]|\eta\rangle\chi = 2D_\xi\nabla\xi \cdot \nabla\xi \qquad (1.83)$$

All terms on the right-hand-side of Equation 1.82 are unclosed and require modelling. Literature provides suggestions how the terms may be closed.

1. Scalar dissipation χ is generally modelled with Girimajis closure assuming local homogeneity [71].

2. The reaction term of reaction k is modelled using simple first-order closure.

$$\langle\omega_k|\eta\rangle = \rho_\eta k(Q_T)Q_iQ_j$$

3. The fluctuation term, ϵ_y, is neglected.

The first closure, conditional mean reaction rates are estimated from:

$$\langle \omega_i(\mathbf{Y}, T)|\eta\rangle = \omega(\mathbf{Q}, Q_T) \tag{1.84}$$

This approach is valid if the conditional fluctuations of the reactive scalars are small enough for high-order terms to be negligible.

Second order conditional moment closure: Second-order closure [72] employs the conditional variances and covariances to improve the estimate of $\langle \omega_i|\eta\rangle$. This has been described in the literature with the Taylor expansion method and the assumed PDF method. The latter is more CPU-demanding but more accurate. In the assumed PDF method, the conditional mean reaction rate terms are calculated by:

$$\langle \omega_i(\mathbf{Y}, T)|\eta\rangle = \int_{\Omega_\eta} \omega_i(\zeta_1, ..., \zeta_n; \eta) P(\zeta_1, ..., \zeta_n)|\eta) d\zeta_1 ... d\zeta_n \tag{1.85}$$

where n is the number of reactions, ζ_i is the sample variable for the reaction progress variable, $C_i, i = 1, ..., n$ and ω_η is the sample space of the reaction progress variables $C_i, i = 1, ..., n$, at η. P is the conditional joint PDF.

Doubly-conditional moment closure modelling: In order to model extinction and re-ignition effects in turbulent, non-premixed combustion the doubly-conditional moment closure model was developed [73]. The method is based on Kilmenkoo and Bilger's multi-conditional moment closure [74]. The scalar dissipation rate is introduced as a second conditioning variable into the first-moment, singly-conditional moment closure model. The source term for χ states that:

$$\frac{L(\chi)}{\rho} \equiv \left(\frac{\partial}{\partial t} + \mathbf{u} \cdot \nabla - D\nabla^2 \right) \chi \tag{1.86}$$

with constant diffusion D and density ρ. The method is better suited to describe two-flow systems and extinction and re-ignition processes, than the single CMC.

Other CMC methods: There are several other models within CMC such as the conditional source-term estimation (CSE) model [75] which does not add any dimensionality to the equations. Similarly to LES it can be applied to either spatially filtered equations or Reynolds averaged contexts.

Flamelet modelling

The flamelet approach is the subject of this thesis. The idea that a turbulent, non-premixed flame can be seen as an ensemble of counterflow diffusion flames, so-called laminar flamelets, was first introduced by Williams [76]. Peters [77] extended this theory by comparing the chemical and physical time scales in turbulent flames taking non-equilibrium effects into account. The most important aspect of the laminar flamelet method is the decoupling of the chemistry modelling from the calculations of the flow field.

Such approach is based on the assumption that the chemical reaction time is much shorter than the time scale of the turbulent flow. This implies that the chemical reactions take place so fast that they remain unaffected by the movement in the turbulent flow. The region where the classical flamelet assumption is valid is identified in the Borghi diagram (Figure 1.4), where $D_a > 1$. In this domain the time scale for chemical reactions is smaller than that of the turbulent system. Peters divided the domain into five different states of the flamelet [77]:

1. the steady unreacted initial mixture,

2. the unsteady transition after ignition,

3. the quasi-steady burning state,

4. the unsteady transition after quenching, and

5. the unsteady transition after re-ignition with the stationary states.

States 1 and 3 are time-independent states. The species concentrations and temperature can be calculated using the steady flamelet approach. States 2, 4 and 5 are time-dependent. The must be modelled interactively with a CFD code,which is CPU-demanding. However, relevant pollutants such as NO_x and soot are generated very slowly and the concentrations calculated from the quasi-steady burning state are never reached. Two flamelet approaches were shown to be able to handle this problem.

The unsteady flamelet method was first applied by Pitsch [78] in order to model transient effects such as the slow formation of NO_x as well as other transient effects such as the loss of enthalpy due to radiation. Time dependent flamelet equations are solved with information from the CFD code. As mentioned before the steady flamelet method (Section 3.3) is a special variant of the unsteady flamelet model (Section 3.2). It can be used to precalculate a library containing source terms of quantities not reaching the quasi-steady burning state, such as enthalpy, NO_x and soot. The transport equations are

then solved with the CFD code. The application of this concept to soot formation has been shown to provide an efficient approximation of the transient process of soot formation. Since the sources are given as functions of the local mixing and strain conditions, mean enthalpy and pressure, the model becomes independent of the flame-flow interaction the model employed in the CFD code. The flamelet model itself can be considered to be a special case of the conditional moment closure method, conditioned at a mixture fraction interval and the scalar dissipation rate at stoichiometry, χ_{st}.

1.4 The Soot Model

Soot is an agglomerate of particles, which vary in structure and size [79]. The main constituent of soot is carbon and some minor amounts of hydrogen and oxygen. Depending on the surrounding gas, other species may adsorb onto the surface of soot. Although many properties of soot have been identified, it has not been possible to uniquely define the chemical composition of soot.

The size of the smallest soot particle follows the limits of experimental research. The size of the smallest primary particle is detected with an electron microscope and has a size of $20nm$ [80]. Figure 1.10 shows an electron microscopic image of soot particles from the combustion of pyrolysis gas from wood chips produced of Technical University of Denmark [81]. Soot is produced during the combustion of hydrocarbons under fuel-rich conditions at high temperatures. The emission of soot from a flame is determined by the formation and oxidation of soot. Soot models of today describe the formation of soot in seven steps (Figure 1.11).

1. Reactions in the gas phase: The first step in soot formation is the formation of cyclic benzene c-C_6H_6 and phenyl c-C_6H_5 in the gas phase. The cyclic molecules grow further into two-dimensional Polyaromatic hydrocarbons (PAH).

2. Inception of particles: This is the first step wherein two two-dimensional PAHs merge into one three-dimensional particle.

3. Condensation: The particles grow via condensation of a two-dimensional PAH on a three-dimensional PAH.

4. Surface growth: The particles grow via reactions with the gas phase. Acetylene (C_2H_2) is mainly responsible for the growth of soot particles.
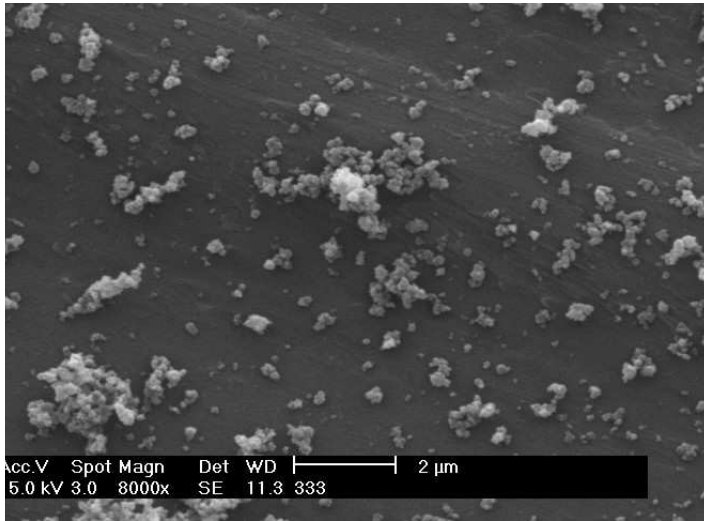
5. Coagulation: Two soot particles merge.

Figure 1.10: Soot particles formed by the pyrolysis of wood chips (electron microscope image) [81].

6. Agglomeration: Large clusters of particles are formed.

7. Oxidation: The soot particle looses mass in reactions with gas phase molecules O_2 and OH.

Source terms of soot formation can be assigned to each steps of soot formation and reduction. Figure 1.12 is taken from Megaridis and Dobbins [82]. It shows that the zone upstream in the flame is dominated by inception and condensation of PAHs previously formed in the gas phase. These are the first soot particles. The the particles grow in the reaction with C_2H_2. They coagulate and form large agglomerates. At high temperatures the soot particles interact with the gas phase and oxidation reduces the size of the particles. This Figure is very schematic and does not tell the complete truth. Soot formation occurs even in the horizontal plane of the flame, which does not show in the figure. The single processes of soot formation are dependent of the mixture fraction scalar dissipation rate and enthalpy. They are present at all times, even though the zones are dominated by different processes.

A large number of models have been developed to describe the formation of soot in various combustion situations. These include a number of chemical models, ranging from simple chemical mechanisms, with a few reactions, to large detailed chemical models. They also vary in their description of soot

formation built in the flow code as a postprocess or interactively with the flow code. Kennedy [83] classified existing models into three groups, a classification which will be followed in this section.

1. Empirical models based completely on experimental data.

2. Semi-empirical computer models containing a mathematical description supplemented with data originating from experimental result.

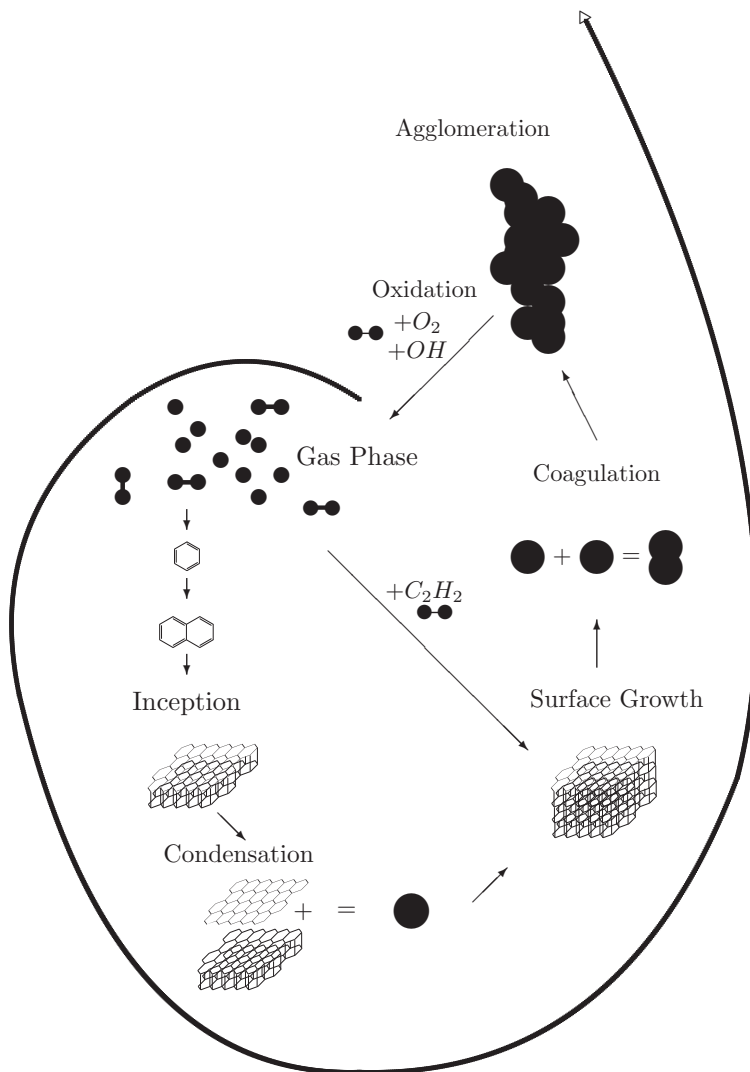3. Detailed models seeking to solve the rate equations for the elementary reactions that lead to soot.

Figure 1.11: Process of soot formation.
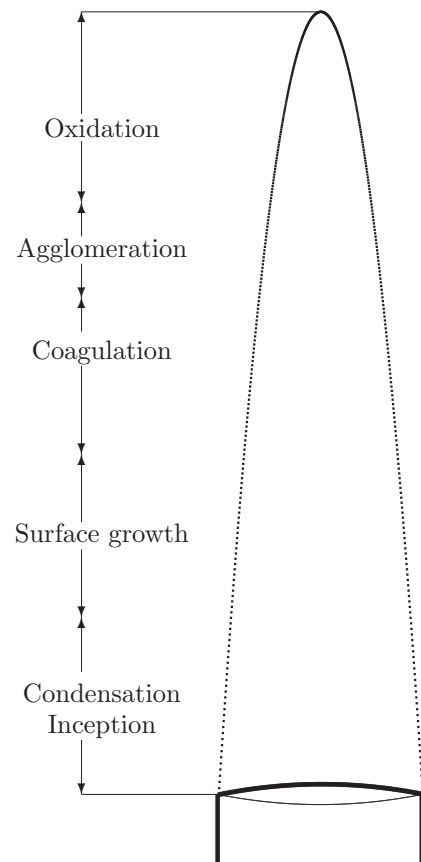
Figure 1.12: A schematic description of the dominant sources of soot formation in different zones in a flame. The radial components are neglected (after Megaridis and Dobbins [82]).

1.4.1 Empirical Models

The pioneers of the field developed empirical models. Some scientists still work with empirical models since they give rapid results. They are based on experimental results and are designed to model a certain combustion situation and do not describe combustion processes in general. Empirical models do not require complex modelling and are thus easy to develop and require little CPU time. Most empirical models are based on the definition threshold sooting index (TSI). The first to define the TSI as a function of the equivalence ratio were Calcote and Manos [84]:

$$TSI = a + b\Phi_C \tag{1.87}$$

where a and b are empirical constants and Φ_C is the critical threshold equivalence ratio. Soot formation is expected to begin when the C/O ratio exceeds unity. Experiments have shown that this event already occurs at $C/O = 0.5$ [1]. The definition of the TSI was further developed by Gill and Olson [85] who included a contribution of each component of the fuel to the TSI. The model was extended by Glassman and Takahashi [86] who expressed the TSI as a function of an effective equivalence ratio, $\Phi \equiv \frac{2C+H}{2O}$. The models were further developed and applied to different combustion conditions. In 1991 Kahn et al. [87] proposed a model describing soot formation in diesel engines. They assumed that the diameter of soot particles formed in engines was constant for all speeds and loads. As a consequence, soot formation became the result of particle inception alone. Particle inception was considered to be a function of pressure, the equivalence ratio of unburned gases and the temperature. Lefebvre [88] applied the Kahn model to gas turbines. De Ris et al. [18] developed a model describing soot formation in fires in buildings. Their method is based on the measurement of the soot layer thickness, δ_S, through the deposition of soot particles on metal rods placed at different locations in the flame. Megaridis and Dobbins [82] found the soot volume fraction to be proportional to the deposition. Curve fits of the measurements resulted in the following definition of the soot volume fraction:

$$f_V \delta_S = -\lambda_0 \frac{\ln(1 - \epsilon_0)}{7} \tag{1.88}$$

where ϵ_0 is the extinction coefficient taken from Markstein [18] and $\lambda_0 \in [0.9, 1.0]$ μm is the wavelength. The main interest in the present work was to include the radiative properties of the soot in a simple model.

One may wonder why is it of interest to spend more time on understanding the details of soot formation and oxidation, if such simple models exist? One answer might be the following: In order to be able to counteract the process

of soot formation in combustion, and thereby optimize combustion as well as avoiding emission and pollution due to soot, it is not sufficient to know only where soot is formed in the flame, but also how and why it is generated. Another answer is that it is very exciting to find answers to all the questions that arise in this field. Modellers still struggle to achieve the most detailed description of pollution formation in flames, using as little CPU time as possible. The third answer is that the applicability of simple models is restricted to the exact conditions of a particular combustion process. More detailed models succeed in describing combustion process in a general way.

1.4.2   Semi-empirical Models

Many semi-empirical models focus on reproducing experimental results regarding the formation of soot and its precursors. They are often based on simple chemical models and parameters which are to fit the experimental results. In 1971 Tesner et al. [89], developed a model of soot formation based on simple kinetics and a two-step mechanism for soot production: the formation and reduction of soot nuclei. The aim of the model was to interpret measurements performed by Tesner [90] in an acetylene/hydrogen flame. The rate of particle formation is given by:

$$\frac{dn}{dt} = n_0 + (f - g)n - g_0 N n \qquad (1.89)$$

where n_0 is the initial number of nuclei, f and g are branching and terminating coefficients, g_0, is the rate of loss of nuclei due to collisions with gas molecules and N is the number density of soot particles given by:

$$\frac{dN}{dt} = (a - bN)n \qquad (1.90)$$

Here, a and b are adjustable parameters. Tesner's soot model can be considered to be the foundation of many later soot models. Some of them will be presented here. Soot formation in laminar and turbulent, premixed, co- and counter flow flames is the focus of a great number of numerical and experimental studies. Surovikin [91] developed a more detailed model to describe the formation of soot particles and added oxidation to the model.

Surovikin formulated a model in four steps:

1. formation of radical nucleus,

2. growth of nucleus to incipient particle,

3. growth of incipient particle into carbon particles, and

4. oxidation of the soot particle via O_2.

Magnussen et al. [92] extended Tesner's two-step soot concept with the oxidation of soot and coupled it to a simple eddy dissipation model to calculate a turbulent acetylene flame. Here the reactants were assumed to be homogeneously mixed. Brown and Heywood [93] improved the mixing properties by adding a stochastic mixing model to simulate the inhomogeneous mixing and combustion in a diesel engine. Other flow codes such as the KIVA code have been coupled to Tesner's two-step soot kinetics. Jensen et al. [94] defined a soot model in five steps. The soot nucleus was answered to consist of C_2 or C_2H molecules. The steps to soot formation applied in this model are:

1. Reversible gas phase mechanism containing 11 reactions, wherein soot nuclei are formed,

2. Coagulation,

3. Soot surface growth,

4. Oxidation,

Graham [95] assumed that the first steps of soot formation took place by the pyrolysis of aromatic hydrocarbons. Dobbins et al. [82] suggested that soot particles were formed in a graphitization process of liquid droplets. Mulholland [96] formulated a simple reaction mechanism for the soot formation process in Arrhenius form, where large nuclei were formed during pyrolysis of the fuel. The surface growth was assumed to be proportional to the area of the soot surface. The fuel itself was considered to be responsible for the surface growth. Kennedy et al. [83] formulated an equation to describe soot formation in which the number density was assumed to be constant. Moss' soot model [48] is of special interest since it is based on the flamelet concept to model soot formation in diffusion flames, which is also the focus of this thesis. The model accounts for: particle inception causing an increase in number density; surface growth; coagulation as well as oxidation through O_2 and OH. The source terms for the number density and the soot volume fraction are expressed as functions of

temperature and mixture fraction. The model consists of two soot equations for the number density, N, and the soot volume fraction f_V.

$$\frac{d}{dt}\left(\frac{n}{N_0}\right) = \alpha(Z) - \beta(Z)\left(\frac{n}{N_0}\right)^2 \tag{1.91}$$

$$\rho_S \frac{df_V}{dt} = \gamma(Z)n + \delta(Z) \tag{1.92}$$

The source terms α, β, γ and δ for the number density are given by:

$$\alpha = C_\alpha \rho^2 \sqrt{T} X_{fuel} \exp\left(-\frac{T_\alpha}{T}\right) = \frac{\delta}{144} \tag{1.93}$$

$$\beta = C_\beta \sqrt{T} \tag{1.94}$$

$$\gamma = C_\gamma \sqrt{T} X_C \exp\left(-\frac{T_\alpha}{T}\right) \tag{1.95}$$

where n_0 is the initial number of nuclei, T is the temperature and T_i is the activation temperature. X_{fuel} is the mole fraction of the fuel. C_α, C_β and C_δ are parameters used to calibrate the model to experimental results obtained by Young et al. [97] in ethylene/air flames. Syed et al. [98] coupled the model to a parabolic k–ϵ turbulence model. Another approach relevant the present work was done by Lindstedt [19, 99]. Lindstedt developed soot models for laminar and turbulent diffusion flames. He also applied the flamelet approach to compute species concentrations and a simple soot model to predict soot volume fractions in diffusion flames. The flamelet model was coupled to a CFD code. He made the crucial contribution to model evolution by making C_2H_2 mainly responsible for the nucleation process. The effect of acetylene on soot formation is now a well-studied phenomenon [100].

$$C_2H_2 \rightarrow 2C_{soot} + H \tag{1.96}$$

His model contained the usual steps: nucleation, surface growth, coagulation and oxidation and and a few chemical reactions for the gas phase. The result was adjusted to experimental data by parameter variations. A number of modellers are occupied with studying the reduction of soot, since this is a very relevant phenomenon. Among these are Harries et al. [101], who formulated a simple OH, O_2 oxidation mechanism containing the enduct CO_2 and implementing the Nagel–Strickland–Constable [102] formula of O_2-oxidation. Mechanisms for different fuels and species have been defined, such as a methane mechanism by Smooke et al. [103] and a mechanism involving C_2 chemistry by

Frenklach [104]. The chemical mechanism, which were developed grew larger with an increasing number of reactants. Numerical methods were developed in order to solve non-linear differential equations balancing the chemistry. Another contribution to this field, of relevance in this thesis is that of Kollmann et al. [105]. A PDF transport model was used to simulate the reacting turbulent flow in a sooting ethylene diffusion flame. Kollmann et al. calculated the process of soot formation using a simple soot model based on experimental chemical source terms [105]. In this approach the source terms are functions of the mixture fraction.

1.4.3   Detailed Chemical Models

In order to provide predictions that are generally valid for any combustion condition, modellers have began to work on models that are free from experimental input parameters. Experiments serve for validation in this context. This aim is to define mechanisms for the complete process, and thus increase our understanding of the formation of soot and soot precursors such as C_2H_2 and PAHs. One of the biggest contributions in this field comes from Frenklach and co-workers. The soot model applied in this thesis is based on the work by Frenklach et al. and others, and will be discussed in Chapter 2.

Chapter 2

The Chemical Soot Model

The different steps of soot formation introduced in the previous chapter is the foundation of this work. They are modelled using chemical and statistical methods which will be presented in this chapter.

2.1 Chemical and Statistical Methods

Different concepts were used in this work to model the formation of soot particles. The generation of soot can be described by chemical mechanisms. Almost one hundred species and about a thousand reactions are involved in the chemical reactions taking place in the gas phase. Even more reactions would be needed to model the generation of soot particles completely. In order to limit the computational demands, some of these reactions have been replaced by a statistical approach. Hence, the characteristics of the formation of soot particles are conveniently described by particle size distribution functions (PSDFs). The smallest unit of the particle size distribution function for soot is the carbon atom, the basic constituent of soot. All physical and chemical processes affecting the PSD must be included in the description. The statistical method of moments introduced by Frenklach et al. [106] and described in Section 2.1.2, makes it possible to solve soot particle size distribution functions.

2.1.1 Chemical Methods

The first steps in soot formation are chemical reactions of species present in the gas. The work presented in this thesis was based on a detailed chemical

model, which is the subject of this chapter. Global reactions of the type:

$$Enduct(A) + x_1 Enduct(B) \rightarrow x_2 Product$$
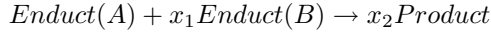
are broken down into elemental reactions of the type

$$A + B \rightarrow C + D \tag{2.1}$$

where A, B, C and D are species in the gas. The reaction rate at which A is produced in Equation 2.1 is a function of the concentrations of species A, $[A]$ and B, $[B]$ and the reaction coefficient k:

$$\frac{d[A]}{dt} = -k[A][B] \tag{2.2}$$

where the reaction coefficient in low-temperature domains can be defined through the Arrhenius form.

$$k(T) = A \exp -\frac{E_A}{RT} \tag{2.3}$$

At higher temperatures, an equation in non-Arrhenius form 2.4 is used:

$$k(T) = AT^b \exp -\frac{E_A}{RT} \tag{2.4}$$

where T is the temperature in Kelvin, E the energy and R the universal gas constant. The species balance equation is solved for every species involved in the combustion process.

$$\rho \frac{\partial Y_i}{\partial t} = -\rho u_\alpha \frac{\partial Y_i}{\partial x_\alpha} + \frac{\partial}{\partial x_\alpha} \left(\rho D \frac{\partial Y_i}{\partial x_\alpha} \right) + \dot{\omega}_i \tag{2.5}$$

2.1.2   Statistical Method - Method of Moments

The statistical methods which will be introduced in this section replace a great number chemical reactions for soot formation. The formation of soot particles can be broken down to an infinite number of collision processes of particles of all sizes. The particle size distribution function (PSDF) is one approach to describe the number density, N_i, of particles of all size classes, equations for the number densities of all size classes $i = 1, .., \infty$ with the mass $m_i = i \cdot m_1$, based on the mass of the smallest unit is the mass of the carbon atom m_c.

$$N_i = f(d_i, t, T, ...) \tag{2.6}$$

where N_i is a function of diameter d_i, time t, temperature K and others. The process of growth is divided into discrete classes. The moments of the PSDF can be solved using the statistical method of moments [107] and [106] where:

$$M_r = \sum_{i=1}^{\infty} m_i^r N_i \quad r = 0, 1, 2, ... \tag{2.7}$$

The method of moments is applied to describe the distribution of the size classes. The method is based on the fact that the direct simulation of the particle size distribution can be replaced by an infinite set of equations describing the statistical method of moments. In this work only a few moments are used in order to safe CPU time, and the validity of this is discussed in Section 4.1.1. In general the moment r of the size class M is defined as the sum of the probability density function and size distribution:

$$M_r = \sum_{i=1}^{\infty} x_i^r p_i \tag{2.8}$$

where x_i^r is random variable, e.g. the mass of the particles in size class i, the PAH and p_i the probability density function, e.g. the number density of the particles in size class i. The physical interpretation of the variables will be discussed in the following sections. The method of moments is valid if the sum converges. The first and second moments have mathematical and physical meanings. The first moment

$$M_1 = \sum_{k=1}^{\infty} x_k p_k \tag{2.9}$$

is the expectation value of M, and the second moment:

$$M_2 = \sum_{k=1}^{\infty} x_k^2 p_k \tag{2.10}$$

is the variance of M. They may also be interpreted in a physical context as will be shown in Section 2.3.
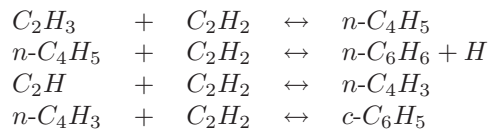
2.2 The Gas Phase Reactions

The formation of soot particles starts out with heterogeneous reactions in the gas phase, where the first nucleus is built. Those reactions, the formation of the first polyaromatic hydrocarbons and the further growth of the PAHs is described in this section.
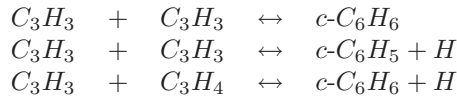
2.2.1   The Formation of PAHs

Extensive chemical mechanisms are involved when the first building blocks of soot, the cyclic polyaromatic hydrocarbons benzene $c\text{-}C_6H_6$ and phenyl $c\text{-}C_5H_6$, are formed. The mechanisms applied in this work are based on a mechanism developed by Warnatz et al. [51]. It includes H_2/O_2 chemistry and mechanism for $C_1\text{-}C_4$, as well as the formation of $H_2\text{-}CO$ and oxidation via O_2 and OH. The kinetics developed by Warnatz are valid for lean combustion conditions. They have been adjusted by Frenklach et al. [16] to rich combustion conditions, which are of special interest in soot formation (see Table 2.1). Frenklach included a mechanism which leads to the formation of cyclic polyaromatic hydrocarbons benzene and phenyl. The molecule mainly responsible for the process of growth of the rings is acetylene. The mechanism was developed by Frenklach and Mauss [104, 108]: Another path for the formation

Table 2.1: Reactions with acetylene, which is mainly responsible for the growth of PAH and soot.

$$
\begin{array}{lclcl}
C_2H_3 & + & C_2H_2 & \leftrightarrow & n\text{-}C_4H_5 \\
n\text{-}C_4H_5 & + & C_2H_2 & \leftrightarrow & n\text{-}C_6H_6 + H \\
C_2H & + & C_2H_2 & \leftrightarrow & n\text{-}C_4H_3 \\
n\text{-}C_4H_3 & + & C_2H_2 & \leftrightarrow & c\text{-}C_6H_5
\end{array}
$$

of benzene in fuel-rich high-temperature domains is via the species propagyl (C_3H_3) [109, 110, 111, 112] as shown in Table 2.2: Soot particles in flames

Table 2.2: C_3 reactions.

$$
\begin{array}{lclcl}
C_3H_3 & + & C_3H_3 & \leftrightarrow & c\text{-}C_6H_6 \\
C_3H_3 & + & C_3H_3 & \leftrightarrow & c\text{-}C_6H_5 + H \\
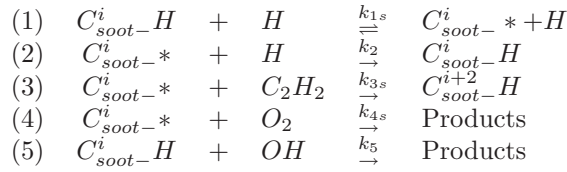C_3H_3 & + & C_3H_4 & \leftrightarrow & c\text{-}C_6H_6 + H
\end{array}
$$

are subjected to formation as well as reduction processes. Hydrocarbons which were formed during the formation of benzene and phenyl are reduced in oxidation via O_2 (see Table 2.3) and OH. Since flame velocities and species profiles are affected by these processes it is important to include a detailed description of the oxidation of higher order hydrocarbons. Slagle et al. [113] , Warnatz [51] and Westmoreland [114] have studied these processes. In the present work the detailed chemical reaction scheme of Chiang et al. [115] and Balthasar [116] was applied in the reaction mechanism. In this work two different were fuels were considered, acetylene/nitrogen and ethylene. The chemical reactions for

Table 2.3: Oxidation in reaction with O_2.

$$
\begin{array}{llllllll}
n\text{-}C_4H_3 & + & O_2 & \rightarrow & C_2H & + & HCO & + & HCO \\
I\text{-}C_4H_3 & + & O_2 & \rightarrow & C_2H & + & CH_2O & + & CO
\end{array}
$$
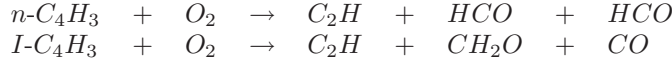
both fuels rely on the mechanism described above. A detailed description of the mechanism can be found in [108].

2.2.2   Growth of PAHs

After small polyaromatic hydrocarbons benzene $c\text{-}C_6H_6$ and phenyl $c\text{-}C_6H_5$ are formed they grow in further reaction with the gas phase species. This growth is a chemical process, beginning with one stable PAH, and can be described by a complicated chemical mechanism. Instead, Frenklach [16, 117] divided the growth of PAHs into different stages, associated with different size classes of PAHs. Growth from one size class to the next is assumed to be identical. The reversible reactions repeat in cycles of growth (Figure 2.1). The mechanism can be restricted to the so-called HACA mechanism, Table 2.4, which is a reversible reaction scheme. This describes the growth of a PAH by hydrogen abstraction through reactions with H, O or OH, acetylene addition, further hydrogen abstraction, followed by the addition of an acetylene molecule, which completes the next ring on the PAH (Figure 2.2).

Table 2.4: The HACA mechanism.

$$
\begin{array}{cllclcl}
(1) & C^i_{soot-}H & + & H & \overset{k_{1s}}{\underset{}{\rightleftharpoons}} & C^i_{soot-}*+H \\
(2) & C^i_{soot-}* & + & H & \overset{k_2}{\rightarrow} & C^i_{soot-}H \\
(3) & C^i_{soot-}* & + & C_2H_2 & \overset{k_{3s}}{\rightarrow} & C^{i+2}_{soot-}H \\
(4) & C^i_{soot-}* & + & O_2 & \overset{k_{4s}}{\rightarrow} & \text{Products} \\
(5) & C^i_{soot-}H & + & OH & \overset{k_5}{\rightarrow} & \text{Products}
\end{array}
$$

The statistical method of moments is used to solve the size distribution. One general reaction rate, $P_{i,j}$, is introduced. It employs the translation from one stage to the next, where i denotes the size class and j one stage of the molecular structure in the polymerization cycle. The resulting set of equations has the dimension of the number of distinct chemical structures within one cycle. Mauss [108] suggested reducing the system even more by introducing the method of fast polymerization, which implies that the PAHs are in a steady state.
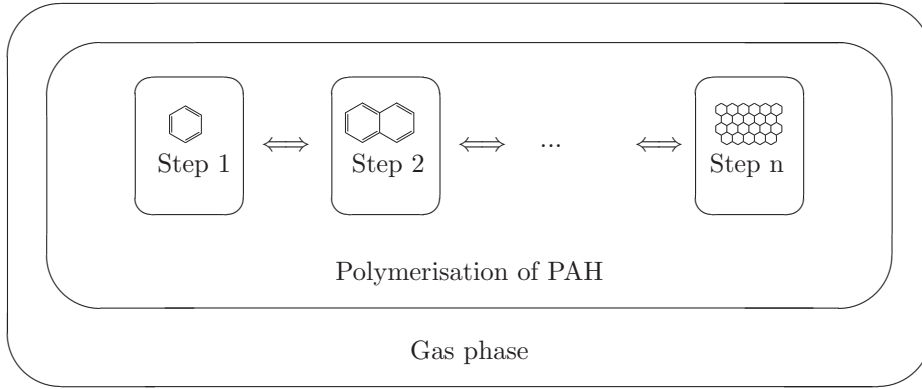
$$
\frac{\partial [P_{i,j}]}{\partial t} = 0 \tag{2.11}
$$

Figure 2.1: The growth of PAH by the method of linear lumping.

This approach reduces the polymerization reactions and thereby the computational effort required for the calculation of the moments of the size distribution. The rth moment of the PAH size distribution is defined as:

$$[M_r^{PAH}] = \sum_{i=1}^{\infty} \sum_{j=1}^{6} n_{i,j}^r [P_{i,j}] \qquad r = 0, 1, ...\infty \qquad (2.12)$$

where $n_{i,j}^r$ is the number of monomer units, which is one C-atom and $[P_{i,j}]$ the concentration of the PAH structure j at stage i. The transport equation for the density-weighted moments $\overline{M}_r^{PAH}$ for a laminar premixed flame is given by Balthasar [116].

$$\rho v \frac{\partial \overline{M}_r^{PAH}}{\partial x} - \frac{\partial}{\partial x} (\rho D_1) \frac{\partial}{\partial x} \overline{M}_{r-2/3}^{PAH} = \sum_{i=1}^{\infty} \sum_{j=1}^{6} n_{i,j}^r L \left(\overline{Y}(P_{i,j}) \right) \qquad (2.13)$$

where $L \left(\overline{Y}(P_{i,j}) \right)$ is the convective diffusive operator of the PAH moment continuity equation.

$$L \left(\overline{Y}(P_{i,j}) \right) = r_{pi} + r_{con} + r_{reac} \qquad (2.14)$$

It is balanced by the source terms of particle inception, condensation and the chemical reactions.
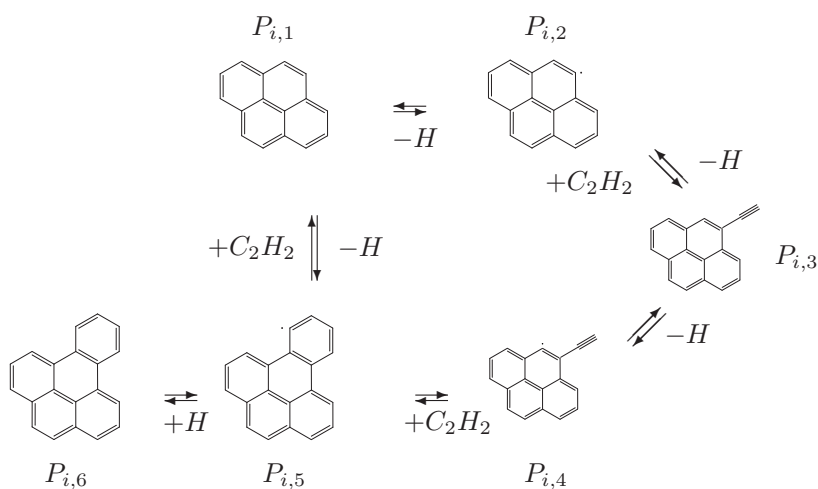
Figure 2.2: HACA mechanism of growth.

2.3   The Soot Model

The formation of soot particles in this work is assumed to go on in seven different steps via reactions with molecules in the gas (Figure 1.11). The modelling of the separate steps to soot formation will be studied closely in this section. Gas phase reactions and the formation of two dimensional PAHs proceed the first step of soot formation.

1. Inception of particles is the initial step of soot formation, where the first and the smallest soot nucleus is built. Particle inception describes the process where two two-dimensional PAHs, which were formed in the gas phase, merge into one three-dimensional particle.

2. Condensation: Here the gas phase reactions are not explicitly involved. One two-dimensional PAH condense on a three-dimensional PAH. The process involves collisions of molecular structures of different sizes.

3. Surface growth: involve heterogenous reactions with molecules in the gas. Acetylene, C_2H_2, has been shown to dominate this process of growth. Surface growth is dependent on the constituency of the surface, which will be shown to be strongly model dependent.

4. Coagulation: This process describes the merging of two spherical soot particles into one larger spherical soot particle. The process is treated statistically.

5. Agglomeration: Large clusters of particles are formed in this process. The soot particles are not assumed to be spherical anymore. The particles turn into fractal shapes.

6. Oxidation: The soot particle looses mass in heterogenous reactions with gas phase molecules O_2 and OH. The reactions lead to abstraction of a hydrogen radical.

Even in this context the method of moments (see Section 2.1.2) is used to describe the size distribution of the soot particles. The rth moment of the size distribution function is defined as a function of the particle i and the number density of particle i with the mass given by:

$$m_i = i \cdot m_1 \tag{2.15}$$

where m_1 is the mass of the smallest soot particle.

$$M_r = \sum_{i=1}^{\infty} m_i^r N_i \tag{2.16}$$

The particle mass, m_i, is the physical interpretation of the random variable, x_i, presented earlier and the number density, N_i, corresponds to the probability density function, p_i. The first moment, M_0, is defined below:

$$M_0 = \sum_{i=1}^{\infty} N_i = N \tag{2.17}$$

The physical interpretation of this variable is the total particle density. The second moment, M_1, is of interest as well, as it resolves the soot volume fraction.

$$M_1 = \sum_{i=1}^{\infty} i N_i = f_V \frac{\rho}{m_1} \tag{2.18}$$

A transport equation for the density-weighted moments of the size distribution, $^{\mathbf{S}}\overline{M}_r$, can be defined analogously to the previous chapter:

$$\rho v \frac{\partial \, ^{\mathbf{S}}\overline{M}_r}{\partial x} - \frac{\partial}{\partial x} \left(\rho D_{p,1} \right) \frac{\partial}{\partial x} \, ^{\mathbf{S}}\overline{M}_{r-2/3} \tag{2.19}$$
$$+ \frac{\partial}{\partial x} \left(0.55 \rho v \frac{1}{T} \frac{\partial T}{\partial x} \, ^{\mathbf{S}}\overline{M}_r \right) \quad = L \left(\, ^{\mathbf{S}}\overline{M}_r (N_A) \right)$$

$L\left(\ ^{\mathbf{S}}\overline{M}_r(N_A)\right)$ is the source term of the rth moment:

$$L\left(\ ^{\mathbf{S}}\overline{M}_r(N_A)\right) = \ ^{\mathbf{S}}\dot{M}_{r,pi} + \ ^{\mathbf{S}}\dot{M}_{r,con} + \ ^{\mathbf{S}}\dot{M}_{r,coag} \qquad (2.20)$$
$$+ \ ^{\mathbf{S}}\dot{M}_{r,sg} + \ ^{\mathbf{S}}\dot{M}_{r,ox}$$

where: pi = particle inception, con = condensation, $coag$ = coagulation, forming either spherical or fractal particles, sg = surface growth and ox = oxidation.

2.3.1   Inception of Particles

Particle inception describes the initial step of soot formation in which the first particle is formed. The gas phase is left behind and the phase of condensed material is entered when two two-dimensional PAHs merge and form the first three-dimensional structure. The size of this first particle is still a matter of discussion. As mentioned above the latest experimental techniques are used to define the smallest soot particle [80]. The Smoluchowski equation describes the interaction of two PAHs of the same type as is the case in particle inception. The transient particle number for each size class, i, is described by Equation 2.21. The equation consists of a particle-producing term and a particle-consuming term. Particles of size class i are produced when two particles of smaller size, class $i - k, 0 < k \leq i$, merge. Particles of larger size class $i + k, 0 \leq k < N - i$, are produced by consuming particles of size class i.

$$\dot{N}_i = \frac{1}{2}\underbrace{\sum_{j=1}^{i-1}(\beta_{j,i-j}N_jN_{i-j})}_{Production\ of\ particles}\ -\ \underbrace{\sum_{j=1}^{\infty}(\beta_{j,i}N_iN_j)}_{Consumption\ of\ particles} \qquad (2.21)$$

The frequency factor $\beta_{j,i-j}$ is a probability weight for the production of particles of size class i by particles of size class j and $i-j$. Factor $\beta_{i,j}$ is a probability weight for the consumption of particles of size class i by particles of size class j and i. The frequency factor is given by:

$$\beta_{i,j} = \epsilon_{ij}\sqrt{\frac{8\pi k_B T}{\mu_{i,j}}}(r_i + r_j)^2 \qquad (2.22)$$

where k_B is the Stefan Bolzmann constant, $\mu_{i,j}$ the reduced mass, r_i the radius of particles in class i and finally ϵ_{ij} is the size-dependent Van der Waals enhancement factor due to either the attractive or repulsive forces between the particles. However, this section deals with the inception of particles which

is a growth process. Therefore, only the production of particles in class i is considered:

$$\dot{N}_{i,pi} = \frac{1}{2} \sum_{j=1}^{i-1} (\beta_{j,i-j} N_j N_{i-j}) \tag{2.23}$$

Frenklach et al. [117] suggested replacing the Smoluchowsky equation for all particle size classes by the statistical method of moments of size distribution for the particles. Multiplying Equation 2.23 by i^r and summing over all size classes results in the following formulation of the PAH size distribution.

$$^s\dot{M}_{r,pi} = \frac{1}{2} \sum_{i=1}^{\infty} \sum_{j=1}^{\infty} ((i+j)^r \beta_{i,j} \, ^P N_i \, ^P N_j) \tag{2.24}$$

The well-known relation between particle volume, V_i, particle mass, m_i, and soot density, $\rho_{\mathbf{S}}$:

$$V_i = \frac{m_i}{\rho_{\mathbf{S}}} = i\frac{m_1}{\rho_{\mathbf{S}}}$$

leads to the following definition of the frequency factor:

$$\beta_{i,j} = C \cdot \sqrt{\frac{i+j}{ij}} (i^{1/3} + j^{1/3})^2 \tag{2.25}$$

where:

$$C = \epsilon_{i,j} \sqrt{\frac{6k_B T}{\rho_{\mathbf{S}}}} \left(\frac{3m_1}{4\pi\rho_{\mathbf{S}}} \right)^{1/6} \tag{2.26}$$

Kennedy et al. [101] set the Van der Waals enhancement factor for particle inception, condensation and coagulation, $\epsilon_{i,j} = 2.2$, which leads to the C factor given below.

$$C = 2.2 \cdot \sqrt{\frac{6k_B T}{\rho_{\mathbf{S}}}} \left(\frac{3m_1}{4\pi\rho_{\mathbf{S}}} \right)^{1/6} \tag{2.27}$$

The PAHs involved in particle inception are assumed to be members of the same size class $i = j$, based on the smallest unit, carbon monomers. This leads to the following frequency factor.
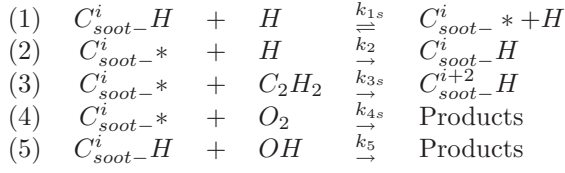
$$\beta_{i,j} = \sqrt{32} \cdot C \cdot i^{1/6} \tag{2.28}$$

The source terms for the moments with respect to particle inception can be formulated as a function of the moments for the soot particle and PAH size distribution. P denotes the PAH distribution:

$$^{\mathbf{s}}\dot{M}_{r,pi} = \frac{1}{2} C \sum_{k=0}^{r} \binom{r}{k} (^P M_{k+\frac{1}{6}}^P M_{r-k}) \tag{2.29}$$

The moments $^P M_0 - ^P M_r$ result in the fast polymerization model for PAH growth. Moments of fractional order are obtained by Lagrange interpolation.

2.3.2 Condensation

Condensation is the process in which one two-dimensional PAH join onto a three-dimensional soot particle. As for particle inception, the Smoluchowsky equation is used to describe this process.

$$\dot{N}_{i,con} = \underbrace{\sum_{j=1}^{i-1} (\beta_{j,i-j} \, ^P N_j \, ^{\mathbf{S}} N_{i-j})}_{Production\ term} - \underbrace{\sum_{j=1}^{\infty} (\beta_{j,i} \, ^{\mathbf{S}} N_i \, ^P N_j)}_{Consumption\ term} \qquad (2.30)$$

$$^{\mathbf{S}}\dot{M}_{i,con} = \sum_{i=1}^{\infty} \sum_{j=1}^{\infty} (i+j)^r \beta_{j,i} \, ^P N_j \, ^{\mathbf{S}} N_{i-j}) - \sum_{i=1}^{\infty} \sum_{j=1}^{\infty} (i^r \beta_{j,i} \, ^{\mathbf{S}} N_i \, ^P N_j) \quad (2.31)$$

Condensation describes the interactions between particles of different size classes. Assuming that one of the particles is much larger that the other ($i \gg j$) the collision frequency is given by:

$$\beta_{i,j} = C j^{-\frac{1}{2}} i^{\frac{2}{3}} \qquad (2.32)$$

The resulting source terms for the moments with respect to condensation can be formulated as a function of the moments for the soot particle and PAH size distribution.

$$^{\mathbf{S}}\dot{M}_{r,con} = C \sum_{k=0}^{r-1} \binom{r}{k} (^P M_{k+\frac{1}{6}}^P M_{r-k}) \qquad (2.33)$$

2.3.3 Surface Growth and Oxidation

Surface growth and oxidation are heterogeneous reactions in which the soot particles interact with the gas phase to either gain or reduce mass. Different approaches have been undertaken to define the rate of surface growth. The models are based on the assumption that the rate of surface growth is dependent on either the soot volume fraction, or on the surface area of the soot particles. In the latter case the fractal dimension of the surface is of relevance. Wagner [118] gave an empirical expression of the rate of surface growth as a function of soot volume fraction, f_v:

$$\frac{df_v}{dt} = k(f_{v,\infty} - f_v) \qquad (2.34)$$

Table 2.5: The HACA-mechanism

$$
\begin{array}{llllll}
(1) & C^i_{soot-}H & + & H & \overset{k_{1s}}{\rightleftharpoons} & C^i_{soot-}*+H \\
(2) & C^i_{soot-}* & + & H & \overset{k_2}{\rightarrow} & C^i_{soot-}H \\
(3) & C^i_{soot-}* & + & C_2H_2 & \overset{k_{3s}}{\rightarrow} & C^{i+2}_{soot-}H \\
(4) & C^i_{soot-}* & + & O_2 & \overset{k_{4s}}{\rightarrow} & \text{Products} \\
(5) & C^i_{soot-}H & + & OH & \overset{k_5}{\rightarrow} & \text{Products}
\end{array}
$$

where k is the empirical rate constant for the surface reactions and $f_{v,\infty}$ is the final value of the soot volume fraction. A model based on the soot surface has been presented by Harries and Weiner [119]. This empirical formulation of the rate of surface growth was found to be:

$$
\rho \frac{df_v}{dt} = k_S S [C_2 H_2] \tag{2.35}
$$

where k_S is the empirical rate constant for the surface reactions, S is the surface area of the soot particle and ρ the soot density. It was shown that the rate of surface growth decreases with increasing size of the particle, which coincides with the age of the particle. A chemical reaction path for the surface reactions has been given by Frenklach and Wang [104]. The principle of active sites on soot particles was introduced in this context. The active site parameter indicates the reaction activity of the soot surface and allows the particle to take part in the gas phase reactions. An active site on the surface of the soot particle is a C atom, bound to a hydrogen radical, namely the atom C^i_{soot-H} and the radical active site C^i_{soot-*}. The surface reaction constants are then obtained from the PAH reactions. The growth rate can be formulated as follows.

$$
\rho \frac{df_v}{dt} = k_3 [C_2 H_2][C^i_{soot-*}] \tag{2.36}
$$

Assuming that the reaction with the surface is fast, and assuming that the concentration of the active radical sites is in steady state, the concentration can be determined.

$$
[C^i_{soot-*}] = \left(\frac{k_{1,f}[H]}{k_{1,b}[H_2] + k_2[H] + k_3[C_2H_2] + k_4[O_2]} \right) \cdot [C^i_{soot-H}] \tag{2.37}
$$

The concentration of active sites, $C^i_{soot}H\chi$, on the soot surface, which is the sum of $[C^i_{soot-*}]$ and $[C^i_{soot-H}]$, can be calculated with the help of the surface density, S, the number of sites, χ_{soot}, and the fraction of active sites, α:

$$
C^i_{soot_\chi} = \frac{\chi_{soot}}{N_A} \alpha S \tag{2.38}
$$

Table 2.6: The HACARC-mechanism.

(1.a)	$C_{soot,i}H$	$+$	H	$\overset{k_{1a}}{\rightleftharpoons}$	$C^*_{soot,i}$	$+H_2$		
(1.b)	$C_{soot,i}H$	$+$	OH	$\overset{k_{1b}}{\rightleftharpoons}$	$C^*_{soot,i}$	$+H_2O$		
(2)	$C^*_{soot,i}$	$+$	H	$\overset{k_2}{\rightarrow}$	$C_{soot,i}H$			
(3.a)	$C^*_{soot,i}$	$+$	C_2H_2	$\overset{k_{3a}}{\rightleftharpoons}$	$C_{soot,i}C_2H_2$			
(3.b)	$C_{soot,i}C_2H_2$	$+$		$\overset{k_{3b}}{\rightleftharpoons}$	$C_{soot,i+1}H$	$+H$		
(4.a)	$C^*_{soot,i}$	$+$	O_2	$\overset{k_{4a}}{\rightarrow}$	$C^*_{soot,i-1}$	$+2CO$		
(4.b)	$C_{soot,i}C_2H_2$	$+$	O_2	$\overset{k_{4b}}{\rightarrow}$	$C^*_{soot,i}$	$+2CHO$		
(5)	$C_{soot,i}H$	$+$	OH	$\overset{k_5}{\rightarrow}$	$C^*_{soot,i-1}$	$+CH$	$+CHO$	
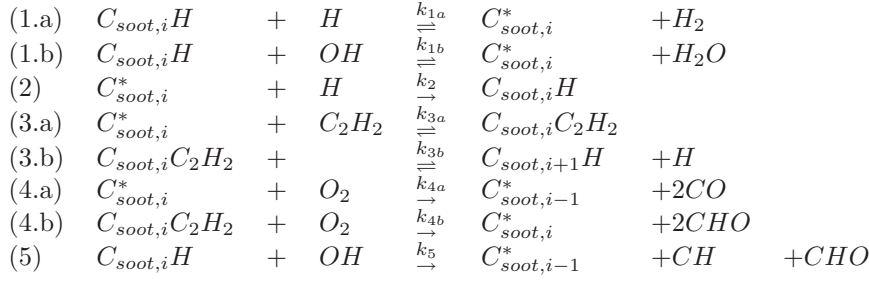
where:

$$S = \sum_{i=1}^{\infty} S_i N_i \tag{2.39}$$

In this work the HACARC mechanism (see Table 2.6), the so-called hydrogen-abstraction-carbon-addition-ring-closure-mechansim described by Mauss [120] was used:

The concentration of the active radical sites, C^*_{soot}, and $C^*_{soot}C_2H_2$, is found, as mentioned previously, based on the assumption of a quasi-stationary state:

$$[C_{soot}] = \sum_{i=1}^{\infty} \alpha \frac{\chi_{soot}}{N_A} S_i N_i \tag{2.40}$$

where S_i is the surface area and N_i the number density of particles of size class i. α is the fraction of the active sites available for chemical reactions. α is a steric factor, that accounts for the probability of the gaseous species colliding with the reactive prismatic planes of a soot particle [121]. It was found to quantify the temperature dependent morphology of the soot particles [122]. The value of α is still a matter of discussion and will be considered in Chapter 4. Appel et al. [122] developed a temperature formulation of the active site parameter for premixed flames:

$$\alpha = \tanh\left(\frac{a}{\log \mu_1} + b\right) \tag{2.41}$$

where μ_1 is the first size moment of the soot particle distribution, and a and b are fitted parameters given by:

$$a = 12.65 - 56.3 \cdot 10^{-4} \cdot T \tag{2.42}$$

and

$$b = -1.38 + 6.8 \cdot 10^{-4} \cdot T \qquad (2.43)$$

As mentioned above the surface annealing of aging soot particles is a result of a decreasing H atom concentration and the ensuring reduction in radical sites [104]. Frenklach and Wang [104] claimed that α must decrease with temperature. They argued that at high temperatures soot particle crystallites align themselves in such a way that the active sites of neighbouring crystallites face each other, and thereby thus the access of gaseous species. Each benzene molecule contained in a soot particle is assumed to have one active site, $\chi_{soot}S_1$, which results in the following expression for the active sites:

$$\chi_{soot}S_i = \chi_{soot}S_1 i^{2/3} = i^{2/3} \qquad (2.44)$$

where i is the size class of the molecule. The source terms of surface growth and oxidation for the soot moments follow the formulation of Balthasar [116]:

$$^S\dot{M}_{0,sg} = 0 \qquad (2.45)$$

$$^S\dot{M}_{r,sg} = \alpha \, k_{3a,f} \, [C_2H_2] \, f_{3a} A \qquad (2.46)$$

$$\cdot \sum_{k=0}^{r-1} \binom{r}{k} {}^S M_{k+\frac{2}{3}} 2^{r-k}, \quad r = 1, 2, ...$$

and for oxidation:

$$^S\dot{M}_{0,ox} = -\alpha(k_{4a}[O_2]A + k_5[OH])N_x \qquad (2.47)$$

$$^S\dot{M}_{r,ox} = \alpha(k_{4a}[O_2]A + k_5[OH]) \qquad (2.48)$$

$$\cdot \sum_{k=0}^{r-1} \binom{r}{k} {}^S M_{k+\frac{2}{3}} (-2)^{r-k}, \quad r = 1, 2, ...$$

where:

$$A = \frac{k_{1a,f}[H] + k_{1b,f}[H] + k_5[OH]}{k_{1a,b}[H_2] + k_{1b,b}[H_2O] + k_2[H] + k_{3a,f}[C_2H_2] + k_{4b}[O_2]} \qquad (2.49)$$

In order to achieve closure of the system the number density of the smallest size class must be known. Hence, the probability of the burn-out of the soot particles is assumed to be proportional to the mean particle size. This results in a rate of oxidation for the zeroth moment:

$$^S\dot{M}_{,ox} = -(k_{4a}[O_2]A + k_5[OH])^S M_{-\frac{1}{3}} \qquad (2.50)$$

2.3.4   Coagulation

Coagulation is the merging of two spherical particles into one larger spherical particle. The number density decreases in this process while the soot volume fraction remains constant. It is still unclear if small or large particles are responsible for the coagulation process [109, 110, 111]. However, when describing coagulation, three different cases must be considered. They are connected to the "crowdedness" of the space, which is expressed by the Knudsen number:

$$Kn = \frac{2\lambda}{d} \tag{2.51}$$

d is the diameter of the particles, and λ is the mean free path.

1. The free molecular regime, $Kn \gg 1$: The path between the particles is much larger than the particle diameter. The particles in this regime are free to move around.

2. The transition regime, $0.1 < Kn < 10$: This is the state between the free molecular and the continuum regime.

3. The continuum regime, $Kn \ll 1$: The path between the particles is much smaller than the particle diameter. The regime is quite crowded. The movement in this regime is close to a continuous flow.

However, the Smoluchowski equation 2.21 is valid in all three regimes, with collision frequencies adjusted to the crowdedness of the regime.

$$\dot{N}_{i,coag} = \frac{1}{2} \sum_{j=1}^{i-1} (\beta_{j,i-j} \, {}^{\mathbf{s}}N_j \, {}^{\mathbf{s}}N_{i-j}) - \sum_{j=1}^{\infty} (\beta_{j,i} \, {}^{\mathbf{s}}N_i \, {}^{\mathbf{s}}N_j) \tag{2.52}$$

The coagulation in terms of the statistical moments of the soot particle size distribution is given below.

$${}^{\mathbf{s}}\dot{M}_{i,coag} = \sum_{i=1}^{\infty} \sum_{j=1}^{\infty} ((i+j)^r \beta_{j,i} \, {}^{\mathbf{s}}N_j \, {}^{\mathbf{s}}N_{i-j}) - \sum_{i=1}^{\infty} \sum_{j=1}^{\infty} (i^r \beta_{i,j} \, {}^{\mathbf{s}}N_i \, {}^{\mathbf{s}}N_j) \tag{2.53}$$

Coagulation in the free molecular regime

The Knudsen number in this regime is much greater than unity, and the particles are free to move. The particle size ranges from $i = 0$ to $i = \infty$. The collision frequency in this regime is given by Equation 2.27 and:

$$\beta_{i,j}^f = C\sqrt{\frac{i+j}{ij}} \tag{2.54}$$

In order to obtain closure, Frenklach et al. [117] introduced a function $\langle \Phi_{x,y} \rangle$ and reformulated the source terms of the coagulation for the soot moments:

$$^{\mathbf{s}} \dot{M}^f_{r,coag} = \frac{1}{2} \sum_{k=1}^{r-1} \binom{r}{k} \langle \Phi_{x,y} \rangle \, {}^{\mathbf{s}} M_0^2 \qquad (2.55)$$

where:

$$\langle \Phi_{x,y} \rangle = C \langle \, f_{x,y} \rangle \qquad (2.56)$$

and $\langle \, f_{x,y} \rangle$ is obtained by $f_{x,y}$ through the following relation:

$$f_{x,y} = \sum_{i=1}^{\infty} \sum_{j=1}^{\infty} (i+j)^r \frac{(i^{\frac{1}{3}} + j^{\frac{1}{3}})^2}{\sqrt{ij}} i^x j^y n_i n_j \qquad (2.57)$$

where $n_i = \frac{N_i}{^{\mathbf{s}} M_0}$ is the fraction of particles of size class i related to the sum of all particles. $^r f_{x,y}$ (Equation 2.58) is a term of the fractional moments $\mu_r = \frac{^{\mathbf{s}} M_r}{^{\mathbf{s}} M_0}$. It is be obtained by applying Lagrange interpolation between the logarithms of $^0 f_{x,y},^1 f_{x,y},^2 f_{x,y}, \dots \, ^r f_{x,y}$, $r = 0, 1, 2, \dots$ [116].

$$^r f_{x,y} = \mu_{(k+x+\frac{1}{6})} \mu_{(r+y-k-\frac{1}{2})} + 2\mu_{(k+x-\frac{1}{6})} \mu_{(r+y-k-\frac{1}{6})} \qquad (2.58)$$
$$+ \mu_{(k+x-\frac{1}{2})} \mu_{(r+y-k+\frac{1}{6})}$$

Coagulation in the continuum regime

The Knudsen number in this regime is much less than unity and we are dealing with a continuous flow. The collision frequency in this regime is given by:

$$\beta^c_{ij} = K \left(\frac{\mathcal{C}_i}{i^{\frac{1}{3}}} + \frac{\mathcal{C}_j}{j^{\frac{1}{3}}} \right) (i^{\frac{1}{3}} + j^{\frac{1}{3}}) \qquad (2.59)$$

where c denotes the continuum regime and:

$$K = \frac{2k_B T}{3\eta} \qquad (2.60)$$

where η is the viscosity of the gas, and the Cunningham slip correction factor, $\mathcal{C}_i$, is given by:

$$\mathcal{C}_i = 1 + 1.257 Kn(i) \qquad (2.61)$$

Van der Waals forces are small in this regime [123], which is the reason why no enhancement factor is included. The source terms for the coagulation of soot

particles in terms of the moments are given by:

$$
\begin{aligned}
{}^{\mathbf{s}}\dot{M}^c_{r,coag} &= \frac{1}{2}K\sum_{k=1}^{r-1}\binom{r}{k}\cdot\Bigg[2\,{}^{\mathbf{s}}M_k\,{}^{\mathbf{s}}M_{(r-k)} \\
&+ \quad {}^{\mathbf{s}}M_{(k+\frac{1}{3})}\,{}^{\mathbf{s}}M_{(r-k-\frac{1}{3})} + {}^{\mathbf{s}}M_{(k-\frac{1}{3})}\,{}^{\mathbf{s}}M_{(r-k+\frac{1}{3})} \\
&+ \quad 2.514\lambda\left(\frac{\pi\rho_s}{6m_1}\right)^{\frac{1}{3}}\cdot\Bigg({}^{\mathbf{s}}M_{(k-\frac{1}{3})}\,{}^{\mathbf{s}}M_{(r-k)} \\
&+ \quad {}^{\mathbf{s}}M_{(k)}\,{}^{\mathbf{s}}M_{(r-k-\frac{1}{3})} + {}^{\mathbf{s}}M_{(k+\frac{1}{3})}\,{}^{\mathbf{s}}M_{(r-k-\frac{2}{3})} \\
&+ \quad {}^{\mathbf{s}}M_{(k-\frac{2}{3})}\,{}^{\mathbf{s}}M_{(r-k+\frac{1}{3})}\Bigg)\Bigg]
\end{aligned}
\tag{2.62}
$$

Coagulation in the transition regime

The Knudsen number in this regime is between 0.1 and 10. This state is between the free molecular and the continuum regimes. The semi-empirical formula of Fuchs [124] was developed to describe the coagulation in the transient regime:

$$
\tilde{\beta}_{ij} = \tilde{\beta}^c_{ij}\left[\frac{\frac{1}{Kn(i)}+\frac{1}{Kn(j)}}{\frac{1}{Kn(i)}+\frac{1}{Kn(j)}+2\sqrt{\tilde{\delta}_i^2+\tilde{\delta}_j^2}}+\zeta\frac{\tilde{\beta}^c_{ij}}{\tilde{\beta}^f_{ij}}\right]^{-1}
\tag{2.63}
$$

where:

$$
\zeta = \frac{1}{3}\sqrt{\frac{K\rho}{\lambda\eta}}
$$

$$
\tilde{\delta} = \frac{1}{Kn}\left[\frac{(1+\frac{\pi}{\zeta C\sqrt{Kn}})^3-(1+(\frac{\pi}{\zeta C\sqrt{Kn}})^2)^{3/2}}{3\left(\frac{\pi}{\zeta C\sqrt{Kn}}\right)^2}-1\right]
$$

$$
\tilde{\beta}^f_{ij} = \sqrt{Kn(i)^3+Kn(j)^3}\left(Kn(i)^{-1}+Kn(j)^{-1}\right)^2
$$

$$
\tilde{\beta}^c_{ij} = \sqrt{C_iKn(i)+C_jKn(j)}\left(Kn(i)+Kn(j)\right)\left(C_iKn(i)+C_jKn(j)\right)
$$

A simpler approach was applied by Frenklach [106], inspired by Partsinis [125], who approximated the coagulation rate of particles of the same size by the harmonic mean of the continuum and the free molecular rate. Frenklach [106] first extended the approach to a wide particle size distribution.

$$
{}^{\mathbf{s}}\dot{M}_{r,coag} = \frac{{}^{\mathbf{s}}\dot{M}^f_{r,coag}\,{}^{\mathbf{s}}\dot{M}^c_{r,coag}}{{}^{\mathbf{s}}\dot{M}^f_{r,coag}+{}^{\mathbf{s}}\dot{M}^c_{r,coag}}, \qquad r=0,2,3,4...
\tag{2.64}
$$

2.3.5   Agglomeration

After having reached a critical diameter, d_c, soot particles join and form agglomerates, which are large chain-like soot structures. Agglomerates are clusters of at least two primary particles, which differ in size and shape. Soot particles denominate primary particles as well as agglomerates. The number density of primary particles remains constant when agglomerates are formed. A large number of experimental studies aimed at measuring parameters describing the shape and size of agglomerates, have been undertaken since the 1980s [21, 22, 23, 96, 126, 127, 128, 129]. Frenklach and Kazakov [106] made the first attempt to include this process into their existing model. Their method is based on the assumption that agglomerates are composed of spherical equal-sized primary particles. It is necessary to differentiate between the formation of primary particles on the one hand and the formation of the agglomerates on the other. Agglomerates are subjected to soot formation processes such as condensation of PAH's, surface growth and coagulation with other primary particles and other agglomerates, as well as soot reduction processes such as oxidation via O_2 and OH. The number of primary particles in an agglomerate may be described via its radius of gyration [22], $R_g = \sqrt{\frac{1}{n}\sum_i r_i^2}$, where r_i is the distance of the ith primary particle from the centre of mass of the agglomerate.

$$n = k_f \left(\frac{2R_g}{d_p}\right)^{D_f} \tag{2.65}$$

where n is the number of primary particles in an aggregate, and D_f is the fractal or Hausdorf dimension. The fractal dimension has been found to be in the range $[1.7 - 2.07]$ [130, 127]. Equation 2.65 was found to be valid if $D_f \geq 2$, or if the aggregates have similar size [106]. Otherwise the collision frequency is overestimated since small particles sometimes pass through large agglomerates without adsorbing. Mandelbrot [131] denoted the first-order lacunarity or fractal prefactor, k_f as a parameter characterizing the aggregate density and cut-off of fractality. The lacunarity describes the gaps in the surface of the fractal shape of the agglomerate. d_p denotes the diameter of primary particles.

$$d_p = \left(\frac{6m_1 m}{\pi \rho n}\right)^{1/3} \tag{2.66}$$

Equation 2.65 is strictly only valid for large agglomerates. Dobbins at al. [132] demonstrated the validity of this statistical approach down to small-scale agglomerates containing about 5 particles. Particle agglomeration must be considered in two extremes:

1. The regime of particle coalescence, where particles are formed into perfect spheres.

2. The regime of agglomeration, where fractals are generated with the constants D_f and k_f.

The mean free path decreases with increasing pressure. This results in coagulation being transformed in to the transition and continuum regimes. Soot particles aggregate into fractal agglomerates. In simulating a non-premixed flame, the integration starts with the coalescent limit and changes to the aggregation limit when the critical diameter d_c is reached. Instead of instantaneously switching on the formation of agglomerates, the transformation into the regime of agglomerates is done slowly using a $tanh(\mathcal{D}(d_p))$ in order to avoid convergence problems (see Chapter 4). $\mathcal{D}(d_p) \propto d_p$ is a function of the particle diameter. Agglomerates are formed through the coagulation process where the particles form fractals. This can be modelled with the method of moments. Again the system has to be divided into three regions: the free molecular regime, the transition regime and the continuum regime.

Agglomeration formation in the free molecular regime

The collision frequencies for the free molecular regime, denoted with superscript f, are given by [106]:

$$\beta_{ij}^{f,a} = 2.2\sqrt{\frac{\pi k_B T}{2m_1}\left(\frac{1}{m_i} + \frac{1}{m_j}\right)}(d_{c,i} + d_{c,j})^2 \tag{2.67}$$

Similar to coagulation in the free molecular regime, described in Section 2.3.4, the source terms of the agglomeration for the soot moments may be formulated as functions of $\langle \Phi_{x,y} \rangle$:

$$^{\mathbf{s}}\dot{M}_{r,ac}^f = \frac{1}{2}\sum_{k=1}^{r-1}\binom{r}{k}\langle \Phi_{x,y} \rangle \, ^{\mathbf{s}}M_0^2 \tag{2.68}$$

where the subscript ac denotes agglomerate coagulation, and

$$\langle \Phi_{x,y} \rangle = C\langle f_{x,y}^l \rangle \tag{2.69}$$

where $\langle f_{x,y}^l \rangle$ is obtained through the following relation:

$$
\begin{aligned}
\langle f_{x,y}^l \rangle &= \frac{1}{M_0^2} \sum_{i=1}^{\infty} \sum_{j=1}^{\infty} (m_i + m_j)^l &&(2.70) \\
&\quad \cdot \left(m_i^{1/3} n_i^{1/D_f - 1/3} + m_j^{1/3} n_j^{1/D_f - 1/3} \right)^2 m_i^{x-1/2} m_j^{y-1/2} N_i N_j \\
&= \sum_{k=0}^{l} \binom{l}{k} \langle m^{x+k+1/6} n^{2/D_f - 2/3} \rangle \mu_{x+k-1/2} \\
&\quad + 2 \langle m^{x+k-1/6} n^{2/D_f - 1/3} \rangle \langle m^{y+l-k-1/6} n^{1/D_f - 1/3} \rangle \\
&\quad + \mu_{(x+k-1/2)} \langle m^{y+l-k+1/6} n^{2/D_f - 2/3} \rangle
\end{aligned}
$$

$\langle m^r n^{r'} \rangle$ are binary moments of a two-dimensional particle size distribution, which is a function of the mass of the agglomerate, m, and the number of primary particles in the agglomerate, n. The binary moments are approximated to functions of the particle mass moments, μ_r, and the number of primary particles, $\pi_{r'}$ [106]:

$$ \langle m^r n^{r'} \rangle \approx \langle m^r \rangle \langle n^{r'} \rangle = \mu_r \pi_{r'} \tag{2.71} $$

where the number of primary particles can be expressed by the moments of the primary particles, defined in Equation 2.77:

$$ \pi_r = \frac{P_r}{P_0} \tag{2.72} $$

The value of $\langle f_{x,y} \rangle$ is determined by Lagrange interpolation as described in Section 2.3.4 which leads to the following formulation of the term:

$$
{}^r f_{x,y} = \mu_{(k+x+\frac{1}{6})} \mu_{(r+y-k-\frac{1}{2})} + 2\mu_{(k+x-\frac{1}{6})} \mu_{(r+y-k-\frac{1}{6})} \tag{2.73}
$$
$$
+ \mu_{(k+x-\frac{1}{2})} \mu_{(r+y-k+\frac{1}{6})}
$$

Agglomeration in the continuum regime

The collision frequencies for the continuum regime, denoted with c, are given by [106]:

$$ \beta_{ij}^{c,a} = K \left(\frac{C_i}{d_{c,i}'} + \frac{C_j}{d_{c,j}'} \right) (d_{c,i} + d_{c,j})^2 \tag{2.74} $$

where K is defined in Equation 2.60. The particle diameter $d_{c,j}'$ is the mobility diameter [133]. In order to avoid discontinuity in $M_{r,ac}$ the suggestion of Kruis

et al. [134] is followed and the mobility diameter is equated to d_c.

$$
\begin{aligned}
M_{r,ac}^c \;=\; & \frac{1}{2}K\sum_{k=1}^{r-1}\binom{r}{k}\Big[2\mu_k\mu_{r-k} \\
+\; & \langle m^{k+1/3}n^{1/D_f-1/3}\rangle\langle m^{r-k-1/3}n^{1/3-1/D_f}\rangle \\
+\; & \langle m^{k-1/3}n^{1/3-1/D_f}\rangle\langle m^{r-k+1/3}n^{1/D_f-1/3}\rangle \\
+\; & 2.514\lambda\Big(\frac{\pi\rho}{6m_1}\Big)^{1/3}\Big(\langle m^{k-1/3}n^{1/3-1/D_f}\rangle\mu_{r-k} \\
+\; & \mu_k\langle m^{r-k-1/3}n^{1/3-1/D_f}\rangle \\
+\; & \langle m^{k+1/3}n^{1/D_f-1/3}\rangle\langle m^{r-k-2/3}n^{2/3-2/D_f}\rangle \\
+\; & \langle m^{k-2/3}n^{2/3-2/D_f}\rangle\langle m^{r-k+1/3}n^{1/D_f-1/3}\rangle\Big)\Big]M_0^2
\end{aligned}
\tag{2.75}
$$

Agglomeration in the transition regime

The transition regime is the intermediate regime between the free molecular and the continuum regime. As for the coagulation into spheres, Section 2.3.4, the formula of Kazakov and Frenklach [106] can be used to describe the coagulation in the transient regime.

$$
{}^{\mathbf{s}}\dot{M}_{r,ac} = \frac{{}^{\mathbf{s}}\dot{M}_{r,ac}^f \; {}^{\mathbf{s}}\dot{M}_{r,ac}^c}{{}^{\mathbf{s}}\dot{M}_{r,ac}^f + \; {}^{\mathbf{s}}\dot{M}_{r,ac}^c}, \qquad r = 0, 2, 3, 4...
\tag{2.76}
$$

Moments for primary particles.

In the regime of coalescence, the moments describe the size distribution of soot particles that coincide with the primary particles, since they consist of exactly one primary particle. Entering the regime of agglomeration, soot particles denominate agglomerates as well as single primary particles in the system. An additional source term for the primary particles in terms of the statistical moments must be introduced:

$$
P_r = \sum_{i=1}^{\infty} n_i^r N_i
\tag{2.77}
$$

where N_i is the concentration of the agglomerate size class i, n_i is the number of primary particles in size class i and $P_0 = M_0$ is the total number density of the soot particles in both regimes. For the regime of coalescence this implies that $n_i = 1$ and the moments of the primary particles, P_r, coincide with the zeroth soot moment and thus:

$$
P_r = P_0 = M_0
\tag{2.78}
$$

In the agglomeration regime particles consist of more than one primary particle, $n_i > 1$, and P_1 is the total number density of primary particles in the system. They are either free primary particles or joined in an agglomerate. The mean number of primary particles in an agglomerate $\bar{n}$ is given by:

$$\bar{n} = \frac{P_1}{P_0} \tag{2.79}$$

The source term for the primary particles in terms of the method of moments reads:

$$\dot{P}_r = R_0 + H_r, \qquad r = 2, 3, ... \tag{2.80}$$

where R_0 is the rate of particle formation described in the previous sections. The first moment is $\dot{P}_1 = R_0$, where R_0 is composed of the moments for particle inception and surface reactions such as oxidation [135]. H_r arises from the aggregate coagulation, with:

$$H_r = \frac{1}{2} \sum_{k=1}^{r-1} \binom{r}{k} \left(\sum_{i=1}^{\infty} \sum_{j=1}^{\infty} n_i^k n_j^{r-k} \beta_{ij}^a N_i N_j \right) \tag{2.81}$$

where the collision frequency differs for the different regimes.

Moments for primary particles in the free molecular regime: In the free molecular regime the moment for aggregate coagulation for the primary particles is:

$$H_r^f = \frac{1}{2} \langle \psi_r \rangle \tag{2.82}$$

with:

$$\frac{1}{2} \langle \psi_r \rangle = C \cdot \langle h_r \rangle \tag{2.83}$$

where C is given in Equation (2.27) and $\langle h_r \rangle$ can be determined from:

$$
\begin{aligned}
\langle h_r \rangle \;=\; & \sum_{k=0}^{l} \binom{r}{q} \Big(\langle m^{k+1/6} n^{q+2/D_f-2/3} \rangle \langle m^{l-k-1/2} n^{r-q} \rangle \\
& + \; 2 \langle m^{k-1/6} n^{q+1/D_f-1/3} \rangle \langle m^{l-k-1/6} n^{r-q+1/D_f-1/3} \rangle \\
& + \; \langle m^{k-1/2} n^q \rangle \langle m^{l-k-1/6} n^{r-q+2/D_f-2/3} \rangle \Big)
\end{aligned}
\tag{2.84}
$$

Agglomeration in the continuum regime: The statistical moments of the agglomerate coagulation in the continuum regime are similar to Equation 2.3.5.

$$
\begin{aligned}
H_r^f \;=\; & \frac{1}{2}K\sum_{k=1}^{r-1}\binom{r}{k}\Big[2\pi_k\pi_{r-k} \\[4pt]
& +\; \langle m^{1/3}n^{k+1/D_f-1/3}\rangle\langle m^{-1/3}n^{r-k+1/3-1/D_f}\rangle \\[2pt]
& +\; \langle m^{-1/3}n^{k+1/3-1/D_f}\rangle\langle m^{1/3}n^{r-k+1/D_f-1/3}\rangle \\[2pt]
& +\; 2.514\lambda\Big(\frac{\pi\rho}{6m_1}\Big)^{1/3}\Big(\langle m^{-1/3}n^{k+1/3-1/D_f}\rangle\pi_{r-k} \\[2pt]
& +\; \pi_k\langle m^{-1/3}n^{r-k+1/3-1/D_f}\rangle \\[2pt]
& +\; \langle m^{1/3}n^{k+1/D_f-1/3}\rangle\langle m^{-2/3}n^{r-k+2/3-2/D_f}\rangle \\[2pt]
& +\; \langle m^{-2/3}n^{k+2/3-2/D_f}\rangle\langle m^{1/3}n^{r-k+1/D_f-1/3}\rangle\Big)\Big]M_0^2
\end{aligned}
\tag{2.85}
$$

Moments for primary particles in the transition regime: The moments for the transition regime the harmonic mean is built as explained above.

$$
{}^{\mathbf{s}}\dot{H}_r = \frac{{}^{\mathbf{s}}\dot{H}_r^f\,{}^{\mathbf{s}}\dot{H}_r^c}{{}^{\mathbf{s}}\dot{H}_r^f + {}^{\mathbf{s}}\dot{H}_r^c}, \qquad r = 0,2,3,4...
\tag{2.86}
$$

Surface Reactions Although surface reactions were not studied explicitly in this work, they do affect the value of the soot volume fraction . As stated by Frenklach and Kazakov [106], the agglomeration of soot particles affects surface growth since the fractal surface of an agglomerate is larger than the surface of a spherical particle. If the entire surface of an aggregate were to be accessible for reactions to take place, meaning that the primary particles have point contact, then the surface of an agglomerate of size class i would be given by [106, 135]:

$$
S_i^a = n_i\,S_i^{pp} = \pi d_p^2 n_i = \pi\left(\frac{6m_c}{\pi\rho}\right)^{2/3}\frac{2}{3}n_i^{\frac{1}{3}}m_i^{\frac{2}{3}}
\tag{2.87}
$$

which leads to the number of active sites of:

$$
s_i^a = \alpha n_i^{\frac{1}{3}}i^{\frac{2}{3}}
\tag{2.88}
$$

Even though the surface of an agglomerate is larger than of spherical particles, the accessibility of the sites due to geometry could be expected to counterwork the reactivity. Primary particles are assumed to have a narrow size distribution [106], which leads to the conclusion that a two-moment model for P_1 and P_2 provides sufficient accuracy.

Chapter 3

The Laminar Flamelet Model
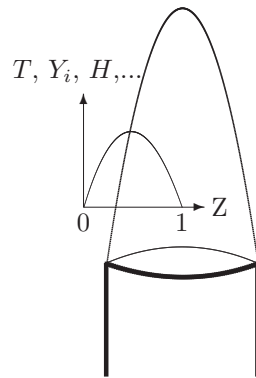
Figure 3.1: Ensemble of flamelets in a diffusion flame

The laminar flamelet model is a tool which makes it possible to couple the information contained in a thorough physical description of the flow with detailed chemical models. The approach is based on dividing the flame into an ensemble of small laminar counterflow diffusion flames (flamelets) in the flow field (Figures 3.1 and 3.2). The conservation equations for the ensemble are trans-
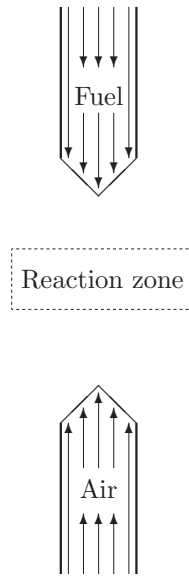
Figure 3.2: Counter-flow diffusion flame

formed into flamelet space: a space defined on the basis of the mixture fraction coordinate which will be explained in Section 3.1.2. The conserved scalars are calculated in mixture fraction space. Figure 3.3 shows the temperature profile in mixture fraction space at a scalar dissipation rate of $\chi = 5.6680 \ [s^{-1}]$ for the fuel n-decane α-methyl naphtalene. Since the flamelet approach is coupled to flow calculations transport properties within the system must be considered. Hence, the scalar dissipation rate, χ, introduces diffusion effects into the chemical calculations. It describes the coupling to the turbulence.

Apart from the general formulation of the flamelet model, referred to as the unsteady flamelet model, a special case of the model, the steady flamelet model where transient effects are neglected, can be formulated. The steady flamelet model was first developed by Moss and co-workers [48].

Peters [77] defined five states for the combustion system, which are relevant for the flamelet:

1. the steady unreacted initial mixture,

2. the unsteady transition after ignition,

3. the quasi- steady burning state,

4. the unsteady transition after quenching,

5. the unsteady transition after re-ignition.

In states 2, 4 and 5, the flamelet is strongly influenced by transient effects. Neither the steady nor the unsteady flamelet model are able to account for these effects. It is possible, to account for some some transient effects in the steady flamelet model. However, for a system without turbulence the flame turns into a laminar flame and the approach is exact. For higher Reynolds numbers, the concept is acceptable for fast chemistry. Soot formation is a slow process. Hence, transient effects are of relevance. The steady flamelet model may be used to calculate source terms for soot formation. The soot volume fraction can be determined in the flow calculations. Another transient effect is the radiative heat loss, which can be included in the model through the introduction of scaling terms.

3.1 The Physical Model

The general mathematical model, including transport properties and the definition of the mixture fraction and scalar dissipation rate will be given in this section, followed by two approaches used in flamelet modelling the unsteady flamelet model, and the steady flamelet model.

3.1.1 Transport Properties

The transport properties were calculated following the formulation for one-dimensional diffusion by Hirschfelder and Curtiss [136].

$$v_{D,i} = -\frac{D_i}{X_i}\frac{\partial X_i}{\partial x} \tag{3.1}$$

The diffusion, D_i, is defined as:

$$D_i = \frac{1 - Y_i}{\sum\limits_{j=1, j \neq i}^{n_s} \frac{X_j}{D_{i,j}}} \tag{3.2}$$

where $D_{i,j}$ is the binary diffusion coefficient.

Thermodiffusion, or diffusion due to thermophoresis, is a relevant transport phenomenon, which affects molecules and particles of all shapes and sizes. The thermophoretic diffusion (α_T, D) of aggregates has been shown to be independent of size and orientation [137] and has been shown to be 8% of the thermophoretic diffusivity of a primary soot particle. Thermodiffusion of soot particles and agglomerates is of special interest for experimentalists, since the effect is used to extract soot particles from flames using a cold plate. However, the effect presents difficulties for theoreticians. To avoid complicated computations with unreliable results in this work, thermal diffusion was considered for light species only, as recommended by Paul and Warnatz [138]. The modelling problem lies in the definition of the relevant thermal diffusion factor, α_T, and the lack of experimental information on this factor. It should be mentioned that Rosner et al. [139] suggested a formulation of the factor. The thermodiffusion for species with small molar mass is given by [108]:

$$v_{T,i} = -\frac{D_i t_i^T}{X_i} \frac{1}{T} \frac{\partial T}{\partial x} \tag{3.3}$$

where t_i^T is the thermodiffusion coefficient. The condition $\sum_{i=1}^{n_s} Y_i v_i = 0$ will be fulfilled by introducing a correction for the mass $v_{c,i}$. The complete definition of the diffusion is then given by:

$$v_i = v_{d,i} + v_{T,i} + v_{C,i} \tag{3.4}$$

The Lewis number (Le) is a measure of transport:

$$Le_i = \frac{\lambda}{\rho D_i c_p} \tag{3.5}$$

where λ is the thermal diffusivity, ρ the density and c_p the heat capacity. The diffusion for species i can be expressed as a function of the Lewis number:

$$D_i = \frac{\lambda}{\rho Le_i c_p} \tag{3.6}$$

Different diffusion model are studied in Chapter 4. Depending on the model the Lewis number is assumed to be either unity, constant in space but species dependent or varying in space and being species dependent. Assuming a Lewis number of unity implies that all chemical species diffuse in the same way; we can define the diffusibility using Fick's law.

$$\rho V_{i\alpha} Y_i = -\rho D_Z \frac{\partial Y_i}{\partial x_\alpha} \tag{3.7}$$

The effect of this term on soot formation will be explained below.
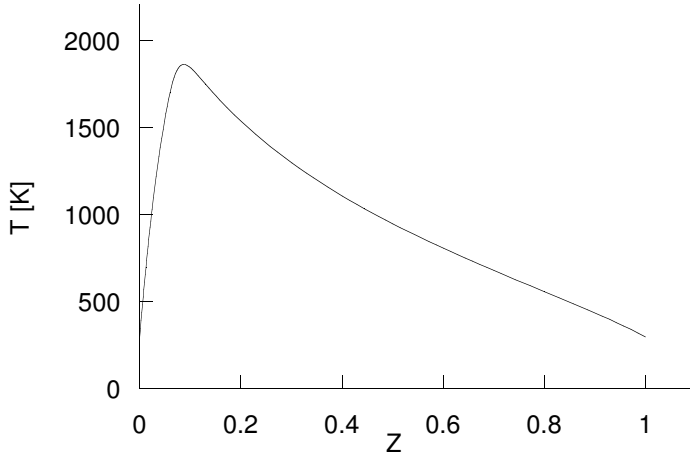
Figure 3.3: Temperature as a function of mixture fraction. The mixture fraction Z is defined in the interval $[0, 1]$. $Z = 0$ in regions where only oxidizer is present and $Z = 1$ in regions where only fuel is present.

3.1.2   Definition of the Mixture Fraction Coordinate

Combustion processes occur when a mixture of a fuel and an oxidizer stream ignite. The mixture fraction Z can be considered as a space coordinate, convenient for the description of combustion processes. Z describes the mixing state of a combustion system, and was first introduced by Bilger [68]. The mixture fraction, Z, is defined in the interval $Z \in [0, 1]$. The boundary of the mixture fraction is given by $Z = 1$ in the pure fuel side and $Z = 0$ in the pure oxidizer side (Figure 3.3). According to Bilger [68] the local value of any conserved scalar, β, can be used to define the mixture fraction:

$$Z = \frac{\beta - \beta_O}{\beta_F - \beta_O} \tag{3.8}$$

where β_F and β_O are the values of the conserved scalar in the fuel stream and in the oxidizer stream, respectively. A conserved scalar preferably used for combustion purposes is the mass fraction Z_i of the elements, which is a conserved scalar during this process. The mass fraction Z_j of element j is

related to the mass fraction Y_i of species i by:

$$Z_j = \frac{m_j}{m} = \sum_{i=1}^{n} \frac{a_{ij}\omega_j}{\omega_i} Y_i \tag{3.9}$$

This conserved scalar variable element j may be defined on the basis of the mass fractions and the molar masses ω_j, ω_i, and a_{ij} is the number of atoms of element j. The application of the operator for the transport equation:

$$L = \rho \frac{\partial}{\partial t} + \rho v_\alpha \frac{\partial}{\partial x_\alpha} + \frac{\partial}{\partial x_\alpha} \left(\rho D_Z \frac{\partial}{\partial x_\alpha} \right) \tag{3.10}$$

results in the mixture fraction transport equation:

$$L(Z_j) = \frac{\partial}{\partial x_\alpha} \left(\sum_{i=1}^{n} \frac{a_{ij}\omega_j}{\omega_i} \left(\rho D_Z \frac{\partial Y_i}{\partial x_\alpha} + \rho V_{i\alpha} Y_i \right) \right) + \sum_{i=1}^{n} \frac{a_{ij}\omega_j}{\omega_i} \dot{m}_i \tag{3.11}$$

Definition of the mixture fraction for unity Lewis number

Assuming a Lewis number of unity, Equation 3.11 can be reduced to:

$$L(Z_j) = \sum_{i=1}^{n} \frac{a_{ij}\omega_j}{\omega_i} \dot{m}_i = \omega_j \sum_{i=1}^{n} \frac{a_{ij}}{\omega_i} \dot{m}_i = -\nu_j \omega_j \omega \tag{3.12}$$

In order to define a relevant conserved scalar for the process, we will consider the chemical species of greatest importance for the combustion process:

$$\nu_C C + \nu_H H + \nu_O O \rightarrow P \tag{3.13}$$
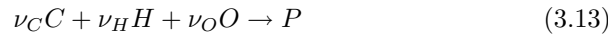
where ν_j is the number of atoms j contained in the enduct. Consequently, we define the conserved scalar variable β to be:

$$\beta \equiv \frac{Z_C}{\nu_C \omega_C} + \frac{Z_H}{\nu_H \omega_H} - 2 \frac{Z_O}{\nu_O \omega_O} \tag{3.14}$$

Applying β in Equation 3.8 allows the mixture fraction coordinate for unity Lewis number to be defined:

$$Z = \frac{\frac{Z_C}{\nu_C \omega_C} + \frac{Z_H}{\nu_H \omega_H} - 2 \frac{Z_{O,ox} - Z_O}{\nu_O \omega_O}}{\frac{Z_{C,fuel}}{\nu_C \omega_C} + \frac{Z_{H,fuel}}{\nu_H \omega_H} - 2 \frac{Z_{O,ox}}{\nu_O \omega_O}} \tag{3.15}$$

For $Le = 1$ the transport equation for the mixture fraction is given by:

$$L(Z) = 0 \tag{3.16}$$

which gives:

$$\rho \frac{\partial Z}{\partial t} + \rho v_\alpha \frac{\partial Z}{\partial x_\alpha} - \frac{\partial}{\partial x_\alpha} \left(\rho D \frac{\partial Z}{\partial x_\alpha} \right) = 0 \tag{3.17}$$

The point of stoichiometry is given by:

$$Z_{st} = \frac{2\nu_O \omega_O}{\frac{Z_{C,fuel}}{\nu_C \omega_C} + \frac{Z_{H,fuel}}{\nu_H \omega_H} - 2\frac{Z_{O,ox}}{\nu_O \omega_O}} \tag{3.18}$$

Definition of the mixture fraction for preferential diffusion

Assuming preferential diffusion means that all species diffuse in a different way, which implies the assumption of a non-unity Lewis number, $Le \neq 1$. The mixture fraction transport equation for this condition is given by:

$$\rho \frac{\partial Z}{\partial t} + \rho v_\alpha \frac{\partial}{\partial Z} \left(\rho D \frac{\partial Z}{\partial x_\alpha} \right) = 0 \tag{3.19}$$

Equation 3.18 does not describe the stoichiometric development of the mixture fraction in the case of preferential diffusion [140]. However, since the point of stoichiometry is used as a reference point, we will make use of Equation 3.15. The maximum temperature is reached at the point of stoichiometry and this fact can be used to identify Z_{st}.

3.2   The Unsteady Flamelet Model

The unsteady flamelet concept was first introduced by Pitsch et al. [78]. It is the most general formulation of the flamelet model and it accounts for transient processes such as ignition and extinction.

3.2.1   Governing Equations

The time-dependent Navier-Stokes equations describe the combustion system. The energy conservation equation in terms of the enthalpy, h, in the low-Mach-number approximation is:

$$\rho \frac{\partial h}{\partial t} + \rho v_\alpha \frac{\partial h}{\partial x_\alpha} - \frac{\partial}{\partial x_\alpha} \left(\frac{\lambda}{c_p} \frac{\partial h}{\partial x_\alpha} \right) \qquad + \tag{3.20}$$

$$\frac{\partial}{\partial x_\alpha} \sum_{i=1}^{n} \left(\frac{\lambda}{c_p} h_i \frac{\partial Y_i}{\partial x_\alpha} - \rho D_i \frac{Y_i}{X_i} (h_k - h) \frac{\partial X_i}{\partial x_\alpha} \right)$$

$$= \frac{\partial p}{\partial t} + \frac{\partial q_r}{\partial t}$$

The conservation of species mass fractions, Y_i, can be written as:

$$\rho \frac{\partial Y_i}{\partial t} + \rho v_\alpha \frac{\partial Y_i}{\partial x_\alpha} + \frac{\partial}{\partial x_\alpha} \left(\rho Y_i V_{i\alpha} \right) = \dot{\omega}_i \tag{3.21}$$

where the diffusion velocity, $V_{i\alpha}$, is given by:

$$V_{i\alpha} = V_{i\alpha}^D + V_{i\alpha}^C \tag{3.22}$$

This term is defined by the sum of diffusion, $V_{i\alpha}^D$, and the correction term, $V_{i\alpha}^C$, which compensates for the loss of mass

$$V_{i\alpha}^D = -\frac{D_i}{X_i} \frac{\partial X_i}{\partial x_\alpha} \tag{3.23}$$

$$V_{i\alpha}^C = \sum_{k=1}^{n} \frac{Y_k}{X_k} D_k \frac{\partial X_k}{\partial x_\alpha} \tag{3.24}$$

The Curtiss - Hirschfelder [136] approximation and a correction term for conservation of mass are used to model neglecting thermodiffusion. Where α denotes the space coordinates, v, the velocities and $V_{i\alpha}$ the diffusion velocities. $\dot{\omega}_i$ are the chemical source terms of species i, n, the number of chemical species, λ the heat conductivity, c_p the heat capacities and p the pressure. S_r is the heat loss due to radiation and X_i and Y_i are mole and mass fraction of species i respectively. The pressure-dependent term can be neglected in open diffusion flames. The conservation equation of the moments in space is defined as:

$$\rho \frac{\partial}{\partial t} \frac{M_r}{\rho} + \rho v \frac{\partial}{\partial x} \frac{M_r}{\rho} = \frac{\partial}{\partial x} \left[\rho D_i \frac{\partial}{\partial x} \left(\frac{M_{r-2/3}}{\rho} \right) \right] + \dot{M}_r \tag{3.25}$$

The equations can be further simplified by neglecting the Dufour (energy transport due to thermal diffusion) and the Soret effects (mass transport due to thermal diffusion) and by assuming equal diffusiveness for all species and unity Lewis numbers:

$$\rho Y_i V_{i\alpha} = -\rho D \frac{\partial Y_i}{\partial x_\alpha} \tag{3.26}$$

$$Le = \frac{\lambda}{\rho D c_p} \equiv 1 \tag{3.27}$$
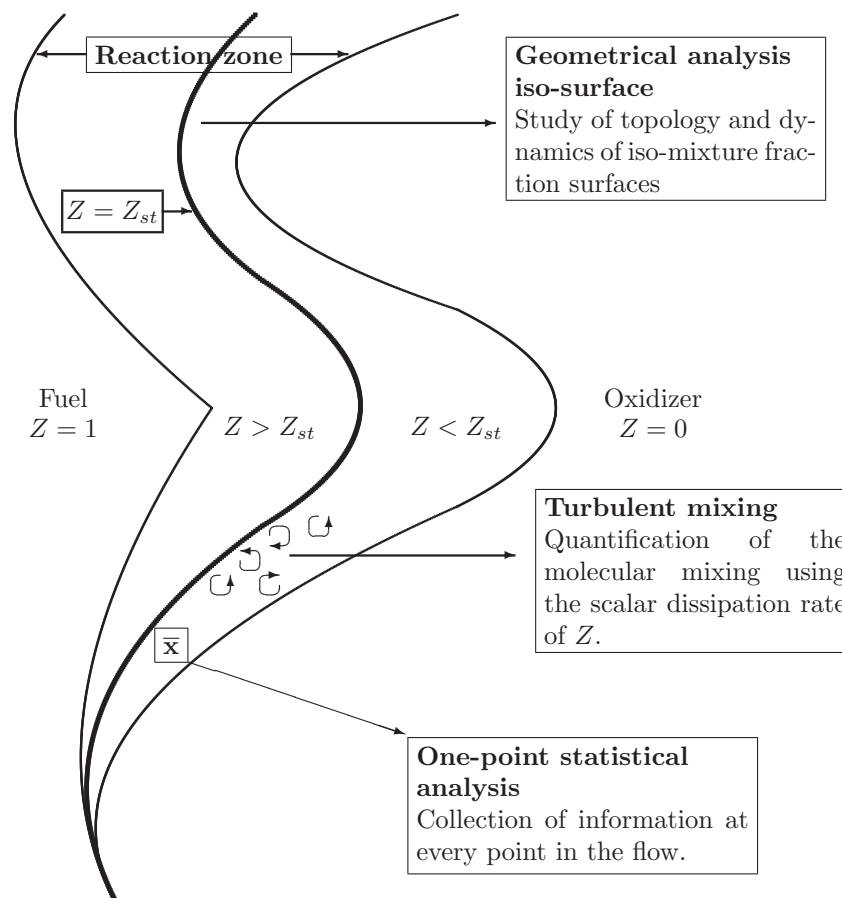
Figure 3.4: Non-premixed turbulent flame, after [141], visualising the reaction zone where flamelet calculations are performed; the stoichiometric iso-mixture fraction surface; eddies, a consequence of turbulence mixing.

3.2.2 Transformation into Mixture Fraction Coordinates

Navier-Stokes equations can be transformed into the coordinate-free system [77], the first dimension of flamelet space. The chemical reactions in a flame take place mainly in a thin zone around the stoichiometric mixture fraction iso-surface (Figure 3.4). A new coordinate system is defined where x_1 is replaced by the coordinate Z, which is normal to the surface of the stoichiometric mixture. Defining $Z_2 = x_2$, $Z_3 = x_3$ and $\tau = t$, the following transformation rules are obtained.

$$\frac{\partial}{\partial t} = \frac{\partial}{\partial \tau} + \frac{\partial Z}{\partial t}\frac{\partial}{\partial Z} \tag{3.28}$$

$$\frac{\partial}{\partial x_1} = \frac{\partial Z}{\partial x_1}\frac{\partial}{\partial Z} \tag{3.29}$$

$$\frac{\partial}{\partial x_k} = \frac{\partial}{\partial Z_k} + \frac{\partial Z}{\partial x_k}\frac{\partial}{\partial Z}, \quad k = 2,3 \tag{3.30}$$

3.2.3 Governing Equations in Flamelet Space

The energy conservation equation is:

$$\rho c_p \frac{\partial T}{\partial \tau} + \frac{\rho \chi}{2}\left[\frac{\partial}{\partial Z}\left(c_p \frac{\partial T}{\partial Z}\right) + H\right] = \sum_{i=1}^{N} h_i \omega_i + S \tag{3.31}$$

where S is the radiative heat loss.

$$H = \sum_{k=1}^{N} (c_{p,k} - c_p)\frac{\partial T}{\partial Z}\frac{Y_k}{Le_k X_k}\frac{\partial X_k}{\partial Z} \tag{3.32}$$

The species conservation equation is:

$$\rho \frac{\partial Y_i}{\partial \tau} - \frac{\rho \chi}{2}\frac{\partial F_i}{\partial Z} - \frac{G_i}{4} = -\frac{\partial \omega_i}{\partial \tau} \tag{3.33}$$

where:

$$F_i = \frac{Y_i}{Le_i X_i}\frac{\partial X_i}{\partial Z} - Y_i \sum_{k=1}^{N} \frac{Y_k}{Le_k X_k}\frac{\partial X_k}{\partial Z} \tag{3.34}$$

$$G_i = \left(F_i - \frac{\partial Y_i}{\partial Z}\right)\left(\frac{\partial \rho \chi}{\partial Z} + \frac{\chi}{D}\frac{\partial \rho D}{\partial Z}\right) \tag{3.35}$$

The conservation equation of the statistical soot moments is:

$$\rho \frac{\partial}{\partial \tau} \left(\frac{M_r}{\rho} \right) - \frac{\rho \chi}{2} \frac{\partial}{\partial Z} F_S - \frac{G_S}{4} = -\frac{\partial}{\partial \tau} M_r \qquad (3.36)$$

where:

$$G_S = \left[F_S - \frac{\partial}{\partial Z} \left(\frac{M_r}{\rho} \right) \right] \left[\frac{\partial}{\partial Z} (\rho \chi) + \frac{\chi}{D} \frac{\partial}{\partial Z} (\rho D) \right] \qquad (3.37)$$

and

$$F_S = \frac{D_{p,i}}{D} \frac{\partial}{\partial Z} \left(\frac{M_r}{\rho} \right) \qquad (3.38)$$

3.2.4   Radiative Heat Loss

The radiative heat loss parameter S in Equation 3.31 is computed using the Stefan-Boltzmann law. Radiative heat loss plays an important role in soot formation. It also takes place on a long time scale [78] and is therefore a transient effect, which is preferably modelled using the unsteady flamelet approach. It is defined as:

$$\begin{aligned} S &= \alpha_p S_r & (3.39) \\ &= \alpha_p \sigma_s T^4 \end{aligned}$$

where:

$$\alpha_p = \alpha_{p,soot} \ fv + \alpha_{p,CO_2} \ p_{CO_2} + \alpha_{p,H_2O} \ p_{H_2O} \qquad (3.40)$$

there, p_{CO_2} and p_{H_2O} are the partial pressure of CO_2 and H_2O. The coefficients for the radiative heat loss of these species: v_{CO_2} and α_{H_2O}, were taken from [108]:

$$\alpha_{p,CO_2} = 46.241 \cdot \exp -8.888 \cdot 10^{-4} T \qquad (3.41)$$

$$\alpha_{p,H_2O} = 22.6 \cdot \exp -1.546 \cdot 10^{-3} T \qquad (3.42)$$

$$\alpha_{p,soot} = -3.75 \cdot 10^5 + 1.735 \cdot 10^3 T \qquad (3.43)$$

3.2.5   Definition of the Scalar Dissipation Rate

The scalar dissipation rate, χ, is a variable of great relevance for combustion models. There are many physical interpretations of this characteristic inverse diffusion time imposed by the mixing field. The scalar dissipation rate introduces the mixing rate into the chemical calculations. It can be regarded as the

rate at which scalar fluctuations are destroyed. The scalar dissipation rate is a function of the diffusivity, D, and the mixture fraction Z:

$$\chi = D\nabla Z \cdot \nabla Z \qquad (3.44)$$

Su et al. [27] measured χ by recording data of the mixture fraction from PLIF experiments. The scalar dissipation rate was defined to be the loss term in the temporal evolution of the mixture fraction, $\frac{1}{2}Z^2$:

$$\left(\frac{\partial}{\partial t} + \mathbf{u} \cdot \nabla - D\nabla^2\right)\frac{1}{2}Z^2 = -D\nabla Z \cdot \nabla Z \equiv -\chi \qquad (3.45)$$

The influence on the flow field to the chemical system is introduced into the conservation equation by the instantaneous scalar dissipation rate χ. It is relevant for the coupling between the chemical calculations and the flow field as already described in Section 1.3.3.

An understanding of the physical evolution of the scalar dissipation rate can be gained by studying the maximum temperature in mixture fraction space as a function of the inverse scalar dissipation rate (Figure 3.5). The figure shows the transition between the lower and the upper quenching point at temperatures T_2 and T_3. As temperature in a mixture rises from T_0, the point of ignition is reached at T_1. The reaction rate increases rapidly, which results in a sudden rise in temperature up to T_3. The flamelet burns following the upper branch of the S-shaped curve from the ignition point to χ_i at T_3 to the point where the flame is quenched at χ_q at T_2. Starting at ignition, χ_i an increase in scalar dissipation rate leads to a drop in the maximum temperature due to higher diffusive transport of energy and species from the reaction zone. Soot formation is usually quenched earlier and at lower scalar dissipation rates, as the flamelet itself. It should be noted that the scalar dissipation rate is much lower at the point of ignition than at quenching. The formulation of the scalar dissipation rate is dependent on the combustion process. Its value decreases with x^{-4} along the axis, where x is the height above the burner. Since the scalar dissipation rate has considerable influence on the flamelet, we must assume that the flamelet undergoes rapid changes as it moves downstream. The unsteady flamelet is a function of the flamelet time, which is the the time scale in which the flamelet moves upstream. It is related to the height over the nozzle (Figure 3.7).

$$t = \int_0^x \left(u\left(x^{'}\right)\big|_{\left(\widetilde{Z}=Z_{st}\right)}\right)^{-1} dx^{'} \qquad (3.46)$$

where $\widetilde{Z}$ is the Favre average of the mixture fraction, and $u(x^{'})$ is the axial
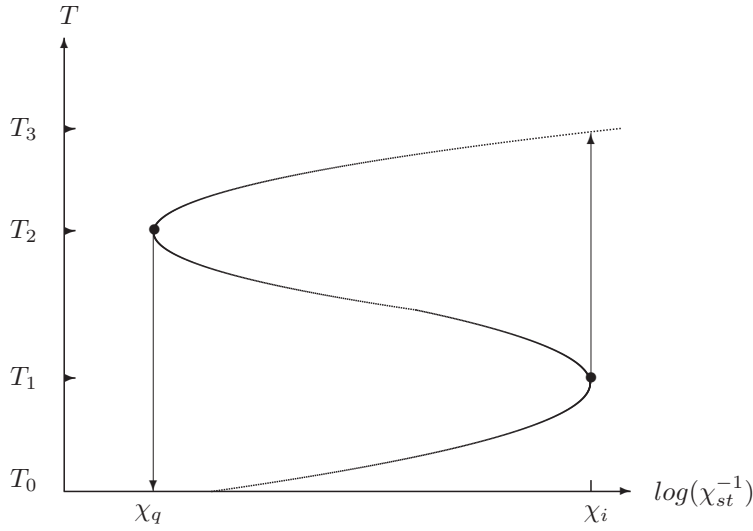
Figure 3.5: Transition of the inverse scalar dissipation rate between the lower and the upper quenching point.

velocity component at along the iso-surface $\widetilde{Z} = Z_{st}$ illustrated in Figure 3.4. The transience of the scalar dissipation rate is taken from the flow field solution as a domain average of the conditional scalar dissipation rate at stoichiometric condition $\langle \widehat{\chi_{st}} \rangle$. It is defined in Equation 3.65. The unsteady flamelet is calculated and time averaged at every grid point in the flow using the distribution of mixture fraction. The transport equation for a one-dimensional laminar mixing layer is given by:

$$\rho \frac{\partial Z}{\partial t} - \frac{\partial}{\partial x} \left(\rho D_i \frac{\partial Z}{\partial x} \right) = 0 \tag{3.47}$$

with the following initial and boundary conditions:

$$
\begin{aligned}
&t = 0 : Z = 1 \text{ for } x < 0 \text{ and } Z = 0 \text{ for } x > 0 \\
&t > 0 : Z = 1 \text{ for } x \longrightarrow -\infty \text{ and } Z = 0 \text{ for } x \longrightarrow \infty
\end{aligned} \tag{3.48}
$$

Choosing a reference point at stoichiometry one obtains an expression of the
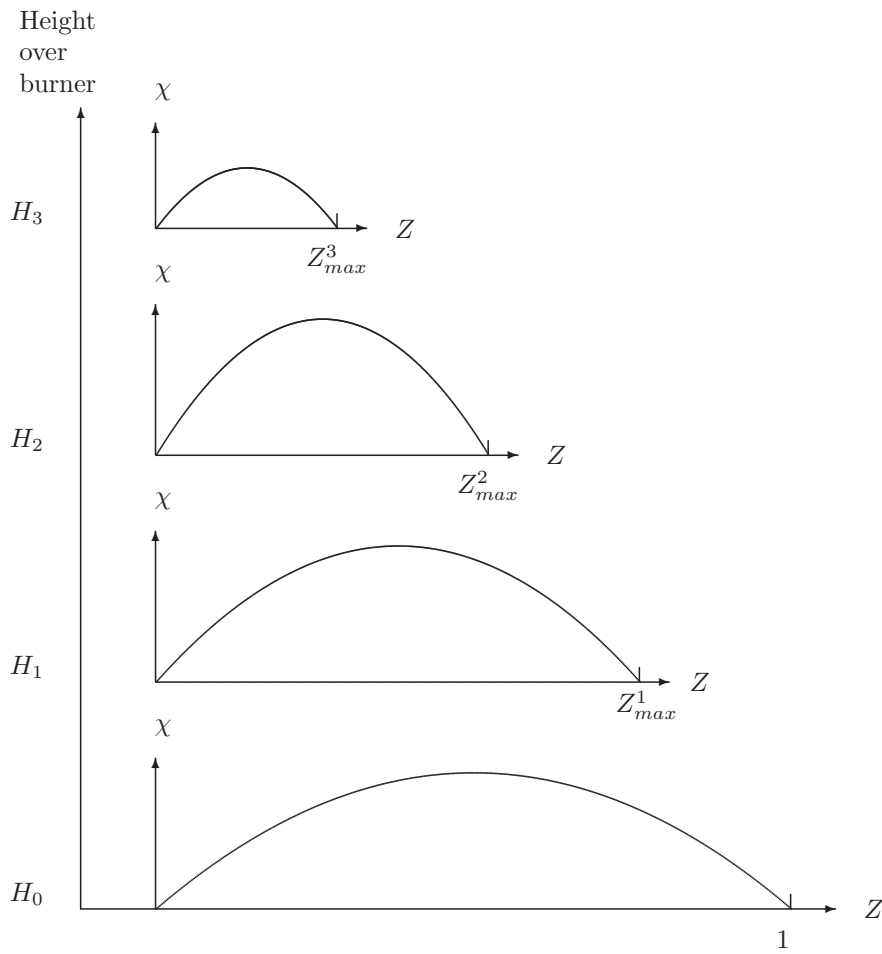
Figure 3.6: Evolution of the scalar dissipation rate in mixture fraction space.
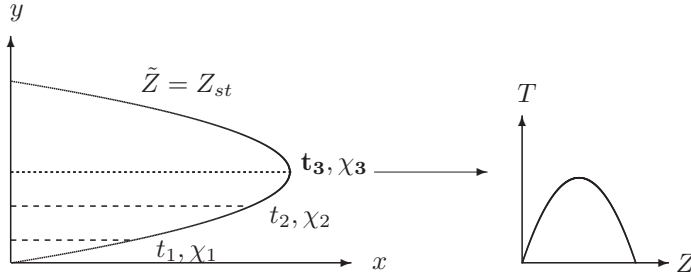
Figure 3.7: The left side shows the iso-surface at $Z_s t$ in the flow, and the temporal evolution of the scalar dissipation rate. The right side shows a schematic temperature profile in flamelet space for a particular scalar dissipation rate, $\chi_3 = \chi(t_3)$.

similarity coordinate η:

$$\eta = \frac{1}{2\sqrt{D_{st}t}} \int_0^x \frac{\rho}{\rho_{st}} dx \qquad (3.49)$$

which can be solved by:

$$Z = \frac{1}{2} Erfc^{-1}(\eta) \qquad (3.50)$$

The resulting scalar dissipation rate can be expressed as a function of time and mixture fraction [77].

$$\chi(Z,t) = \chi_{st} \frac{f(Z)}{f(Z_{st})} \qquad (3.51)$$

It can be read as a function of the complementary inverse of the Gaussian error function of the mixture fraction Z.

$$\chi(Z,t) = \frac{1}{2\pi t} \exp\left(-2Erfc^{-1}(2Z)^2\right) \qquad (3.52)$$

The transient path of the scalar dissipation rate, can be translated into its path in height over the burner. This path is dependent on the chemical properties of the fuel as well as the physical properties of the combustion process.

The time may be considered to be a parameter and related to the known reference value at stoichiometry of the scalar dissipation rate, namely $\chi_{st}(t)$. The scalar dissipation rate can now be expressed as:

$$\chi(Z) = \chi_{st}(t) \exp\left[2\left(\left[Erfc^{-1}(2Z_{st})\right]^2 - \left[Erfc^{-1}(2Z)\right]^2\right)\right] \qquad (3.53)$$

Assuming constant density, the scalar dissipation rate may be defined as [78]:

$$\chi(Z) = \frac{a_{ox}}{\pi} \exp\left(-2Erfc^{-1}(2Z)^2\right) \qquad (3.54)$$

Considering potential flows the strain rate a_{ox} may be defined as $a_{ox} = \frac{\partial u_{ox}}{\partial x}$. The main formulation of the scalar dissipation rate applied in this thesis is given by the eqation:

$$\chi(Z) = \langle\chi_{st}(t)\rangle \exp\left(-2Erfc^{-1}(2Z)^2\right) \qquad (3.55)$$

where $\langle\chi_{st}(t)\rangle$ is taken from the flow code and is derived following the formulation of Pitsch [78] (Equation 3.64).

For the investigations on the laminar diffusion flame, the scalar dissipation rate will be taken from the flow code. Since the broadness of the scalar dissipation rate diminishes with time we substitute $Z = Z/Z_{\max}$ where $Z_{\max}(t)$ is a decaying function of time (Figure 3.6. It was conditioned at $Z_{max}+15\%$ to account for the fact that soot is formed in rather fuel-rich domains. The conditions for non-constant density were given by Kim and Williams [142]:

$$\chi(Z) = \frac{a_{ox}}{\pi} \frac{3\left(\sqrt{\rho_{ox}/\rho} + 1\right)^2}{2\sqrt{\rho_{ox}/\rho} + 1} \exp\left(-2Erfc^{-1}(2Z)^2\right) \qquad (3.56)$$

At χ_{st} and Z_{st} the strain rate is given by:

$$a_{ox} = \chi_{st}\pi \frac{2R_{st}+1}{3\left(R_{st}+1\right)^2} \exp\left(2Erfc^{-1}(2Z_{st})^2\right) \qquad (3.57)$$

$$\chi(Z) = \chi_{st}\frac{2R_{st}+1}{2R+1}\frac{(R+1)^2}{(R_{st}+1)^2} \qquad (3.58)$$

$$\cdot \exp\left(2\left[Erfc^{-1}(2Z_{st})^2 - Erfc^{-1}(2Z)^2\right]\right) \qquad (3.59)$$

where $R = \sqrt{\rho_{ox}/\rho}$ and $R_{st} = \sqrt{\rho_{ox}/\rho_{st}}$. The scalar dissipation rate given by Equation 3.51 depends on Z and χ_{st}. The turbulent mean of the scalar

dissipation rate will now be defined assuming that Z and χ_{st} are statistically independent variables.

$$\chi(Z, t) = \chi_{st}(Z, t) \left(\frac{Z}{Z_{st}}\right)^2 \frac{\ln(Z)}{\ln(Z_{st})} \tag{3.60}$$

$$\tilde{\chi} = \int_{\chi_{st}} \chi'_{st} \tilde{P}(\chi'_{st}) d\chi'_{st} \int_Z f(Z) \tilde{P}(Z) dZ \tag{3.61}$$

$$\tilde{\chi} = \langle \chi_{st} \rangle \int_Z f(Z) \tilde{P}(Z) dZ$$

where:

$$\langle \chi_{st} \rangle = \int_{\chi_{st}} \chi'_{st} \tilde{P}(\chi'_{st}) d\chi'_{st} \tag{3.62}$$

is the mean scalar dissipation rate conditioned at Z_{st}. This formulation of the mean scalar dissipation rate may be linked to the following model of the unconditional mean scalar dissipation rate derived by Pope [143].

$$\tilde{\chi} = \int_0^1 \chi_{st} \frac{f(Z)}{f(Z_{st})} \tilde{P}(Z) dZ = c_\chi \frac{\tilde{\varepsilon}}{\tilde{k}} \widetilde{Z''^2} \tag{3.63}$$

Applying Equations 3.61 and 3.63 gives:

$$\langle \chi_{st} \rangle = \frac{c_\chi \frac{\tilde{\varepsilon}}{\tilde{k}} \widetilde{Z''^2}}{\int_0^1 \frac{f(Z)}{f(Z_{st})} \tilde{P}(Z) dZ} \tag{3.64}$$

The computation is done over each grid cell and averaging over the total domain. The domain-averaged value of the conditional scalar dissipation rate at stoichiometric mixture is weighted with the surface of the stoichiometric mixture per unit volume.

$$\langle \widehat{\chi_{st}} \rangle = \frac{\int_V \langle \chi_{st} \rangle^{3/2} \overline{\rho} \tilde{P}(Z_{st}) dV'}{\int_V \langle \chi_{st} \rangle^{\frac{1}{2}} \overline{\rho} \tilde{P}(Z_{st}) dV'} \tag{3.65}$$

3.2.6   Coupling to the Flow Field

The conditional, time-dependent scalar dissipation rate, $\chi_{st}(t)$, and the mixture fraction at the stoichiometric iso-surface, Z_{st}, are the parameters responsible for introducing the transport and turbulence information into the flamelet calculations. The two profiles are determined in the flow and fed into the flamelet
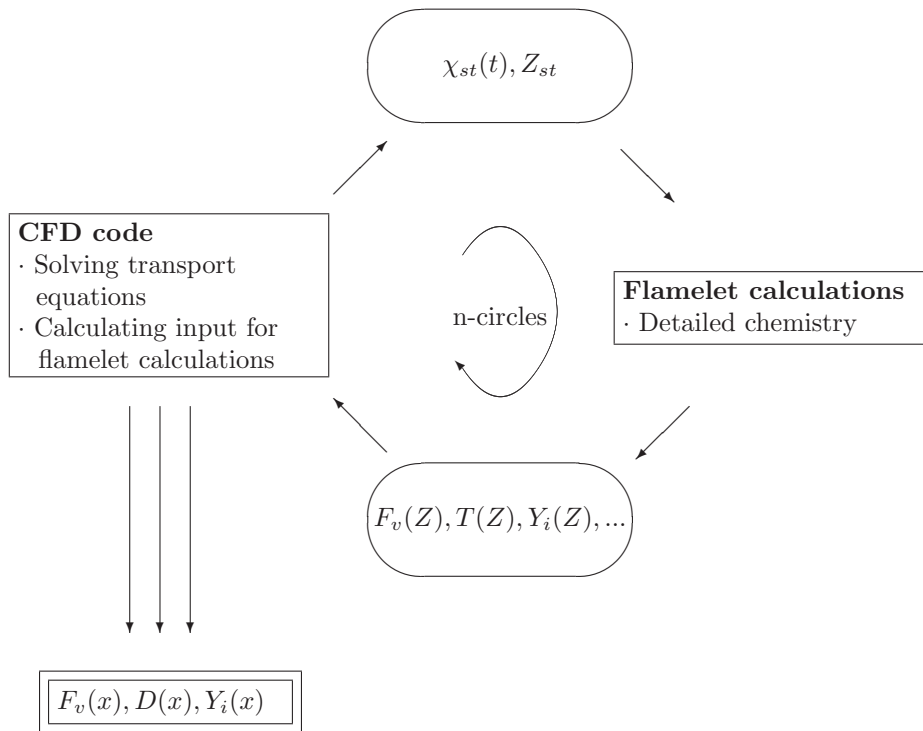
Figure 3.8: Coupling of the unsteady flamelet method to the flow model.

calculations, where soot volume fraction, species concentrations and temperature profiles are calculated in mixture fraction space. The scalars are then transported in the flow field and a new distribution of the interface parameters is determined. After repetition n times, the flow code determines the final distribution in physical space. A schematic description of the method can be seen in Figure 3.8.

3.2.7   The Flow Code

An in-house CFD RANS code developed by Bai [144] was in charge for the flow calculations delivering the values of the time-dependent scalar dissipation

rate, characteristics of the mixture fraction as well as the stoichiometric iso-surface. The diffusion flame was modelled by solving Favre-averaged Navier-Stokes equations with the standard $k - \epsilon$ equation and the Boussinesq gradient-diffusion hypothesis for the Reynold stresses and the scalar fluxes. A general form of the governing equations in Cartesian coordinates is:

$$\frac{\partial \overline{\rho} \tilde{\Psi}}{\partial t} + \frac{\partial \overline{\rho} \tilde{u}_j \tilde{\Psi}}{\partial x_j} = \frac{\partial}{\partial x_j} \left(\frac{\mu_e}{Pr_t} \frac{\partial}{\partial x_j} \right) + \overline{S}_\Psi \tag{3.66}$$

The bar denotes a time- (Reynolds) average and the tilde a mass- (Favre) averaged quantity. Pr_t is the turbulent Prandtl number and $\mu_e = \mu_L + C_\mu \overline{\rho} \frac{k^2}{\epsilon}$ is the turbulent effective viscosity, while μ_L is the laminar viscosity. For the continuity equation we have $\Psi = 1$, and for the energy conservation equation $\Psi = h$. The source term $\overline{S}_\Psi$ in the energy equation is calculated by assuming that the medium is optically thin. The code employs a staggered cylindrical grid system with second-order numerical discretization. Steady-state solutions are obtained with a pseudo-timemarching technique.

The mean flow field consisting of the Favre mean velocity, enthalpy and mean and the stoichiometric mixture fraction, as well as scalar dissipation rate at stoichiometric condition is calculated for every time step. The PDF, $\wp(Z, \chi)$, is determined. This is done using the the flow information on the mixture fraction $\tilde{Z}, \widetilde{Z"}^2$ and scalar dissipation rate μ_χ, σ_χ as well as the flamelet relation $\rho = \rho(Z, \chi)$.

With $\wp(Z, \chi)$, the values of $\overline{T}, \overline{f}$ and $\overline{\rho}$ can be found and the calculation is repeated for the next time step. The values of Z_{st} and χ_{st} are determined as an input for the unsteady flamelet calculation.

3.3 The Steady Flamelet Model

Assuming preferential diffusion, the Lewis number varies for all species as a function of the mixture fraction. The chemical system can be described by the following conservation equations. The species conservation equation:

$$\frac{\rho \chi}{2} \frac{\partial F_i}{\partial Z} + \frac{G_i}{4} = \omega_i \tag{3.67}$$

where:

$$F_i = \frac{Y_i}{Le_i X_i} \frac{\partial X_i}{\partial Z} - Y_i \sum_{k=1}^{N} \frac{Y_k}{Le_k X_k} \frac{\partial X_k}{\partial Z} \tag{3.68}$$

and:

$$G_i = \left(F_i - \frac{\partial Y_i}{\partial Z} \right) \left(\frac{\partial \rho \chi}{\partial Z} + \frac{\chi}{D} \frac{\partial \rho D}{\partial Z} \right) \tag{3.69}$$

The momentum conservation equation:

$$\frac{\rho\chi}{2}\frac{\partial F_S}{\partial Z} + \frac{G_S}{4} = M_r \tag{3.70}$$

where:

$$F_S = \frac{D_{p,i}}{D}\frac{\partial\left(M_r/\rho\right)}{\partial Z} \tag{3.71}$$

and:

$$G_S = \left(F_S - \frac{\partial\left(M_r/\rho\right)}{\partial Z}\right)\left(\frac{\partial\rho\chi}{\partial Z} + \frac{\chi}{D}\frac{\partial\rho D}{\partial Z}\right) \tag{3.72}$$

The energy conservation equation:

$$-\frac{\rho\chi}{2}\left[\frac{\partial}{\partial Z}\left(c_p\frac{\partial T}{\partial Z}\right) + H\right] = -\sum_{i=1}^{N}h_i\omega_i - q \tag{3.73}$$

where:

$$H = \sum_{k=1}^{N}\left(c_{p,k} - c_p\right)\frac{\partial T}{\partial Z}\frac{Y_k}{Le_k X_k}\frac{\partial X_k}{\partial Z} \tag{3.74}$$

Assuming the Lewis number to be constant in mixture fraction space, the chemical system can be described as follows. The species conservation equation:

$$\frac{\rho\chi}{2}\frac{\partial F_i}{\partial Z} + \frac{G_i}{4} = \omega_i \tag{3.75}$$

where:

$$F_i = \frac{Y_i}{Le_i X_i}\frac{\partial X_i}{\partial Z} - Y_i \tag{3.76}$$

and:

$$G_i = \left(F_i - \frac{\partial Y_i}{\partial Z}\right)\left(\frac{\partial\rho\chi}{\partial Z} + \frac{\chi}{D}\frac{\partial\rho D}{\partial Z}\right) \tag{3.77}$$

The momentum conservation equation:

$$\frac{\rho\chi}{2}\frac{\partial F_S}{\partial Z} + \frac{G_S}{4} = \frac{\partial M_r}{\partial\tau} \tag{3.78}$$

where:

$$F_S = \frac{D_{p,i}}{D}\frac{\partial\left(M_r/\rho\right)}{\partial Z} \tag{3.79}$$

and:

$$G_S = \left(F_S - \frac{\partial\left(M_r/\rho\right)}{\partial Z}\right)\left(\frac{\partial\rho\chi}{\partial Z} + \frac{\chi}{D}\frac{\partial\rho D}{\partial Z}\right) \tag{3.80}$$

The energy conservation equation:

$$-\frac{\rho\chi}{2}\left[\frac{\partial}{\partial Z}\left(c_p\frac{\partial T}{\partial Z}\right) + H\right] = -\sum_{i=1}^{N} h_i\omega_i - q \tag{3.81}$$

where:

$$H = \sum_{k=1}^{N}(c_{p,k} - c_p)\frac{\partial T}{\partial Z}\frac{Y_k}{Le_k X_k}\frac{\partial X_k}{\partial Z} \tag{3.82}$$

The unity Lewis number assumption results in the following definition of the momentum conservation equation:

$$F_i = \frac{\partial Y_i}{\partial Z} \tag{3.83}$$

so that the term for G_i vanishes.

$$G_i = 0 \tag{3.84}$$

This leads to a change in the species conservation equation:

$$-\frac{\rho\chi}{2}\frac{\partial F_i}{\partial Z} = -\frac{\partial\omega_i}{\partial\tau} \tag{3.85}$$

The momentum conservation equations:

$$\frac{\rho\chi}{2}\frac{\partial F_S}{\partial Z} + \frac{G_S}{4} = M_r \tag{3.86}$$

where:

$$F_S = \frac{D_{p,i}}{D}\frac{\partial\left(M_r/\rho\right)}{\partial Z} \tag{3.87}$$

and:

$$G_S = \left(F_S - \frac{\partial\left(M_r/\rho\right)}{\partial Z}\right)\left(\frac{\partial\rho\chi}{\partial Z} + \frac{\chi}{D}\frac{\partial\rho D}{\partial Z}\right) \tag{3.88}$$

The energy conservation equations:

$$-\frac{\rho\chi}{2}\left[\frac{\partial}{\partial Z}\left(c_p\frac{\partial T}{\partial Z}\right) + H\right] = -\sum_{i=1}^{N} h_i\omega_i - q \tag{3.89}$$

where:

$$H = \sum_{k=1}^{N}(c_{p,k} - c_p)\frac{\partial T}{\partial Z}\frac{Y_k}{Le_k X_k}\frac{\partial X_k}{\partial Z} \tag{3.90}$$

Here q is the radiative heat loss term, which is computed using the Stefan-Boltzmann law and:

$$q = \alpha_p q_r$$
$$= \alpha_p \sigma_s T^4 \tag{3.91}$$

where:

$$\alpha_p = \vec{\alpha} \cdot \vec{p}_{(soot,CO2,H_2O)} = \begin{pmatrix} \alpha_{soot} \\ \alpha_{CO_2} \\ \alpha_{H_2O} \end{pmatrix} \cdot \begin{pmatrix} f_V \\ p_{CO_2} \\ p_{H_2O} \end{pmatrix}$$

Since the soot volume fraction is unknown at this stage, the heat radiation of the soot cannot be determined. Instead, the influence of the soot radiation is accounted for by scaling an external radiation factor α. The value of α is varied, and a library considering different values of radiation are produced. The flamelet library is coupled to the flow field in terms of the Favre mean of the enthalpy. The enthalpy, h, has been calculated using the flow code from Bai [144], where the energy equation is solved.

$$\frac{\partial \overline{\rho} \tilde{h}}{\partial t} + \frac{\partial \overline{\rho} \tilde{u} \tilde{h}}{\partial x_j} = \frac{\partial}{\partial x_j} \left(\frac{\mu_e}{Pr_t} \frac{\partial \tilde{h}}{\partial x_j} \right) + \overline{S}_h \tag{3.92}$$

At each point in the flow field the corresponding field in the library (and radiation factor) is found via the mean enthalpy (comparable to the Moss approach [50]). In this way the local value of α is determined. The source term, $\overline{S}_h$, in the energy equation is calculated by assuming that the medium is optically thin. Soot increases the radiation heat loss, which causes a lower flame temperature thereby affecting the flow field.

This approach enables us to account for the radiative heat loss which has been studied since the early 1970 [145]. This takes place on a long time scale [78], and is therefore a transient effect, which is better accounted for by the unsteady flamelet approach.

3.3.1   Definition of the Scalar Dissipation Rate

In contrast to the formulation of the scalar dissipation ate presented in Section 3.2.5, it is no longer a function of time and does not contribute to the interaction between flow and chemistry calculations. However, it still introduces the turbulent mixing into the chemical calculations of the of the model. It ranges between the ignition and the quenching limit as already discussed in Section 3.2.5 and presented in Figure 3.5.

3.3.2 Coupling to the Flow Field

The interface of chemistry flamelet- and the flow calculations consists of four terms:

1. the conditional, time-dependent scalar dissipation rate $\chi_{st}(t)$;

2. the mixture fraction Z_{st} at the stoichiometric iso-surface;

3. and the enthalpy and the radiative heat loss.

Figure 3.9 shows the coupling between the flamelet calculations and the flow. The statistical distributions of χ and Z are determined in the flow and used to identify soot source terms for volume fraction, species concentrations and temperature profiles precalculated in flamelet space. They are assumed to be statistically independent so that the Favre-averaged joint probability density function for Z and χ can be treated separately as:

$$\tilde{P}(Z, \chi) = \tilde{P}(Z)\tilde{P}(\chi) \tag{3.93}$$

Under the assumption that the scalar dissipation is log-normal distributed, the PDF can be defined as:

$$\tilde{P}(\chi) = \frac{1}{\chi \sigma \sqrt{2\pi}} \exp\left\{ -\frac{1}{2\sigma^2}(\ln \chi - \mu)^2 \right\} \tag{3.94}$$

where the mean and the variance of χ are given by:

$$\mu_\chi = \ln \widetilde{\chi} - \sigma_\chi^2/2, \quad \widetilde{\chi} = c_\chi \widetilde{Z''^2} \frac{\epsilon}{k} \tag{3.95}$$

$$\sigma_\chi^2 = 0.5\ln(Re_t^{1/2}), \quad Re_t = \frac{\rho k^2}{\mu_L \epsilon}, \tag{3.96}$$

where $c_\chi \approx 2$. The PDF for the mixture fraction is based on the assumption that the coordinate is distributed according to a beta function. In some cases a clipped Gaussian distribution is assumed. Hence, the PDF is defined as:

$$P(Z) = Z^{(\alpha-1)}(1-Z)^{(\beta-1)} \frac{\Gamma(\alpha + \beta)}{\Gamma(\alpha)\Gamma(\alpha)} \tag{3.97}$$

where:

$$\alpha = \tilde{Z}\left(\frac{\tilde{Z}(1-\tilde{Z})}{\widetilde{Z''^2}} - 1 \right) \tag{3.98}$$

$$\beta = (1 - \tilde{Z})\left(\frac{\tilde{Z}(1-\tilde{Z})}{\widetilde{Z''^2}} - 1 \right) \tag{3.99}$$

The mean, $\tilde{Z}$, and the variance, $\widetilde{Z''^2}$, of the mixture fraction are determined by the solution of their transport equations in the turbulent flow field:

$$\bar{\rho}\frac{\partial \tilde{Z}}{\partial t} + \bar{\rho}\bar{v}\frac{\partial \tilde{Z}}{\partial x} = \frac{\partial}{\partial x}\left(\frac{\nu_\tau}{Sc_{\tilde{Z}}}\frac{\partial \tilde{Z}}{\partial x}\right) \tag{3.100}$$

$$\bar{\rho}\frac{\partial \widetilde{Z''^2}}{\partial t} + \bar{\rho}\bar{v}\frac{\partial \widetilde{Z''^2}}{\partial x} = \frac{\partial}{\partial x}\left(\bar{\rho}D_t\frac{\partial \widetilde{Z''^2}}{\partial x}\right) + 2\frac{\nu_\tau}{Sc_{\widetilde{Z''^2}}}\left(\frac{\partial \tilde{Z}}{\partial x}\right)^2 - \bar{\rho}\tilde{\chi} \tag{3.101}$$

where the Schmidt number is assumed to be constant ($Sc = 0.7$).

By integrating the instantaneous values and the assumed probability density functions of scalar dissipation rate and mixture fraction, the Favre mean for the species mass fractions reads:

$$\tilde{Y}_i = \int_0^\infty \int_0^1 Y_i(Z,\chi)P(Z,\chi)dZd\chi \tag{3.102}$$

The soot volume fraction is determined by its source terms in the flamelet code. The source terms of surface growth, oxidation and fragmentation are functions of the soot volume fraction. Hence, they must be determined in the flow field. A delta-like distribution is assumed, since only the mean of the soot volume fraction is known in the flow field. This rough assumption was also made in models presented by Moss and co-workers and Leung et al. [48, 146] for the statistical distribution of the soot volume fraction and the number density. However, the soot volume fraction is obtained in the flow code by solving the transport equation for the mean soot mass fraction, $\widetilde{Y}_s$:

$$\frac{\partial \bar{\rho}\widetilde{Y}_s}{\partial t} + \frac{\partial \bar{\rho}\tilde{u}_j\widetilde{Y}_s}{\partial x_j} = \frac{\partial}{\partial x_j}\left(\frac{\mu_e}{Pr}\frac{\partial \widetilde{Y}_s}{\partial x_j}\right) + \rho_s\frac{d\bar{f}_v}{dt}, \tag{3.103}$$

where:

$$Y_s = \frac{f_v\rho_s}{\rho} \tag{3.104}$$

The turbulent Prandtl number, Pr, for soot is assumed to be 1.4. In order to account for black body-radiation from soot particles radiation must be included in the coupling. Radiative heat transfer from the soot particles and the gas phase species. CO_2 and H_2O affects the flame temperature and thus the flamelets. The mean enthalpy is calculated in the flow field in order to include radiation heat losses.

As well as computing the mixture fraction, Z, at every point in physical space, the flow code also computes its mean and variance, the scalar dissipation rate, χ, and mean and variance, and mean enthalpies and also identifies the
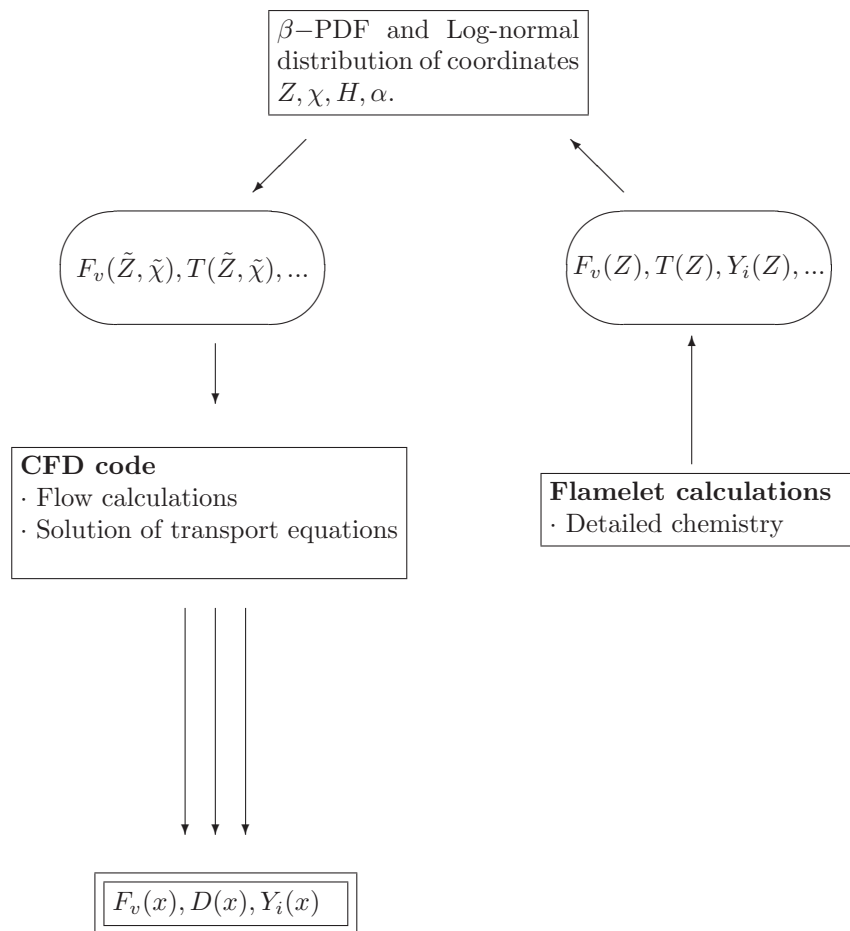
Figure 3.9: Coupling of the steady flamelet method to the flow model.

corresponding library for the different heat loss parameters, α. The temperature decreases with increasing radiation which leads to a change of the rates of soot formation and oxidation.

3.3.3   The Flow Code

The flow calculations and the solving of the transport equations for the soot and mixture fraction were done in the CFD code by Bai [144] described in Section 3.2. Soot increases the radiative heat loss and thus affects the flow field. The absorption coefficients are computed in a similar way to that used previously in fires by de Ris [147]. The code starts with initial estimates of the dependent variables. The mean flow field consisting of $\tilde{u}_j, \tilde{h}, \tilde{Z}, \widetilde{Z''}^2, \mu_\chi$ and σ_χ, is calculated. The PDF, $\wp(Z, \chi)$, is determined for different heat loss parameters α. This is done using the the flow information on the mixture fraction $\tilde{Z}, \widetilde{Z''}^2$ and scalar dissipation rate μ_χ, σ_χ as well as the flamelet relation $\rho = \rho(Z, \chi)$. The enthalpy, $h(\alpha)$, originating from the flamelet calculations is computed using $\wp(Z, \chi)$. The assumption that the enthalpy from the flamelet calculations $h(\alpha)$ coincides with the enthalpy from the CFD code, $\tilde{h}$, results in the determination of the heat loss parameter, α. With α and $\wp(Z, \chi)$, the values of $\overline{T}, \frac{d\overline{f}}{dt}$ and $\overline{\rho}$ can be found and the calculation is repeated until convergence is achieved.

Chapter 4

Results and Discussion

The formulation of combustion models is based on a series of assumptions made to reduce CPU time, as well as to obtain reasonable results. The flamelet concept is such an approach, where compromises are made in the description in order to model soot formation and other species concentrations in combustion processes. The steady flamelet model also has a reasonable accuracy compared with the unsteady flamelet model since it is used as a chemical preprocessor for source terms of soot formation. Since the unsteady flamelet model treats transient effects its accuracy is higher as will be shown in this chapter. A number of assumptions are made in the both models. This chapter describes the validation of the models for the formation of soot in laminar and turbulent diffusion flames. Different properties of soot formation and the dependence of soot formation on different flamelet models were studied. The models used were: the soot model, Section 2.3, the steady laminar flamelet model Section 3.3 and the unsteady laminar flamelet model Section 3.2. The models were coupled to an in-house CFD RANS code developed by Bai [144] (Sections 3.3 and 3.2). The effect of the flow model on the formation of soot is not investigated. The study was performed on two different flames: a turbulent ethylene/air flame and a laminar acetylene/nitrogen/air flame, generated with a mechanism including 855 reactions and 85 chemical species. The mechanism was taken from Mauss and Balthasar [108, 116] without modifications. Agglomeration will be introduced into the unsteady flamelet model and tested for the laminar flame in Section 4.2.3. Until that point the model follows the soot model described in Section 2.3 excluding the formation of agglomerates. Hence soot particles are assumed to be spherical.

Since the comparison of different models is described in this section, the structure of Section 4.1 describing studies on soot formation in turbulent diffu-

sion flames differs from Section 4.2 where soot formation in a laminar diffusion flame is described. This implies that there is much more to do, as discussed in Section 6. Atmospheric pressure is assumed at all times.

Since computation time sets the limit on every model, two approaches to reduce computation time will be discussed at the end of the chapter.

4.1   Turbulent Diffusion Flames

The example flame used to investigate the effect of different model assumptions is a turbulent ethylene/air diffusion flame. The experiments used for validation were taken from Young et al. [49]. An description of the experiment can be found in Section 1.2.3. The unsteady flamelet model was applied to study the affect of using higher moments during flamelet calculations and different factors relevant to surface reactions. Transient effects were then studied using the steady flamelet model and a comparison will be made with the unsteady flamelet model. Finally the relevance of preferential diffusion for the formation of soot using the steady flamelet model is discussed.

4.1.1   Convergence of the Momentum Method

The statistical method of moments applied in this work was previously described in Section 2.1.2. The direct simulation of the particle size distribution function can be replaced by an infinite number of equations describing the statistical moments of the PSDF. In order to save CPU time, many models only solve a limited number of moment balance equations. The validity and accuracy of this approach is the issue of this section. Balthasar [116] has shown that applying the solution of the method of moments to the determination of coagulation rates converges towards the solution of the Smoluchowsky equation when increasing the moments applied in the calculation. Convergence of the soot complete soot profile could be obtained including additional moments into the flamelet model. The active site parameter, which is the subject of Section 4.1.2, is set to 0.8. The surface growth is assumed to depend on the soot particle surface area.

Figures 4.1 (i) and (ii) were obtained with the unsteady flamelet model extended to four moments. Soot volume fractions including two, three and four moments were employed. Figure 4.1 (ii) presents a profile at a height of 250 mm above the outlet. The figures show the convergence towards one profile in soot volume fraction with increasing number of moments. The profile accounting for four moments is 40% lower than the profile including only one moment. Balthasar found that the deviation from the direct Smoluchowsky

calculations lay between 3% and 10% [116]. In order to save computation time, two moments will be considered in the following calculations. The deviation due to this two-moment assumption must be considered.

(i)

(ii)
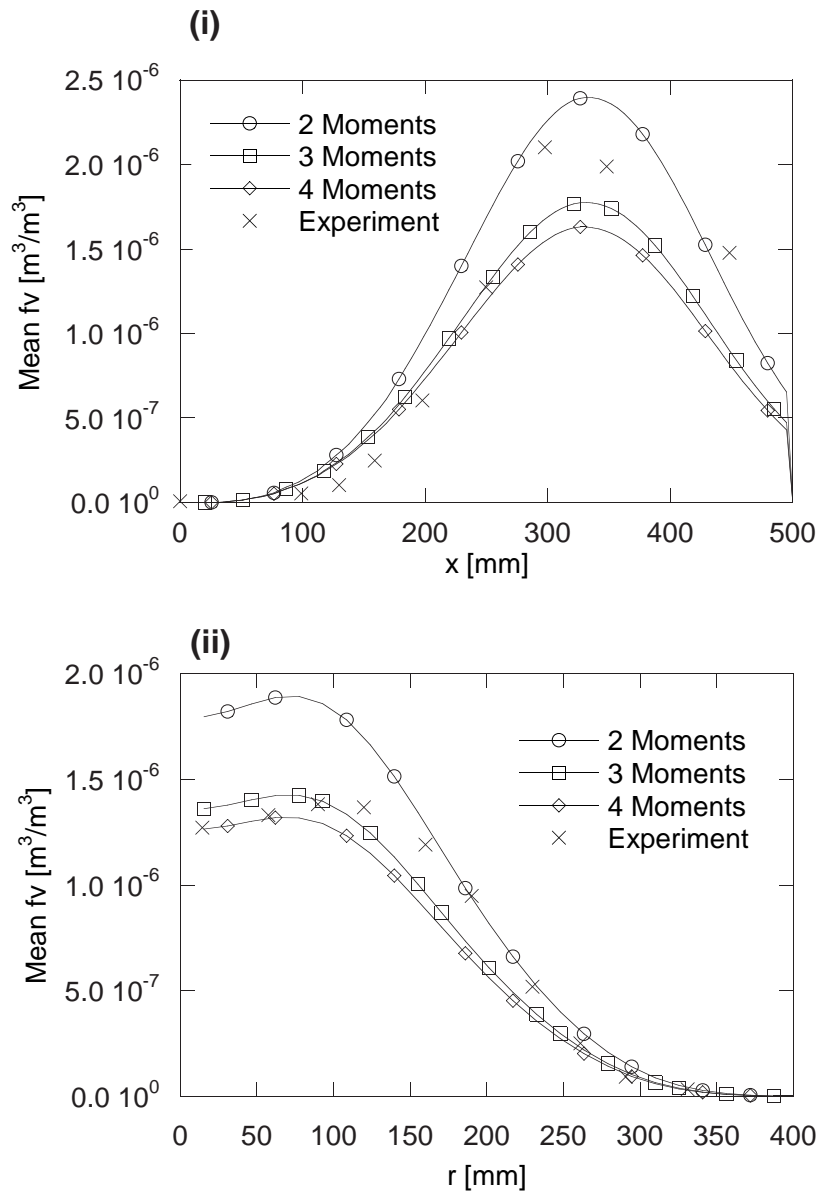
Figure 4.1: The mean soot volume fraction calculated with 2, 3 and 4 moments: axial position (i) radial position at x=250 mm (ii). The results are compared with experiments by Young et al. [49].

4.1.2 Relevance of Surface Reactions for Soot Formation

The process of soot surface growth was previously discussed in Section 2.3.3. In spite the fact, that the process has been the subject of many studies (see Haynes and Wagner [1]), many questions remain unanswered.

In the following the unsteady flamelet model considering two moments will be applied to study the change in on-axis soot volume fraction for different models of surface growth. The results will be compared with experiments by Young et al. [49].

Soot surface growth dependence

One of the questions still not answered is whether the growth of the soot surface can be modelled as a function of soot volume fraction (as claimed by Wagner et al. [118]), the soot surface itself (as postulated by Harris et al. [119]) or the number density as discussed previously.

The mean soot volume fraction is modelled using the unsteady flamelet model describing the turbulent ethylene/air flame described earlier. The active site parameter applied was 0.7, and the calculations were performed using two moments. The model is based on the following assumptions:

1. Soot surface growth is a function of the soot surface area.

2. Soot surface growth is a function of the number density of soot particles.

3. Soot surface growth is a function of the soot particle diameter raised to the power of 2.25.

Figure 4.2 (i) presents the axial mean soot volume fraction. Model modifications based on the three assumptions peak at the same point in space for all three models. The soot volume fraction is badly underestimated when assuming the surface growth to be a function of number density. This under-prediction is unaffected by the active site parameter, which is the subject of the next section. The result in best agreement with the experimental profile is that assuming the assuming the surface growth is a function of soot particle surface area.

Active sites

The active site parameter is another variable of interest. It describes the reactivity of the soot surface. The effect of a change in this parameter on soot volume fraction is illustrated in this section. The model applied is the unsteady flamelet model considering two moments. The surface growth is assumed to depend on the soot particle surface area.

Figure 4.2 shows three values of active site parameter assuming an reference active site parameter of $0.7 \pm 14\%$. The soot volume fraction changes by 30% when varying the activity of the site. It can be concluded that the active site parameter has considerable influence on the formation of soot in turbulent diffusion flames.
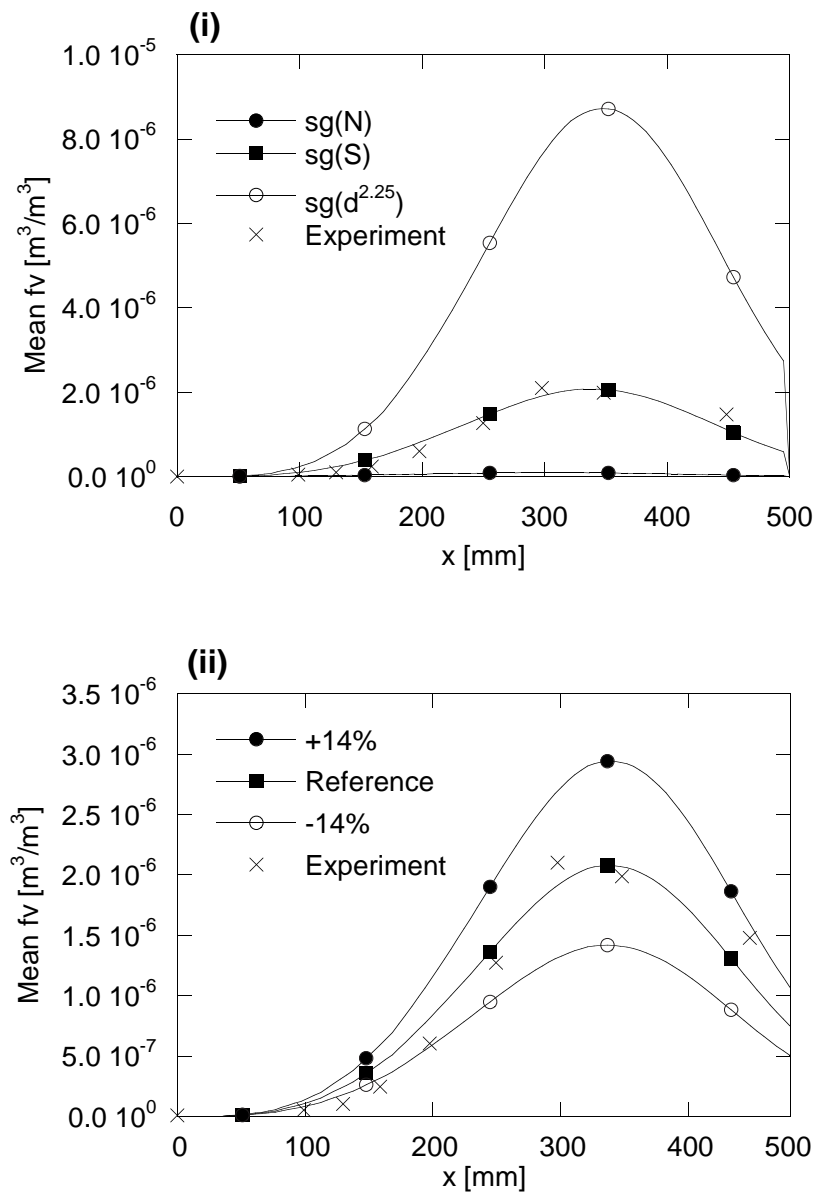
Figure 4.2: (i) The dependence of surface growth on the soot number density (●), the soot surface (■) and the diameter $d^{2.25}$ (○). (ii) Mean soot volume fraction as a function of the active site parameter, increased (○) and decreased (■) by 14%. The results are compared with experiments by Young et al. [49].

4.1.3   Transient Effects

As stated in Section 3, the flamelet can be in five different states [77]:

1. The steady, unreacted initial mixture

2. The unsteady transition after ignition

3. The quasi-steady burning state

4. The unsteady transition after quenching

5. The unsteady transition after re-ignition with the stationary states

Cases 1 and 3 describe time-independent states. They can be calculated prior to the CFD calculation using the steady flamelet model, and stored in a flamelet library. The time-dependent states 2, 4 and 5 must be calculated interactively with the CFD calculations. Slow chemical processes such as NO_X and soot formation reach the quasi-steady burning state on a much longer time scale than the fuel oxidation processes. This time scale may be longer than the typical flamelet lifetime. Hence, they are transient and can not be directly determined with the steady flamelet library concept. As described in Section 3.3, the source terms of slow-forming species can be calculated and the species concentration can be calculated by the CFD code. Another, more direct, way to account for transient effects on soot formation is to apply the unsteady flamelet model (Section 3.2) interactively with a CFD code.

In this section the soot source terms and the resulting mean soot volume fraction are calculated using both models and compared with experiments performed by Young et al. [49]. The unsteady model includes the assumption that the soot volume fraction is surface dependent. An active site parameter of 0.7, applied previously, and two moments are considered in the calculations. The steady laminar flamelet model is based on the assumption that the soot volume fraction is surface dependent. An active site parameter of 0.3 was applied in this model as mentioned previously (Section 4.1.4). The use different parameters is justified with the introduction of transient effects and the stronger influence of the turbulent flow field in the turbulent diffusion flame modelled with the unsteady flamelet model. Furthermore, the unsteady flamelet model is used to study the relevance of other transient effects, such as coupling to the gas phase, which are neglected when applying the steady flamelet model.

Comparison between the steady ad the unsteady flamelet models

The unsteady interactive flamelet concept is described in Section 3.2 accounts for transient processes such as ignition and extinction. The steady flamelet

model Section 3.3 does not consider these processes. To compensate for this, it can be used to calculate source terms for processes reaching the quasi-steady burning state on long time scales. The source terms are used in the transport equation in the CFD code, as described in Section 3.3.2. The model is validated for the description of soot formation in turbulent diffusion flames against the unsteady flamelet model.

One transient effect is the radiative heat loss which takes place on a long time scale. This transition is accounted for in the steady flamelet model by the radiation factor defined in Section 3.3. The inclusion of the radiation into the unsteady flamelet model is described in Section 3.2.

First, the two models will be compared. This is done by studying the source terms at one point in scalar dissipation rate space, and by investigating the complete soot volume fraction. The sources calculated with the steady flamelet model are extracted at a scalar dissipation rate of $\chi = 82s^{-1}$ and the source terms calculated using the unsteady flamelet model are extracted at one point of the time-dependent scalar dissipation rate space which expands along the stoichiometric iso-surface described in Section 3.2.5.

Calculated temperature profiles Figure 4.3 (ii) show the temperature as a function of mixture fraction for both models. The prediction of the models are rather close to each other. The source terms for soot formation and oxidation are effected when transient effects are accounted for in the model.

A comparison of the soot volume fraction calculated the unsteady flamelet approach and with the experimental data is shown in Figure 4.5. Source terms of particle inception, surface growth and oxidation are compared in Figures 4.3(i), 4.4(i) and (ii). The terms were modelled with both the unsteady flamelet approach and the stationary library approach at one point in enthalpy, scalar dissipation rate space. The rate of particle inception seen in Figure 4.4 (i) in the interactive flamelet model exceeds that of the steady flamelet approach. The difference between the results is within 25%.

The source terms for surface growth (Figure 4.4 (ii)) and oxidation (Figure 4.3 (i)) of the unsteady flamelet model are slightly smaller than the source terms of the steady flamelet model. In the following figures, the unsteady flamelet model is compared with the steady flamelet model which was coupled to a CFD code as previously described. Experimental data from Young et al. [49] are also presented. Figure 4.5 (i) and (ii) show the soot volume fraction as a function of axial position. The peak of the steady flamelet model is shifted downstream compared with experimental data and to the interactive flamelet model. This also affects the radial profile, where the mean soot volume fraction is slightly lower than that predicted by the interactive flamelet model (Figure 4.5 (ii)).

It can be concluded that the temperature profile in the flow field is in

reasonable agreement with the experimental data for both the steady and the unsteady flamelet model. Source terms coincide with an error of less than 25%. Both the steady and the unsteady flamelet approach agree fairly with the experimental results when modelling a turbulent ethylene/air diffusion flame. Nevertheless a deviation in the mean soot volume fraction can be seen. The unsteady model prediction of the mean soot volume fraction is closer to the experimental profile. It can thus be concluded that transient effects, such as radiation and coupling to the flow field, affect the modelling of soot formation.
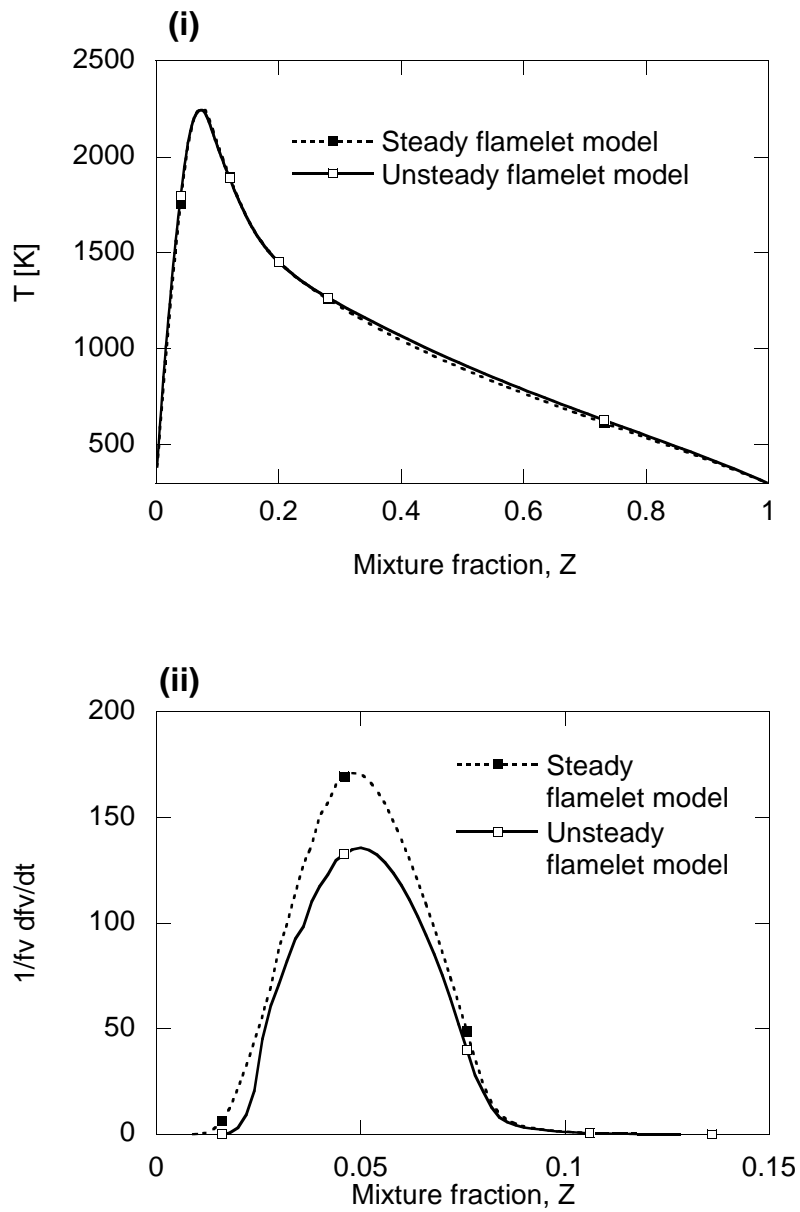
Figure 4.3: Comparison of the unsteady and steady flamelet model. (i) The maximum temperature at a scalar dissipation rate of $\chi = 82 \ s^{-1}$; (ii) Source terms of soot oxidation.

(i)

(ii)
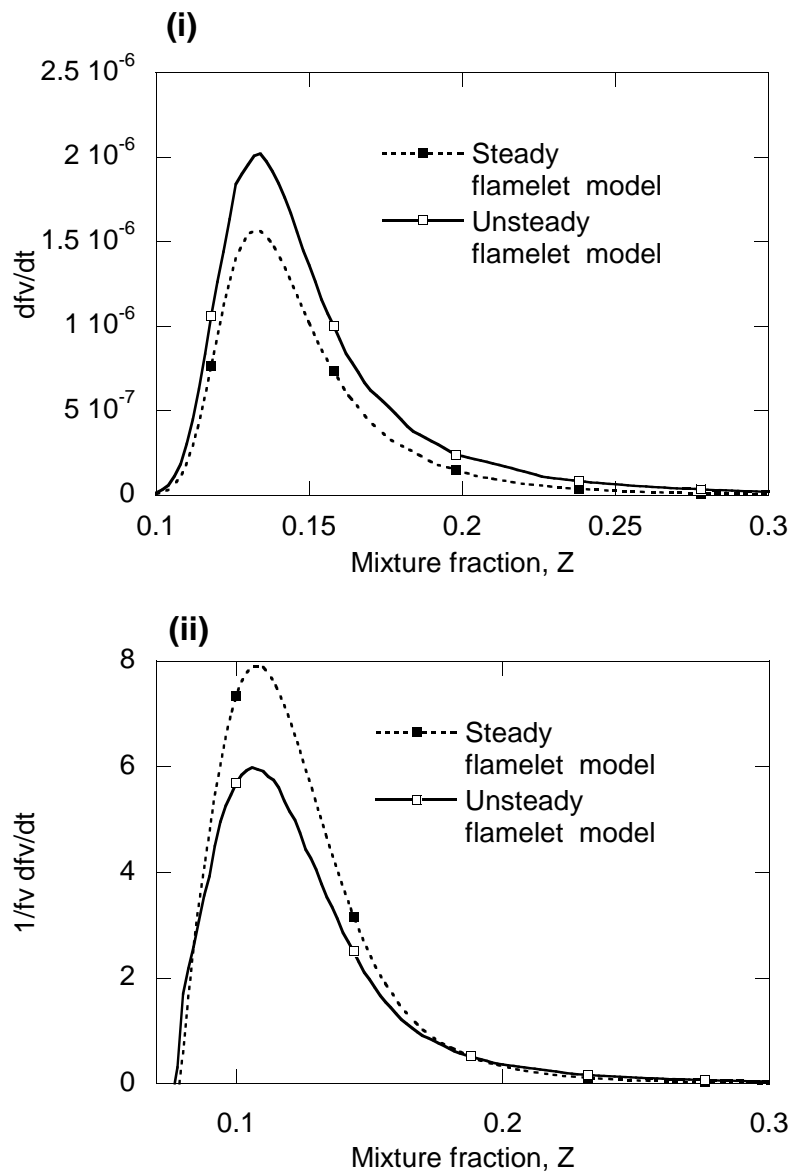
Figure 4.4: Comparison of the unsteady and steady flamelet model. (i) Particle inception; (ii) surface growth at a scalar dissipation rate of $\chi = 82 \ s^{-1}$.
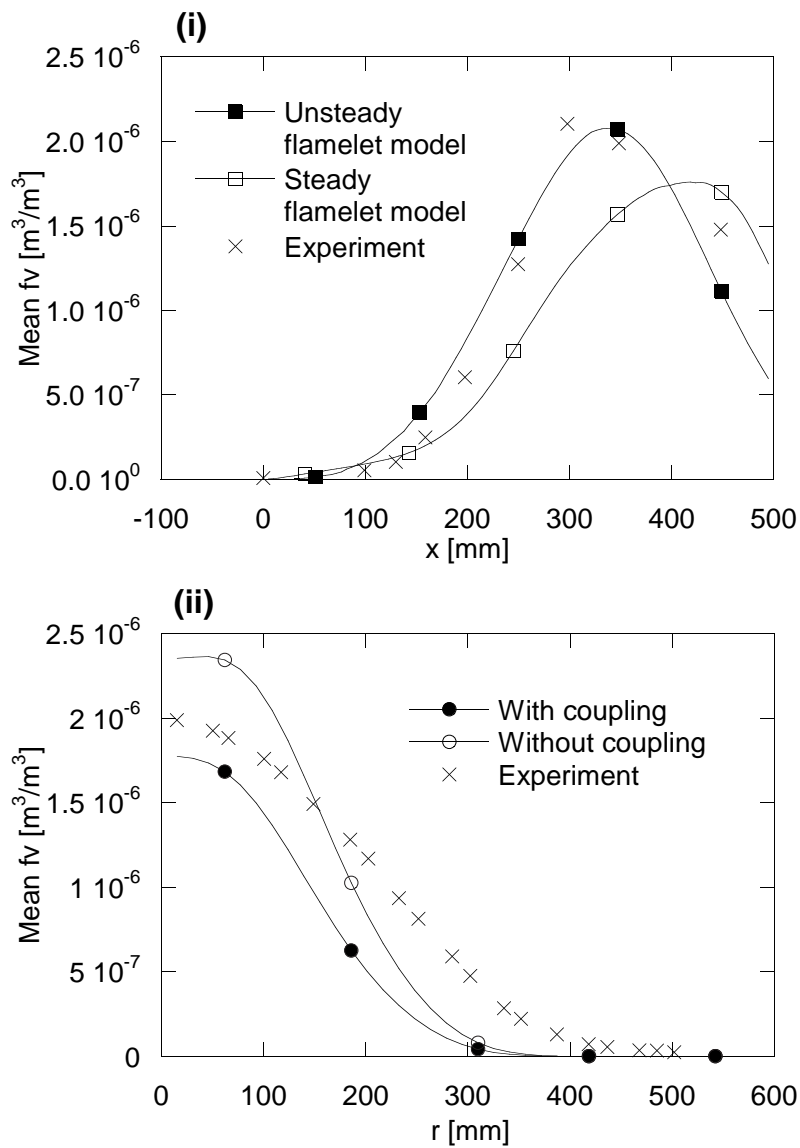
Figure 4.5: Comparison of the unsteady and steady flamelet model for mean soot volume fraction. (i) Axial and (ii) radial at x=250 *mm*. The results are compared with experiments by Young et al. [49].

Coupling to the gas phase

The soot model illustrated in Figure 1.11 can be split up into different stages. The first stage describes reactions in the gas phase with successive growth of the soot particles up to the size of agglomerates. The process involves heterogeneous reactions with the gas phase, during which the generated particles grow by reaction with gas phase species C_2H_2 and oxidize in reactions with O_2 and OH. The gas phase species C_2H_2, O_2 and OH are consumed in the process. The consumption of acetylene can not be included in the steady flamelet model since it depends on local concentrations, which are not known during the library calculations. The consumption also depends on the soot particles which are first modelled in the CFD code.

The unsteady flamelet code has been employed to study the relevance of this effect. An active site parameter of 0.7 and two moments are considered in the calculations. Soot formation is assumed to be soot-surface dependent.

Figure 4.6 shows the axial and a radial profile of the mean soot volume fraction including and excluding coupling to the gas phase species. The mean soot volume fraction decreases by 30% when the consumption of the gas phase species is included in the model of the turbulent flame.
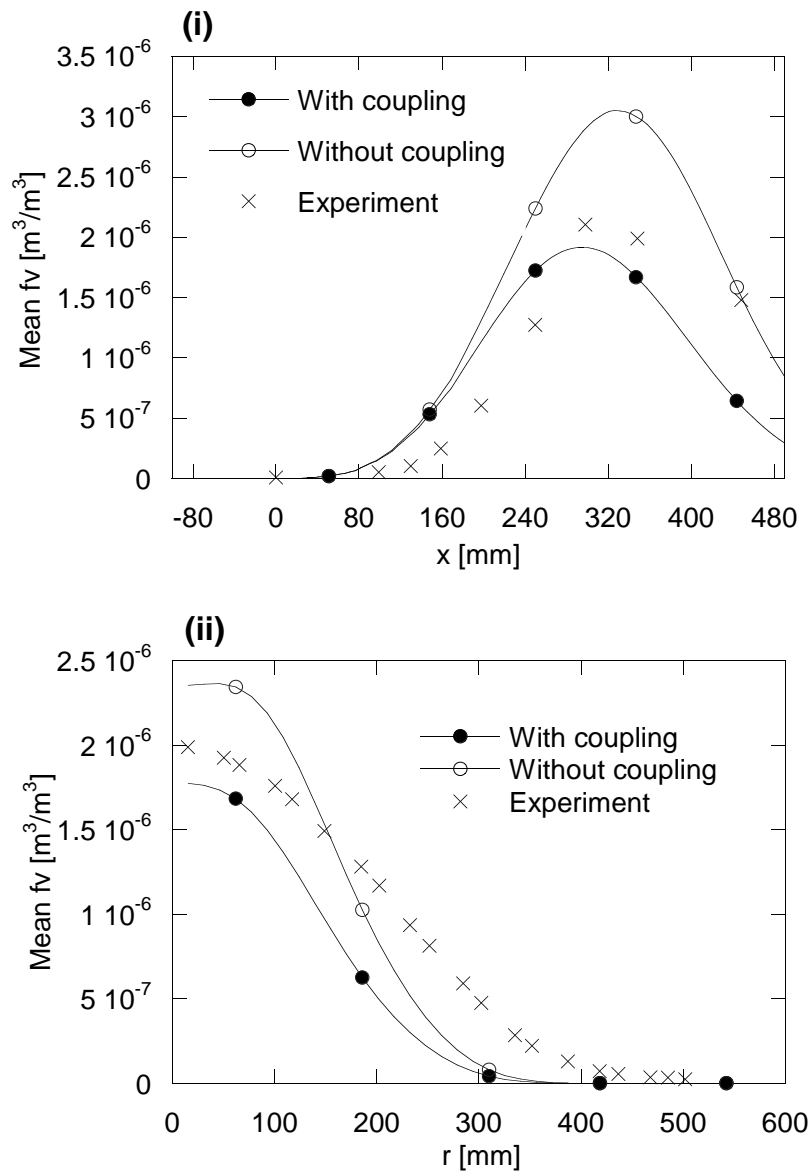
Figure 4.6: Comparison of the unsteady flamelet model including (•) and excluding (◦) the coupling to gas phase species mean soot volume fraction. (i) Axial and (ii) radial direction at x=250 *mm*. The results are compared with experiments by Young et al. [49].

4.1.4 Influence of Preferential Diffusion
on Soot Formation

The effects of differential diffusion on the flame structure have been studied by
Pitsch et al. [78]. The influence of species diffusion on the formation of soot in
a turbulent non-premixed ethylene/air flame is the subject of this section.

The soot model presented in Section 2.3 and the steady flamelet model
(Section 3.3) are used to calculate flamelet libraries containing the source terms
for soot formation. Two moments are considered. The soot volume fraction is
assumed to depend on the surface. An active site parameter of 0.3 is applied.
Frenklach and Wang [121] used an active site parameter of 0.35 to describe
soot formation in a laminar, premixed $C_2H_2/O_2/Ar$ flame at pressures of 12
kPa. The source terms are computed and tabulated for three different flamelet
models. They are defined using various modifications of the species diffusion
term. The libraries are used in a flow code developed by Bai [144] to calculate
a turbulent jet diffusion flame. The results are compared and validated with
a corresponding experiment by Young et al. [49]. Three different diffusion
models were employed.

- Model 1: The model is based on the assumption the Lewis numbers is
  unity for all species. This model implies that the diffusion is the same for
  all species. The results are obtained using species conservation (Equation
  3.85), momentum conservation (Equation 3.86) and energy conservation
  Equation 3.89.

- Model 2: The model is based on the assumption that the Lewis number
  of each species is constant. They are considered to be unity for all species
  except H and H_2. This implies that the diffusion of the lightest species is
  considered. The results are obtained using species conservation (Equation
  3.75), momentum conservation (Equation 3.78) and energy conservation
  (Equation 3.81).

- Model 3: A complex diffusion model is applied to all species. Preferential
  diffusion is taken into account. The results are obtained using species
  conservation (Equation 3.67), momentum conservation (Equation 3.70)
  and energy conservation (Equation 3.73).

Figures 4.7-4.8 show the influence of preferential diffusion on the source terms
for soot formation. The rate of soot particle inception (Figure 4.7 (i)), soot
surface growth (Figure 4.7 (ii)) and soot oxidation (Figure 4.8 (i)) as a function
of the mixture fraction for a scalar dissipation rate at stoichiometric condition
$\chi_{st} = 10s^{-1}$ was studied for all three models.

The resulting source terms for the complex diffusion (Model 3) are close to those computed with the constant diffusion (Model 2). Assuming a Lewis number of unity (Model 1) results in higher values for the oxidation (Figure 4.8 (i)), lower values of particle inception (Figure 4.7 (i)) and lower surface growth (Figure 4.7 (ii)), hence the soot volume fraction calculated with this model is lower (Figure 4.9). This result is achieved by coupling the flamelet library to the in-house CFD RANS code developed by Bai [144]. The agreement between experiments and calculation in the axial and the radial directions are best for the model accounting for preferential diffusion, but the model assuming constant Lewis number also gives reasonable results.

However, the calculated axial profile is shifted 50 mm downstream compared with the experiments. It appears that Model 2 gives the best agreement with the experiments. Soot oxidation occurs too late in all models, but Model 2 reaches a maximum mean value very close to the values found in experiments. Furthermore, a profile mapping the maximum temperature as a function of scalar dissipation rate is shown in Figure 4.8 (ii). The profile for the complex diffusion model follows the tendency already seen in the profile for the source terms and is close to the constant diffusion model. The temperature for the unity Lewis number diffusion model is higher.

It has thus been shown that preferential diffusion has an effect on soot formation in turbulent diffusion flames. The physical transport in the flow has a considerable impact on the flame. Also it can be considered to be sufficient to assume a constant Lewis number for all species.

(i)

(ii)
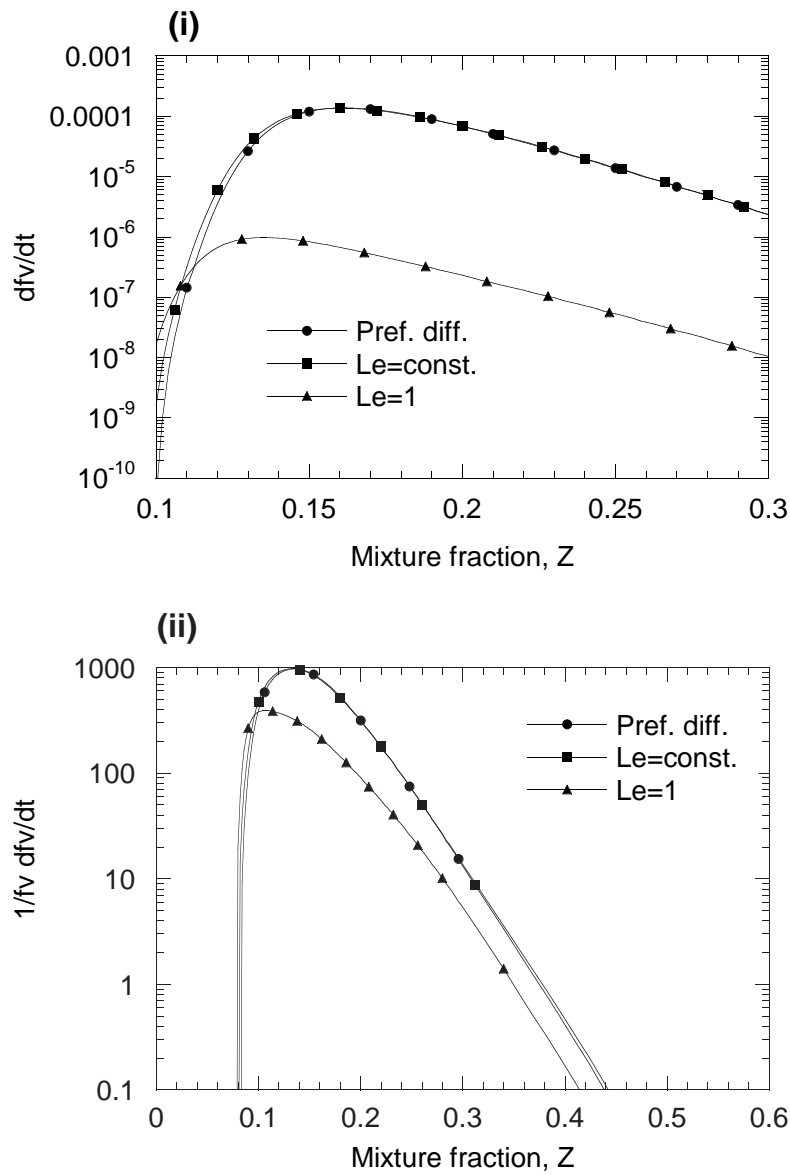
Figure 4.7: The source terms at a scalar dissipation rate of $\chi_{st} = 10 \ s^{-1}$ for particle inception (i) and surface growth (ii).
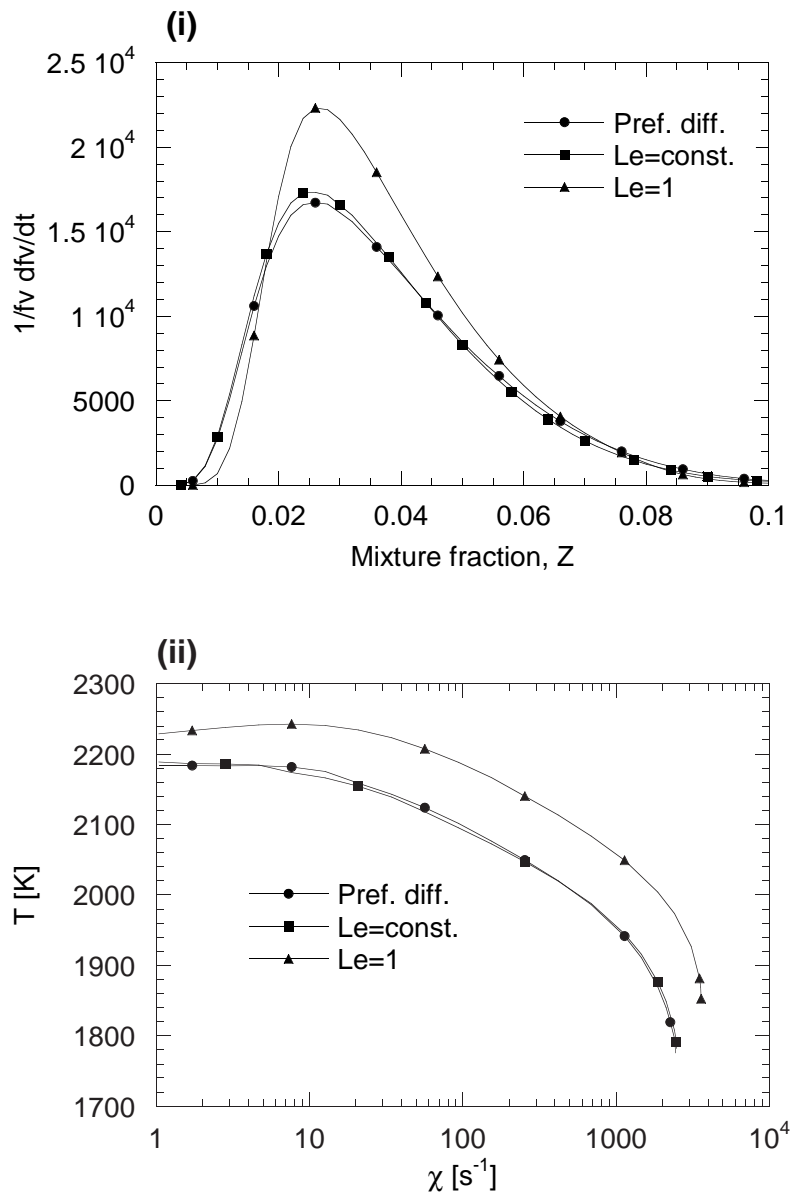
Figure 4.8: The source terms at a scalar dissipation rate of $\chi_{st} = 10\frac{1}{s}$ for oxidation (i). Temperature profile as a function of scalar dissipation rate at stoichiometric mixture (ii).
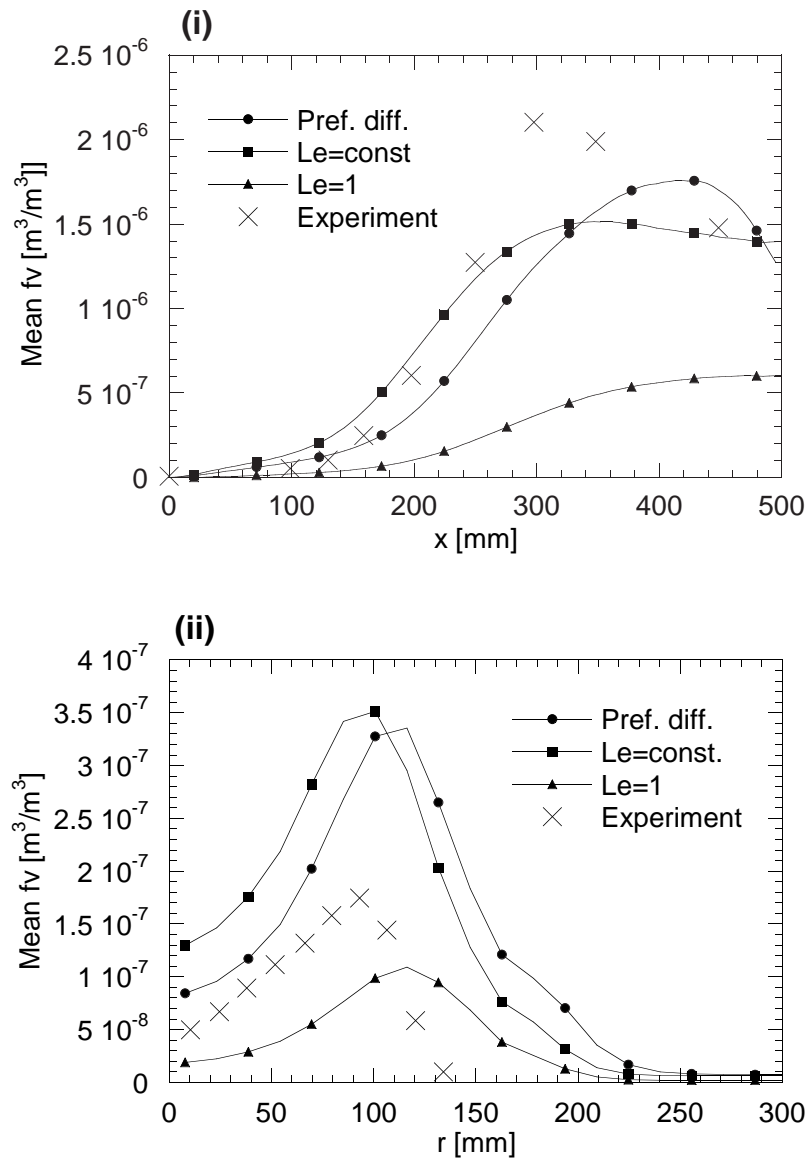
Figure 4.9: Mean soot volume fraction on axial (i) and at radial position (ii) at x=100 mm. The results are compared with experiments by Young et al. [49].

4.2 Laminar Diffusion Flames

The focus of this section is soot formation in laminar diffusion flames using the unsteady flamelet model. The model flame is a laminar acetylene/nitrogen diffusion flame. The results are compared with experiments performed by Xu and Feath [33]. The experimental approach is described in Section 1.2.4. The experiments only give axial results. However, some radial results will be presented in this discussion. The effect of transient effects on soot formation in laminar diffusion flames calculated with the unsteady flamelet model is discussed first in this section. The formation of agglomerates is then coupled to the model and applied in the next three sections. The effect of the introduction of agglomerates on soot formation, the importance of different factors relevant for surface reactions, as well as transient effects, are studied at the end of the section.

4.2.1 Influence of Surface Reactions on Soot Formation

The process of soot surface growth was previously discussed for turbulent diffusion flames, in Section 4.1.2. This section deals with the effects on laminar acetylene/nitrogen/air flames.

Soot surface growth dependence

The questions of whether the growth of the soot surface can be modelled as a function of soot volume fraction [118], the soot surface itself [119] or the number density is posed in this section. The focus of this section os to study the effect of the previously described surface effects on laminar diffusion flames using the unsteady flamelet approach.

   The mean soot volume fraction is modelled using the unsteady flamelet model describing the laminar acetylene/nitrogen/air flame described above. The active site parameter was set to 0.25 and two moments were considered. The results are compared with the experimental data of Xu and Feath [33]. As in Section 4.1.2, the models are based on the following assumption:

1. Soot surface growth is a function of the soot surface.

2. soot surface growth is a function of the number density.

3. soot surface growth is a function of the soot diameter to the power of 2.25.

Figure 4.10 (i) presents the mean soot volume fraction in axial direction. The maximum of soot volume fraction for the models based on the three assumptions coincide in space have the same order of magnitude. The soot volume fraction is still underestimated when assuming the surface growth to be a function of number density. The profiles predicted by the model assuming that the surface growth is a function of the soot surface are close to those predicted by the model assuming the surface growth is a function of $d^{2.25}$. Both profiles agree reasonably with experimental data.

Active sites

Figure 4.10 shows three values of the active site parameter. The reference value of the parameter of $0.25 \pm 14\%$. The parameter is by a factor 0.7 lower than the the parameter applied by Frenklach and Wang [121] for a laminar premixed $C_2H_2/O_2/Ar$ flame at pressures of 12 kPa. The soot volume fraction was assumed to depend on the surface are of the soot particles. The soot volume fraction changes by 8% when varying the activity of the site by 14%. It can be concluded that the active site parameter influences the formation of soot in laminar diffusion flames. The effect is not as large as for turbulent flames. This is due to the fact that the flame is laminar and the turbulent mixing, which supplies the particle in radicals does not affect the process. The active site parameter decreases with the absence of radicals [1].
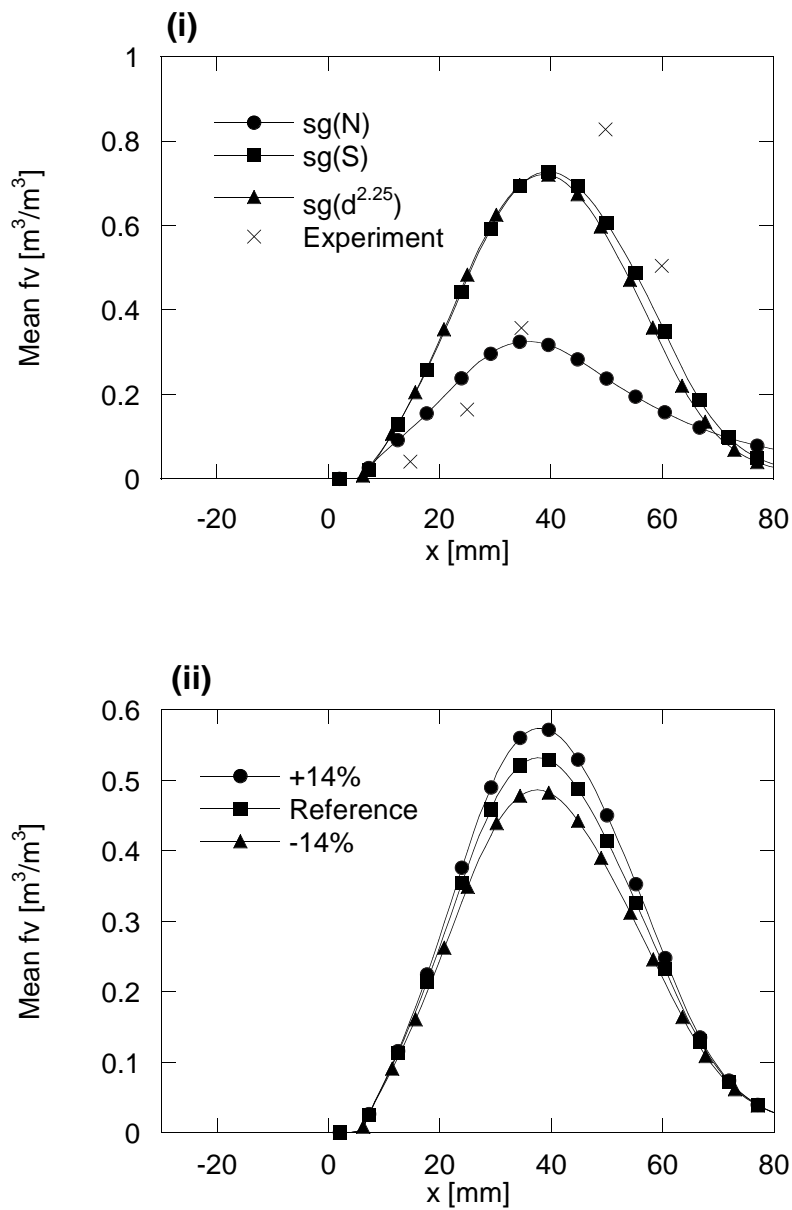
Figure 4.10: (i) The dependence of the surface growth on the soot number density ($\bullet$), the soot surface ($\blacksquare$) and the diameter $d^{2.25}$ ($\circ$). (ii) Mean soot volume fraction as a function of the active site parameter, increased ($\circ$) and decreased ($\blacksquare$) by 14%. The experimental data are from Xu and Faeth [33].

4.2.2   Transient Effects

Transient effects play an important role in laminar flames where the influence of the flow field is weak compared with turbulent flames. This implies that the chemical processes have a stronger effect. The relevance to gas phase coupling was studied for soot formation in the laminar acetylene/nitrogen/air flame.

The radiative heat loss, which is also a transient effect, is accounted for in the unsteady flamelet model as described in Section 3.2.

Coupling to the gas phase

The unsteady flamelet code has been employed to study the effect of the inclusion of the coupling to the gas phase in laminar diffusion flames. Two moments are considered and the active site parameter was set to 0.25. The soot volume fraction depends on the surface area of the soot particle.

Figure 4.11 shows the axial and a radial profile at a height of 33 mm above the outlet of the mean soot volume fraction. The profiles show a comparison of the unsteady flamelet model including and excluding the coupling to the gas phase species. The mean soot volume fraction decreases by 40% when the consumption of the gas phase species is included in the model of the laminar flame. It appears to be 10% higher than for the turbulent flame Figure 4.6. This can be explained by the fact that the influence of the flow field is greater for turbulent flames than for laminar flames.
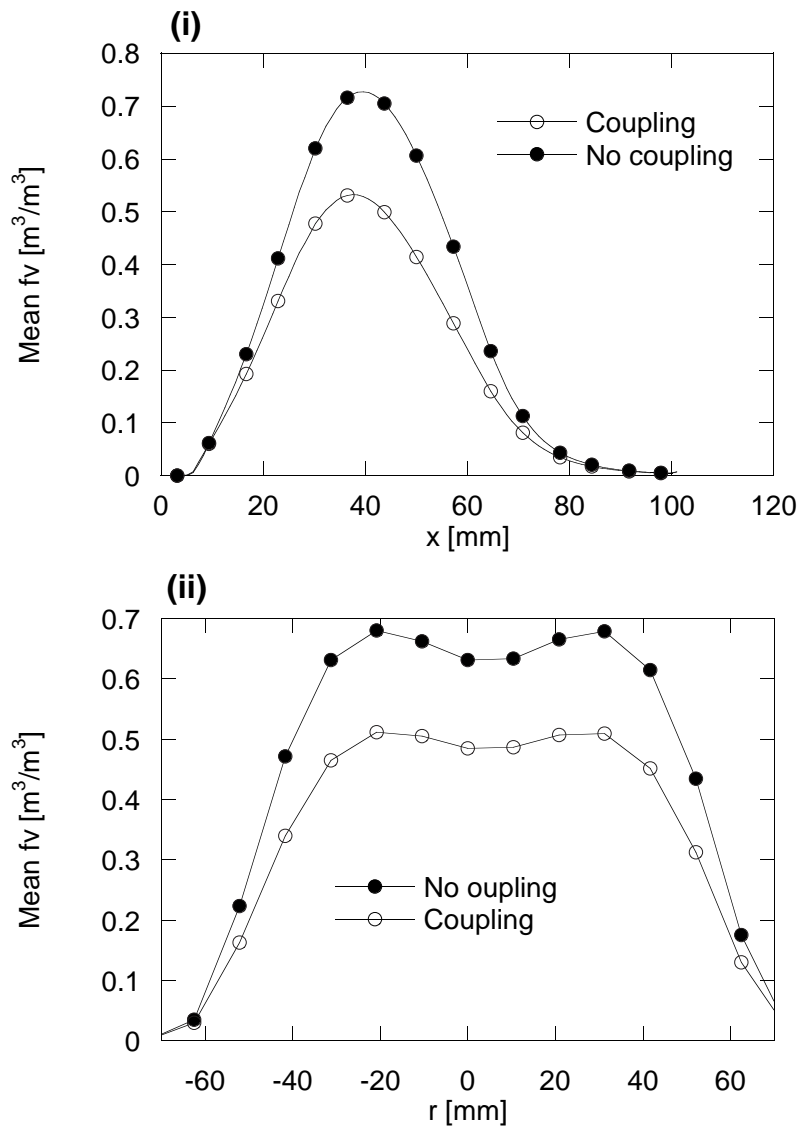
Figure 4.11: Comparison of the unsteady flamelet model excluding($\bullet$) and including ($\circ$) the coupling to gas phase species mean soot volume fraction: (i) axial and (ii) radial at x=33 mm. The results were validated with the experiment by Xu and Faeth [33].

4.2.3   Formation of Agglomerates

As discussed in Sections 1.4 and 2.3.5, soot particles form build agglomerates at a certain stage. This process has been included in the unsteady flamelet model and is treated statistically. The combustion state was found to be completely in the molecular regime. Neither the transition regime, nor the continuum regime were entered at any time (Section 2.3.5). This can be explained by the atmospheric pressure as demonstrated by Pels Leusden [135], and the small particle size relative to the number density. Hence, the agglomerates were built in the free molecular regime.

Instead of "switching on" the agglomeration when the critical diameter d_c is reached, the process is started smoothly using a diameter-dependent pre-factor, Γ, in the code:

$$\Gamma = \frac{0.5 \cdot 10^9 tanh(\Delta D) + 1}{2} \qquad (4.1)$$

The smooth formulation of the factor has the advantage of improving the convergence of the computation.

In order to include the decay of the scalar dissipation rate along the jet axis and other transient effects, the unsteady flamelet model was applied to study this laminar flame where it is assumed that a laminar flamelet is transported through the flame. The scalar dissipation rate, χ, is calculated interactively with the CFD code. The scalar dissipation rate is assumed to be a function of mixture fraction space and a function of time, propagating along the stoichiometric iso-surface, with $\chi(\tau) = \chi(\tau_{st})$. Since the maximum mixture fraction changes upstream, the value of the maximum mixture fraction for each flamelet is determined by the CFD code. This also affects the scalar dissipation rate. In order to account for this evolution, the following normalized, Gaussian-shaped scalar dissipation rate is applied:

$$\chi(Z) = \frac{\chi(Z_{CFD})}{\chi_{\max}(Z)} \; for \; Z \leq Z_{\max}; \quad \chi = 0 \; for \; Z > Z_{\max} \qquad (4.2)$$

The formation of soot agglomerates, (Section 2.3.5), in laminar diffusion flames using the unsteady flamelet model (Section 3.2) was investigated for a laminar acetylene/nitrogen diffusion flame. As for the model not considering agglomerates, the soot volume fraction, species concentrations and soot diameter were calculated interactively with the inhouse CFD RANS code by Bai [144], as described in (Section 3.2.6) and compared with experiments performed by Xu and Feath [33] (Section 1.2.4). Two moments were considered, as in the previous section, and the active site parameter was set to 0.25. Figures 4.13 show that the model agrees well with the experiments for species concentrations such as CO, CO_2 and the fuel itself C_2H_2. Figure 4.14 (i) shows the axial profile of

the mean soot volume fraction. The profile shows a peak and a saddle, which are shifted downstream compared with the experimental data. The saddle is due to agglomeration, and can be seen for both the experiment and the model. Figure 4.15 shows a comparison between a model including and excluding the agglomeration. The results are shown as axial (i) and radial (ii) plots. The saddle does not occur if agglomeration is not considered. The flame is also shifted upstream. The model including the process of agglomeration agrees better with experimental results. Figure 4.14 (ii) shows the diameter of the primary particles. The prediction agrees well with experiments. As for the mean soot volume fraction, the profile is shifted upstream compared with the experiments. Oxidation affects the modelled diameter more strongly than the experiments. This is due to the temperature profile, which peaks later than in the experimental results.
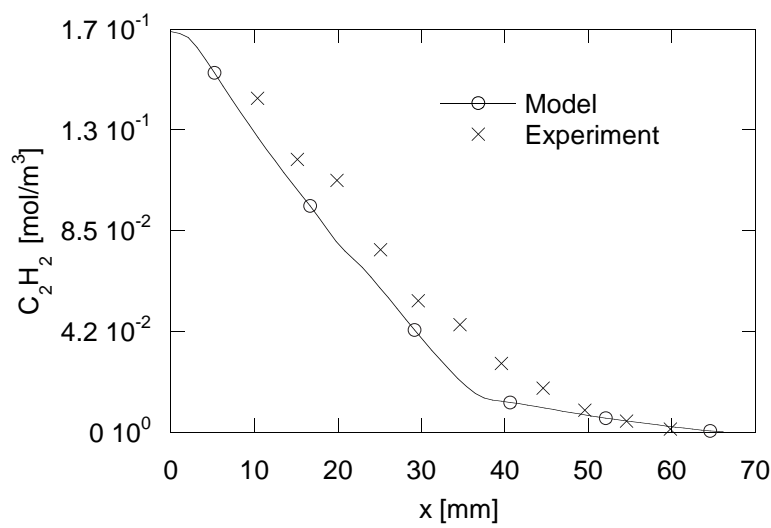
Figure 4.12: Axial profile of the fuel concentration ($\circ$). The experiment was performed by Xu and Faeth [33].
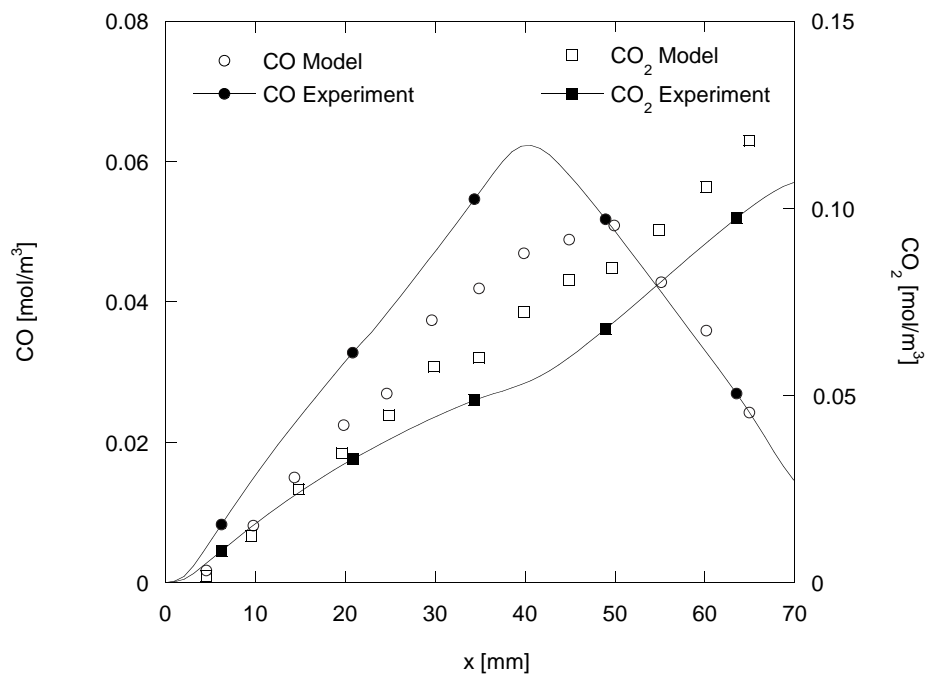
Figure 4.13: Axial profile of species concentration of CO ($\bullet$, $\circ$) and CO_2 ($\blacksquare$, $\square$). The experiment was performed by Xu and Faeth [33].
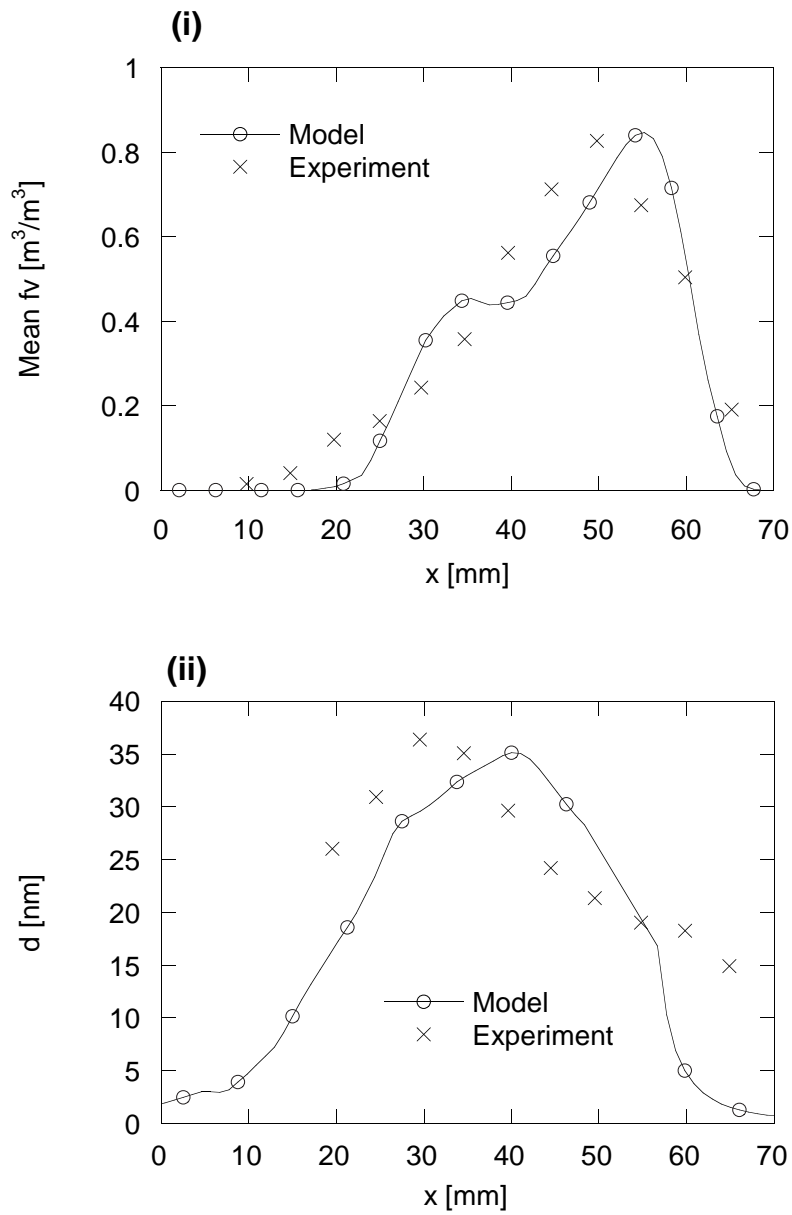
(i)

(ii)

Figure 4.14: Mean soot volume fraction on axis (i). Diameter of primary soot particles (ii). The experiment was performed by Xu and Faeth [33].
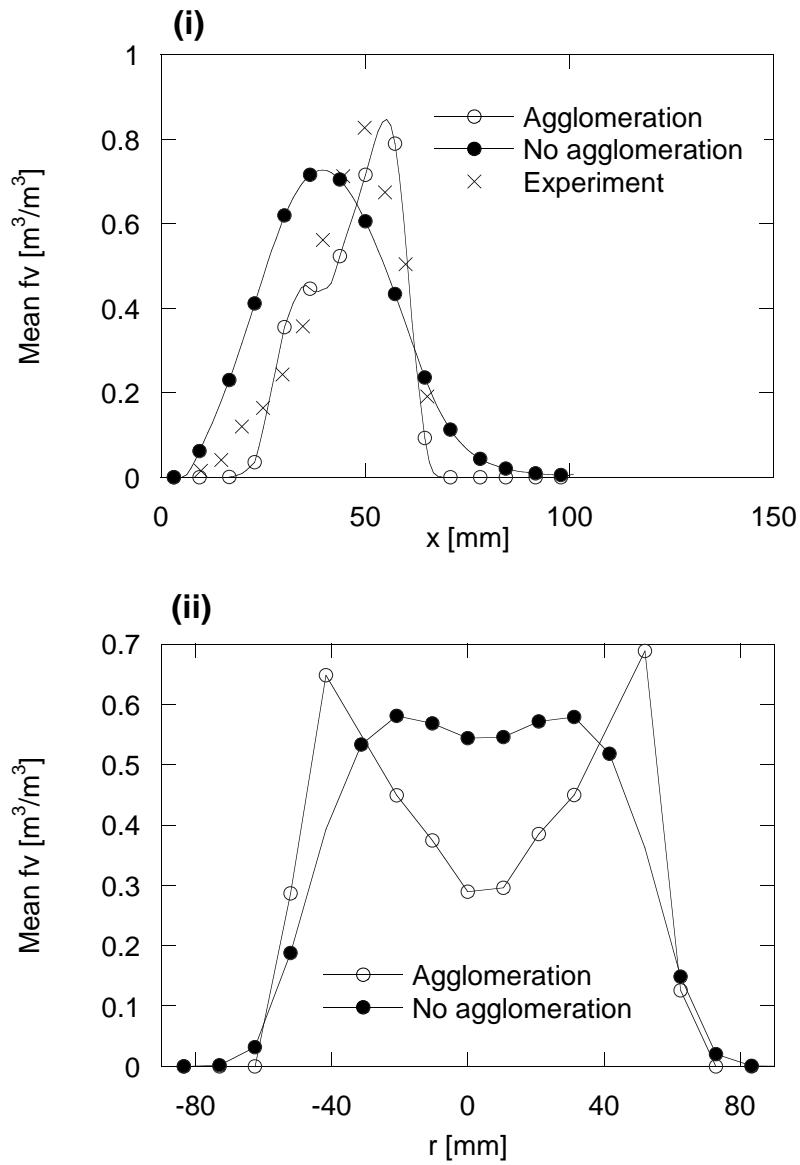
Figure 4.15: Mean soot volume fraction on axis (i). Diameter of primary soot particles (ii). The experimental data were taken from Xu and Faeth [33].

Figure 4.13 shows good agreement with the experiments for the fuel (i) and the oxidizer (ii). The soot volume fraction (i) and the diameter of the primary particles (ii) are shown in Figure 4.14. They agree well with the experimental results. The plateau in the soot volume fraction is seen both for experiments and for the modelled soot volume fraction. This can be explained by the beginning of the process of agglomeration, which is set to start smoothly when a critical diameter $d_c = 10\ nm$ is reached. All soot results are shifted upstream compared with the experiments.

4.2.4 Relevance of Preferential Diffusion for the Process Soot Formation

The effects of differential diffusion on soot formation in turbulent flames were described in Section 4.1.4. This section deals with the influence of the species diffusion on the formation of soot in a laminar non-premixed acetylene/nitrogen/air flame.

   The study concerns soot formation when the process of agglomeration is accounted for (Section 2.3), the active site parameter is set to 0.25, and two moments are considered. The model used here is the unsteady flamelet model (Section 3.2). The results were validated with the experimental data by Xu and Faeth [33]. As before, the study is based on three different diffusion models:

- Model 1: The model bases on the unity Lewis numbers assumption for all species. This model implies that all species diffuse equally.

- Model 2: The model bases on the assumption that the Lewis numbers of each species are constant. They are considered to be unity for all species except for H and H_2. This implies that the diffusion of lightest species is considered.

- Model 3: A complex diffusion model is applied for all species.

Figure 4.16 shows the mean soot volume fraction predicted by the three models, on axis (i) and in the radial direction (ii) at x= 33 mm. The resolution of the radial profile is very poor and no experimental data with which the prediction can be compared. The result is presented anyways since is shows the effect in radial direction. The model including detailed diffusion of all species (Model 3) agrees best with the experimental results. In contrast to the turbulent flame (Section 4.1.4), Figure 4.9 the profile of the complex diffusion model does not agree well with the model assuming unity or constant Lewis numbers. The peak in mean soot volume fraction is a factor 2 lower than in the experiments and considerably shifted upstream. This implies that diffusion plays a greater

role in laminar flames than in turbulent flames contributing to the growth of agglomerates. It is thus not sufficient to apply simple diffusion models when describing laminar flames.
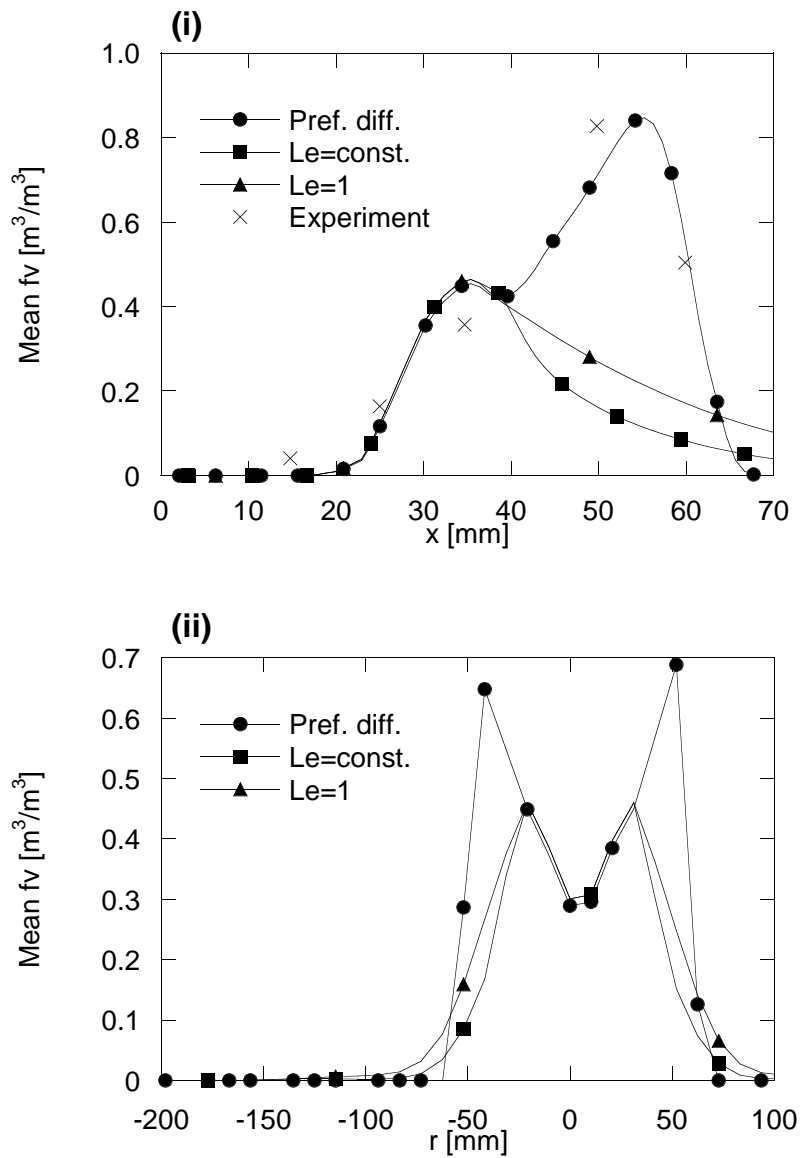
Figure 4.16: Mean soot volume fraction on axial (i) and at radial position x=33 *mm* (ii). The experimental data were taken from Xu and Faeth [33].

4.3   Methods of Reduction

The determination of pollutant formation in diffusion flames is time-consuming. The time limitation of the methods is the reason why theoreticians are forced to prioritize. Often they choose to work either with the physics of the flow or detailed chemistry. Saving time and making use of both the physical and chemical descriptions of combustion systems is of great interest. The flamelet model offers a way of combining detailed chemistry with physical information in flow calculations. In order to save computation time and improve the applicability of the models, two approaches to reduce computational effort will be presented here. The goal of the first the reduction of computation time during chemical calculations. The second is concerned with the steady flamelet model and describes ways of compressing flamelet libraries and introducing them into any flow calculation in a simple manner.

4.3.1   Online Reduction of Reaction Mechanisms during Unsteady Flamelet Calculations

The work described in this subsection is based mainly on the work by Fikret Saric, Saric and Dederichs [148]. A detailed chemical mechanism containing 66 species was used to calculate species concentrations in a turbulent ethylene/air flame using the unsteady flamelet model. An online reduction principle was applied in these calculation. Species with a short lifetime $2 \; 10^{-6}$ s were excluded from the calculation. Thirty-nine species were removed from the calculations (H, O, OH, HO_2, CH, HCO, $1-CH_2$, $3-CH_2$, CH_3, CH_3O, CH_2OH, C_2H, $HCCO$, C_2H_3, CH_2CHO, OCH_2CHO, CH_3CHO, C_2H_5, C_3H_3, C_3H_4P, C_3H_5, N-C_3H_7, I-C_3H_7, C_4H_2, C_4H_3U, C_4H_3S, C_4H_5U, C_4H_5S, C_4H_6, C_4H_7, 1-C_4H_8, 2-C_4H_8, C-2-C_4H_8, P-C_4H_9, S-C_4H_9, C_6H_5U, C_6H_6, C_6H_7U, CO), which implies a reduction in the size of the Jacobian matrix. The results shown in Figures (4.17-4.19) show fair agreement between the species concentration and the temperature profiles when applying the detailed mechanism and the reduced mechanism. The temperature deviates with maximal 3% and the H concentration with less than 15%.
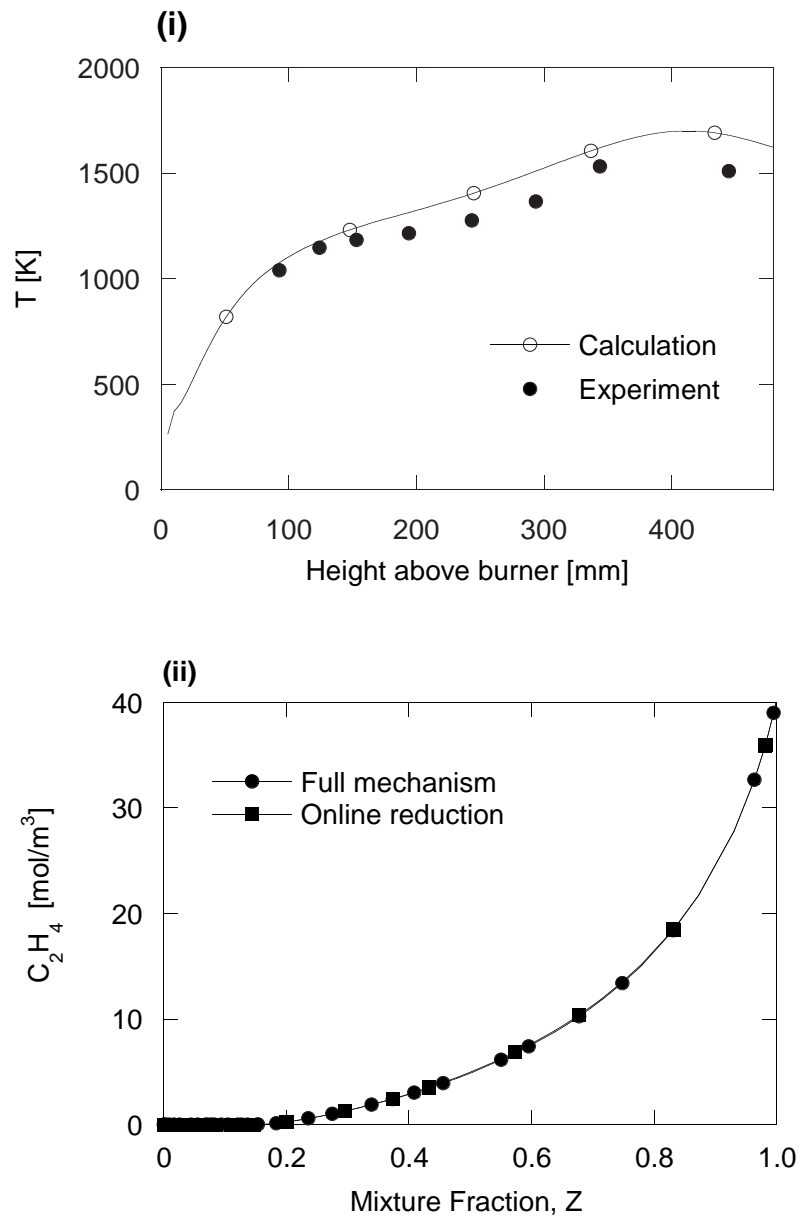
Figure 4.17: Temperature profile for the detailed model (i). Comparison of the fuel concentration as a function of mixture fraction computed with the full (•) and the reduced mechanism (■) (ii).
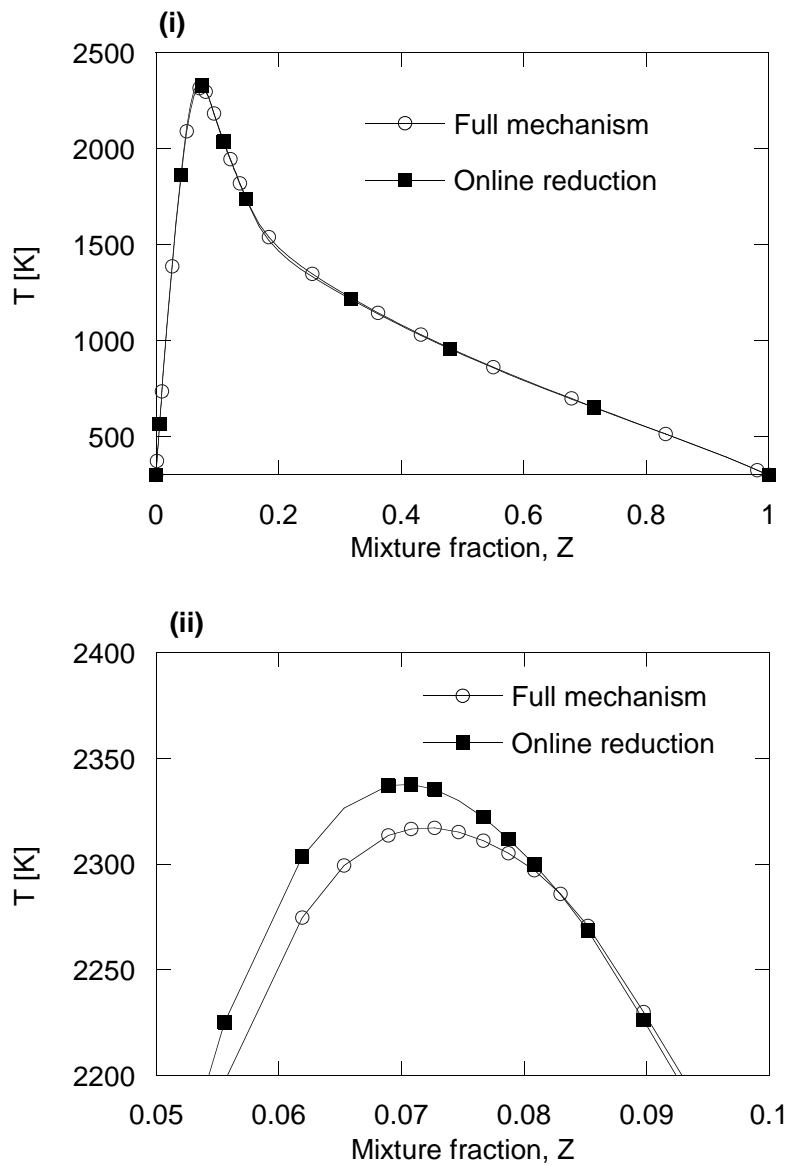
Figure 4.18: Comparison of the temperature as a function of mixture fraction computed with the full (∘) and the reduced (■) mechanism (i). (ii) shows the difference of 3% between the models.
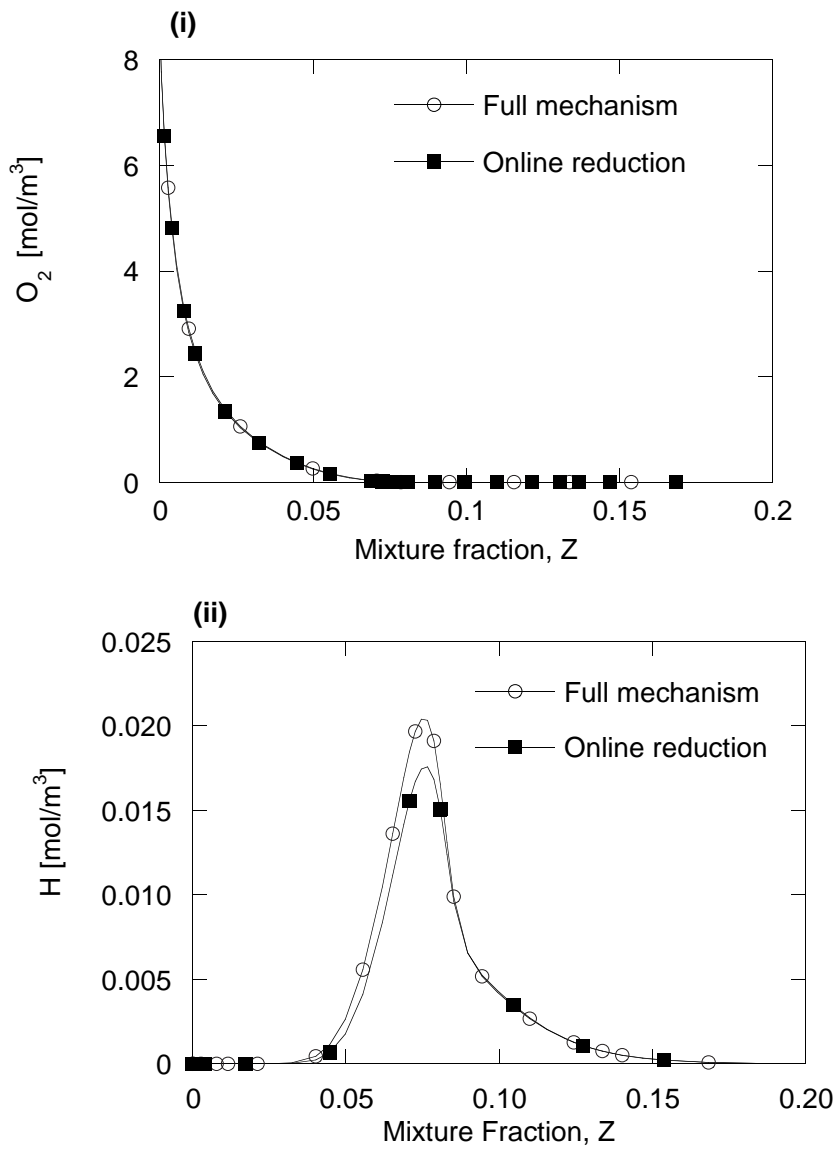
Figure 4.19: Comparison of the O_2 profile (i) and H profile (ii), as function of mixture fraction computed with the full ($\circ$) and the reduced ($\blacksquare$) mechanism.

4.3.2   Compression of the Flamelet Libraries

The previous section focussed on data compression during calculation. As mentioned above, this process results in increased CPU consumption due to convergence problems, caused by a change in Jacobian. Post-process data compression methods do not suffer from these problems.

Data compression is a subject studied by scientists in many fields. The data sets produced in the steady flamelet library are space consuming. The model is interesting because of its compatibility with any CFD code. Since large libraries are not easy to implement, elegant data compression is of interest. The goal is to develop subroutines and functions describing the soot source terms as functions of mixture fraction, scalar dissipation rate, enthalpy, radiation parameter, temperature and pressure. Numerous approaches have been described in literature which could be and have been applied for such a purpose.

Limiting factors which should be considered in this context are the CPU time required to generate the memory of the generated data, the error associated with the reduction process, the CPU time required to retrieve the filtered data, and the applicability of the method. Examples are given below.

- The discrete wavelet transform (DWT) presents as filter applicable to data fields, using a recursive partitioning approach. Another application is in the reduction of the differential equations [149].

- Computationally efficient implementation of combustion chemistry using *in situ* adaptive tabulation (ISAT) has been undertaken by Pope [150]. The method is based on tabulating the physical and chemical evolution of combustion processes in a condensed way.

- Neural networks coupled to Pope's ISAT method [150] has been applied by Chen et al. [151] to reduce storage space of chemical kinetic data by more than a factor of 100.

- Intrinsic low-dimensional manifolds (ILDM) described by Maas and Pope [55] define the time evolution of one species as a function of other major species thereby reducing computation time and memory requirements.

- The multi-adaptive regression spline or so-called MARS method, developed by Friedman [152] offers flexible regression modelling of high-dimensional data. It makes use of spline basis functions and tunable parameters such as order and knot locations using a recursive partitioning approach. It is capable of modelling multivariable interactions.

The goal of the method described in this section is to compress libraries containing source terms of soot.

Flamelet libraries

Flamelet libraries contain data which has been calculated using the steady flamelet model. In our case the data are source terms of chemical reaction such as the soot and physical properties such as the radiative heat release.

The source terms for soot formation: As described in Section 3.3 the steady flamelet model may not be used to model transient effects such as soot formation. Instead the source terms for soot formation and reduction can be calculated and stored. They are functions of temperature, mixture fraction, scalar dissipation rate, enthalpy and the radiative heat loss parameter α.

The radiative heat loss: The radiative heat loss is another term suitable for being pre-calculated and stored in flamelet libraries. It affects the temperature profile and has great influence on the flamelet. At the same time the black-body radiation of soot particles present a strong contributor to the total radiative heat loss. It depends strongly on the fluctuations of the temperature in the turbulent flame. The influence of the radiative heat loss increases with decreasing scalar dissipation rate. The time needed to gain a stationary profile of a flamelet cooled by radiation is much longer than the flame residence time. Radiation is therefore a transient effect and needs to be modelled when stationary flamelet libraries are used. Radiation losses can be pre-calculated using the steady flamelet model (Section 3.3) similar to the calculations of the source terms for soot formation. The source terms for the radiative heat loss presented here, account for the loss due to soot, H_2O and CO_2 .

Appropriate compression of the library containing source terms of soot and then radiative heat loss will limit the computational effort required.

Coupling the flamelet library to the flow code: The original procedure to introduce the flamelet library containing source terms of soot formation and radiative heat release into the flow code was mentioned before (see Section 3.3). However, in order to present the compression method applied in this work, it will be shortly explained :

1. Flamelet libraries containing source terms for the formation and oxidation of soot are calculated using the steady flamelet model. The libraries are calculated for a range of values of the radiative heat loss parameter α. The libraries are then interpolated for intermediate values of α. Flamelet libraries containing radiative heat loss are calculated.

2. (a) The Favre average of the chemical source terms stored in the flamelet libraries is given as:

$$\tilde{f}_v = \int_0^{\chi_q} \int_0^1 \frac{\rho_i}{\bar{\rho}} h(Z,\chi) \dot{f}_v(Z,\chi) \tilde{P}(Z) \tilde{P}(\chi) d\chi dZ \qquad (4.3)$$

The source terms for the radiation,stored in the flamelet libraries, must be Favre averaged as the source terms for the soot formation. This is done as follows

$$\tilde{q} = \int_0^{\chi_q} \int_0^1 \frac{\rho_i}{\bar{\rho}} h(Z,\chi) q(Z,\chi) \tilde{P}(Z) \tilde{P}(\chi) d\chi dZ \qquad (4.4)$$

where χ is assumed to be log-normal distributed and Z as a β-PDF (Equation 3.97).

(b) The Reynolds average of the density and the Favre average of mixture fraction as well as the mixture fraction variance are calculated in the CFD code.

3. (a) The enthalpy is computed by the flamelet calculations as a function of the radiative heat release parameter α:

$$\tilde{h}_\alpha = \int_0^{\chi_q} \int_0^1 h(Z,\chi) \tilde{P}(Z) \tilde{P}(\chi) d\chi dZ \qquad (4.5)$$

(b) The enthalpy h calculated in the CFD code will be used to identify the corresponding flamelet library.

4. The source terms for soot are introduced into the soot transport equations and the soot volume fraction is calculated in the flow calculations. The radiative heat loss is introduced into the energy equation in the flow code.

Coupling the compressed library to the CFD calculations: To reduce the required storage an online compression of the data can be done. The sources are fitted with polynomials along the χ axis and with β functions along the Z axis. The latter choice of the fitting procedure has the advantage that one now

is able to solve the integral of the PDF analytically as follows:

$$
\begin{aligned}
\widetilde{\dot{f}_v} &= \int_0^{\chi_q} \int_0^1 \frac{\rho_i}{\bar{\rho}} h(Z,\chi) \dot{f}_v(Z,\chi) \tilde{P}(Z) \tilde{P}(\chi) d\chi dZ \qquad (4.6) \\
&= \int_0^{\chi_q} \left(\int_0^1 \frac{\rho_i}{\bar{\rho}} h(Z,\chi) \dot{f}_v(Z,\chi) \tilde{P}(Z) dZ \right) \tilde{P}(\chi) d\chi \\
&= \int_0^{\chi_q} F^* \frac{\Gamma(\alpha^*)\Gamma(\beta^*)}{\Gamma(\alpha^* + \beta^*)} \tilde{P}(\chi) d\chi \\
&= \int_0^{\chi_q} \Phi(Z,\chi) \tilde{P}(\chi) d\chi
\end{aligned}
$$

$\Phi(Z,\chi)$ is the Favre average of the fitted distribution of the soot sources and the radiative heat loss as functions of mixture fraction and scalar dissipation. The integration of the source term over the probability might be done analytically, since a β-PDF is used for the statistical distribution of the mixture fraction (Section 3.3.2). This reduces the computational effort required for the method.

The β PDF can be replaced by normal polynomials. The result of the compression compared to the original library data is shown below.

Figure 4.20 shows the library at a boundary temperature of 298 K and atmospheric pressure for the source term of soot oxidation (i) and soot radiation (ii) as a function of mixture fraction Z and scalar dissipation rate $\log \frac{1}{\chi}$. These fields are subject of the data compression. The data field is described as functions of scalar dissipation rate and mixture fraction, temperature and pressure. First the β-function fit is applied on segments of the library at fixed values of χ. Figure 4.21 shows a comparison between the fit and the original source terms of soot oxidation (i) and the inception of soot particles (ii). The beta-function fit and the original source terms of the soot radiation (i) and the radiation due to CO_2 (ii) are shown in Figure 4.22. There is clearly a loss of information which could be diminished if an ordinary polynomial was applied. The loss of information is the trade-off for the applicability of the approach.
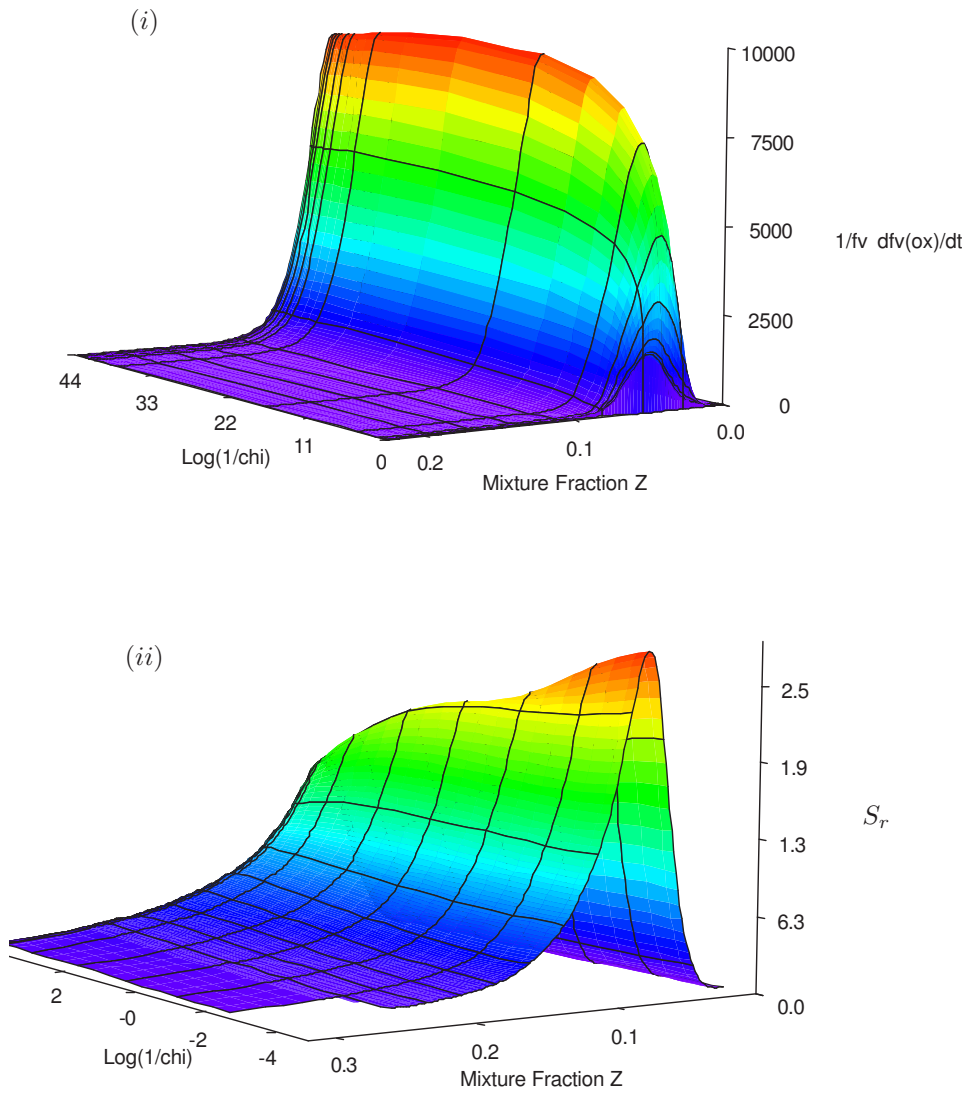
Figure 4.20: Presentation of the source term for soot oxidation (i) and the soot radiation (ii) in flamelet coordinates.
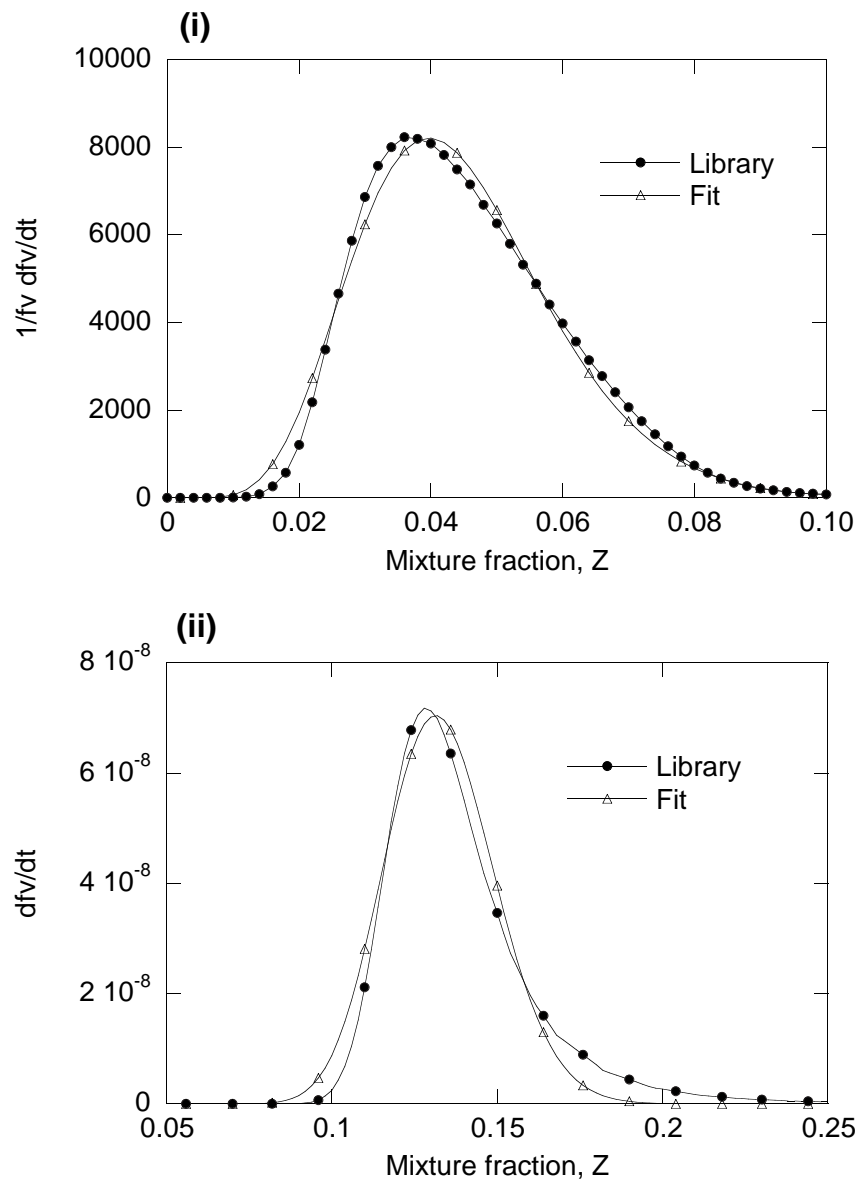
Figure 4.21: Comparison of a polynomial fit of source terms with the original data. Source term for soot oxidation (i) and particle inception (ii).
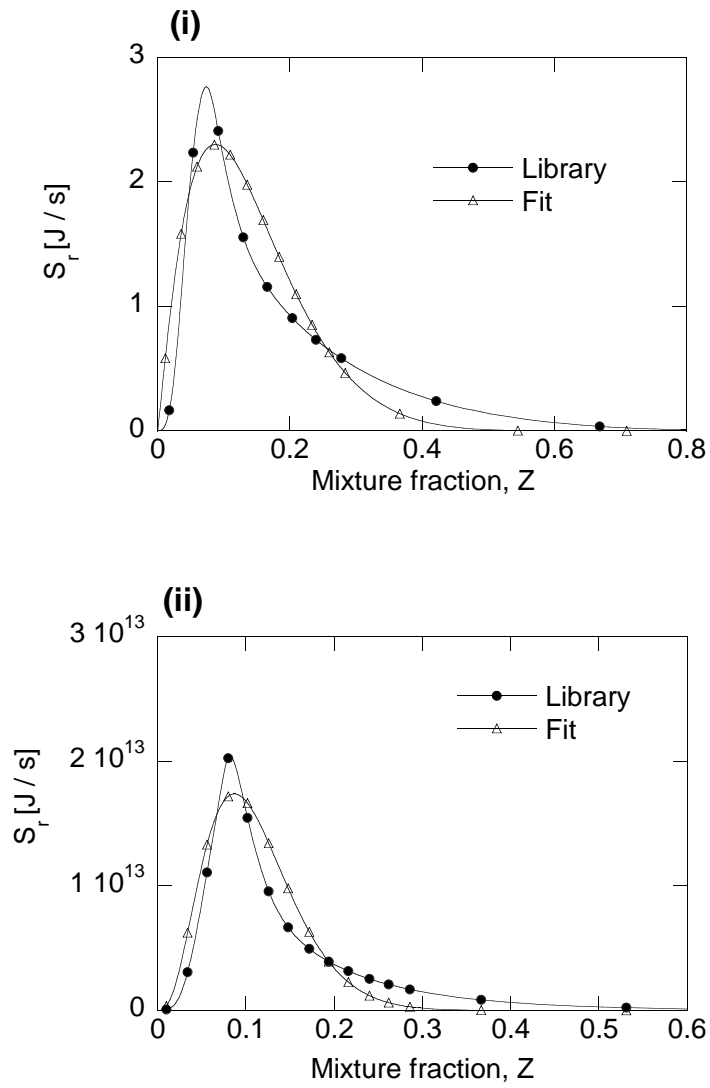
Figure 4.22: Comparison of a polynomial fit of source terms with the original data. Source term for CO_2 radiation (i) and soot radiation (ii).

Chapter 5

Conclusions

A detailed soot model has been applied in an steady and a unsteady flamelet model. The effect on soot formation in laminar and turbulent combustion of numerous features of the two approaches was studied in this work. It was shown that certain assumptions are more crucial in laminar diffusion flames than in turbulent ones.

Surface reactions: It is obvious that the surface growth of soot particles depends on the surface of the particle. The surface dependence of the particle has been shown to be more crucial in turbulent diffusion flames than in laminar flames.

The active site parameter for laminar flames is 35% of the active site parameter for turbulent flames. Soot formation in a laminar is affected much less by changes in the active site parameter than a turbulent flame. This is due to the fact that the flame is laminar and the turbulent mixing, which supplies the particle with radicals, does not affect the process. The active site parameter decreases in the absence of radicals [1].

Preferential diffusion: The diffusivity of the species was shown to play a role in soot formation. The largest effect was seen in laminar diffusion flames, where complex diffusivity of all species should be taken into account. However, complex diffusion is considered relevant for turbulent diffusion flames, where the impact of the flow field is much stronger.

Transient effects: All transient effects investigated in this work were shown to affect soot formation, which is itself transient. The first effect studied is due to heterogeneous-reactions through which the soot particles grow by reacting

with C_2H_2 or broken up by oxidation with O_2 and OH. It was shown that the consumption of these products influences the formation of soot and should be taken into account. This coupling to the gas phase affects laminar flames more, with a change of 40%. But in turbulent diffusion flames it alters the result by 30%. The steady flamelet model does allow the inclusion of this process.

The unsteady flamelet model was shown to achieve results that agreed better with experiments and exhibited better convergence than the steady flamelet model.

Although some of those effects such as the coupling to the gas phase cannot be included in the steady flamelet approach, reasonable results could still be obtained when modelling soot volume fraction.

Formation of agglomerates: The process of the formation of agglomerates was included in the unsteady model and applied to a laminar acetylene/nitrogen/air diffusion flame. It was shown that the soot volume fraction is affected when this process is considered. The predictions of the model including the agglomeration are closer to the experimental profile than the model neglecting the formation of agglomerates.

Methods of reduction: Online mechanism reduction and the removal species with short lifetimes was included in the unsteady flamelet code. It was possible to filter the Jacobian down to one third of the species. However, this method is not considered very useful for modelling soot formation since the CPU time increases due to convergence problems. If CPU time must be reduced it is much more convenient to apply compression of the library when coupling the information generated with the steady flamelet model to the flow code.

Chapter 6

There is much more to do

Despite the fact that many model parameters have been studied in this thesis, a large number of questions remain to be answered. They will be posed in this last chapter and hopefully answered in future work.

Surface reactions: As soon as agglomerates are formed only part of the surface of the particle is exposed and available for reactions with the gas phase species, such as the species assumed to be responsible for growth, C_2H_2, and the species responsible for oxidation, O_2 and OH. Since the fractal surface is much larger than the spherical surface this should effect heterogenous reactions and thereby surface growth and oxidation of soot agglomerates. The fractality of the particles should even have an influence on the activity of the soot sites. Appel et al. [122] described the relation between the active site parameter and temperature in premixed flames. This relation should be investigated for laminar and turbulent diffusion flames.

Preferential diffusion: The effect of preferential diffusion on soot formation could be shown in this work. It is to be expected that this effect is also relevant for soot formation when agglomerates are formed.

Formation of agglomerates: Agglomerates have been included in the unsteady flamelet model and validated against the laminar acetylene flame. It would be interesting to validate the model against a turbulent flame in the future.

   The laminar flamelet model for agglomerates must be tested in all three regimes: the free molecular regime, the continuum regime and the transition regime. This implies that the model should be tested at higher pressures.

143

Fuchs [124] solution for the transition regime should be validated against the simple solution presented by Frenklach et al. [106] using the flamelet model in diffusion flames.

Methods of reduction: With increasing CPU power the demand on the accuracy of the models and of joint physical and chemical models will increase. The need to save CPU time will always be present, although at the cost of a loss in accuracy. This poses a mathematical and numerical challenge to develop methods of reduction which really save computational time and not increase the CPU time due to enlarged convergence problems.

Publications

This dissertation is based on the following publications, contributions at conferences and meetings:

1. A.S. Dederichs, M. Balthasar, F.Mauss and X.-S. Bai, The Formation of Soot in Non-Premixed Combustion Using Different Flamelet Models, in *Survey of Combustion Research in Sweden*, Gothenburg, p. 207-212 (1998).

2. A.S. Dederichs, M. Balthasar, F.Mauss and X.-S. Bai, "Pollutant Formation in Non-Premixed Combustion Using Different Flamelet Models", in *Proceedings of the 17th ICDERS*, Heidelberg (1999)

3. A.S. Dederichs, M. Balthasar, F.Mauss and X.-S. Bai, "Pollutant Formation in Turbulent Diffusion Flames Using the Laminar Flamelet Concept", in *Proceedings of the Joint Meeting of the British, German and French Sections of the Combustion Institute*, Nancy, p.17 (1999)

4. A.S. Dederichs, M. Balthasar, F.Mauss, Modelling of Soot and NO_x Formation in Diesel Combustion, in *Oil & Gas Science and Technology* , 54 (No.2), pp. 245-250 (1999)

5. A.S. Dederichs, M. Balthasar, F.Mauss, The Modelling of Transient Effects in Laminar Flamelets, in *Combustion Technologies for a Clean Environment* , Vol 5 within the book series: "Energy, Combustion and the Environment" (1999).

6. A.S. Dederichs, M. Balthasar, F.Mauss and X.-S. Bai, The Formation of Soot and NOx in non-premixed Combustion Using Different Flamelet Models. 27th Symposium (International) on Combustion, Boulder 1998

7. Modelling of transient effects in turbulent diffusion flames Anne S. Dederichs, Raffaella Bellanca and Fabian Mauss, 27th Symposium (International) on Combustion, Edinburgh 2000.

145

8. Anne S. Dederichs, Fikret Saric, Fabian Mauss, "Inclusion of the interface for adaptive chemistry into the Lund code for interactive flamelets", EU-Meeting, Paris 2001

Acknowledgements

First I would like to thank my supervisor, Professor Göran Holmstedt, without whom I can truly say this thesis would never have been completed. He gave me the best supervision I could have wished for. His backup in difficult times and his feedback have been essential for this work. Thanks to Xue Song Bai, Helen Brocklehurst and Fikret Saric with whom I had enjoyable collaboration. Thanks to Zhenghua Yan and especially to Helen Sheppard for reading this thesis. Margareta Rosén was a great help with getting hold of literature. I am greatly indebted to Susanna Persson, who guided me through rough times.

On a more personal note: The person who awoke my interest in math and science was my committed teacher Alfred Ströher. I want to thank my colleagues during the years - my friends from the Department of Fire Safety Engineering - especially Berit Andersson for her encouragement, Robert Jönsson for distracting me once in a while with inspiring questions and my roommate Daniel Nilsson giving me good advice in moments of confusion.

Thanks to all my friends. I am indebted to my mother Christa, who has been my inspiration in life, and my dear sister Alexa. I am most grateful to my family: Joachim, for his love and active support and our son, Nathan, for introducing me to the miracle of life.

Bibliography

[1] Haynes, B.S.; Wagner H. GG., "Soot formation," *Progress in Energy and Combustion Science*, vol. 7, pp. 229–273, 1981.

[2] Energy Quest, Ed., *Energy History*, California Energy Commission, 2003.

[3] Empedokles, "Rhizômata," *Katharmoi*, c.484-c.424 BCE.

[4] World energy council, "Survey of energy resources," 2001.

[5] Mannion, A. M.; Bowlby, S. R., Ed., *Environemental issues in the 90's*, Wily, 2 edition, 1992.

[6] Eltjo Buringh and Antoon Opperhuizen, Eds., *On health risks of ambient PM in the Netherlands*, RIVM report 650010 032. Netherlands Aerosol Programme, 2002.

[7] Jacobson, M. Z., "Control of fossil-fuel particulate black carbon and organic matter, possibly the most effective method of slow global warming," *Journal of Geophysical Research*, vol. 107, pp. 4410, 2002.

[8] Menon, S.; Hansen, J.; Nazarenko, L.; Luo, Y., "Climate effects of black carbon aerosols in china and india," *Science*, vol. 297, pp. 2250–2253, 2002.

[9] Jacobson, M. Z., "Strong radiative heating due to the mixing state of black carbon in atmospheric aerosols," *Nature*, vol. 409, no. 6821, pp. 695, 2001.

[10] Signed by 55 countries, *Kyoto Protocoll: United Nations Framework Convention on Climate Changes*, United Nations, 1997.

[11] Dockery, D.W., "Epidemiologic evidence of cardiovascular effects of particulate air pollution," *Environmental Health Perspectives*, vol. 109, pp. 483 486, 2001.

[12] Linville, J.L., Ed., *Handbook of Fire Protection Engineering*, National Fire Protection Association, 2 edition, 1995.

[13] Orloff, L.; De Ris, J.; Markstein, G.H., "Upward turbulent fire spread and bruning of fuel surface," in *Fifteenth Symposium (International) on Combustion, Combustion Institute*, 1974, pp. 183–192.

[14] Carlsson, J., "Computational strategies in flame-spread modelling involving wooden surfaces," Tech. Rep., Department of Fire Safety Engineering, Lund University, Sweden, 2003.

[15] Frenlach, M.; Feigelson, E.D., "Soot in flames and iterstellar dust," *Earth and Mineral Sciences*, vol. 58, no. 2, pp. 25–30, 1989.

[16] Frenklach, M., "Reduction of chemical reaction models," *Chem. Ing. Sc.*, vol. 40, pp. 1842, 1985.

[17] Anonymos, "Carbon black faces long-term challenges but benefits from a strengthening us economy," *Chemical Market Reporter*, vol. 265, pp. 13, 2004.

[18] De Ris, J., "Prediction of fire dynamics," *US Department of Commerce, Building and Fire Research Laboratory, NIST-GCR-97-729*, vol. 0, pp. 0–40, 1997.

[19] Lindstedt, P.D., *A simple reaction mechanism for soot formation in non-premixed flames*, Springer Verlag Berlin, 1992.

[20] Black, D.L.; McQuay, M.Q.; Bonin, M.P., "Laser-based techniques for particle-size measurement: A review of sizing methods and their industrial applications," *Progress in Energy and Combustion Science*, vol. 22, pp. 267–306, 1996.

[21] Mountain, R.D.; Mulholland, G.W., "Light scattering from simulated smoke agglomerates," *Langmuir*, vol. 4, pp. 1321–1326, 1988.

[22] Köylü, Ü.Ö.; Xing, Y.; Rosner, D.E., "Fractal morphology analysis of combustion generated aggregates using angular light scattering and electron mircoscope images," *Langmuir*, vol. 11, pp. 4848–4854, 1995.

[23] Bonczyk, P.A.; Hall, R.J., "Fractal propperties of soot agglomerates," *Langmuir*, vol. 7, pp. 1274–1280, 1991.

[24] Hanson, R.K., "Recent advances in laser-based combustion diagnostics," in *Aerospace Science Meeting and Exhibit*, 1997, vol. 35, p. 115, AIAA-97-0115.

[25] Allain, L.R.; Stratis, D.N.; Cullum, B.M.; Mobley, J.; Hajaligol, M.R.; Vo-Dinh, T., "Real-time detection of pah mixtures in the vapor phase at high temperatures," *Journal of Analytical and Applied Pyrolysis*, vol. 66, pp. 145–154, 2002.

[26] Sutton, J.A.; Driscoll, J., "Scalal dissipation rate measured in flames - a method to improve spatial resolution by using nitric oxid plif," in *Twenty-Ninth Symposium (International) on Combustion*. The Combustion Institute, Pittsburgh, 2002, p. 1743.

[27] Su, L.K, "Measurements of the three-dimensional scalar dissipation rate in gas-phase planar turbulent jets," Tech. Rep., Center for Turbulence Research, Stanford University, 1998.

[28] Axelsson, B.; Collin, R.; Bengtsson, P.-E., "Laser-induced incadescence for soot particle size and volume fraction measurements using on-line extinction calibration," *Applied Physics B*, vol. 72, pp. 367–372, 2001.

[29] Walewski, J.; Rupinski, M.; Bladh, H.; Li, Z.S.; Bengtsson, P.-E.; Aldén, M., "Soot visualisation by use of laser-induced soot vaporisation in comination with polarisation spectroscopy," *Applied Phsysics B*, vol. 77, pp. 447–454, 2003.

[30] Zhang, H.X.; Sorensen, C.M.; Ramer, E.R.; Olivier, B.J.; Merklin, J.F., "In situ optical structure factir measurements of an aggregating soot aerosol," *Langmuir*, vol. 4, pp. 867–871, 1988.

[31] Kim, C.H. ; El-Leathy, A.M. ; Xu,F. ; Faeth, G.M, "Soot surface growth and oxidation in laminar diffusion flames at pressures of 0.1-1.0 atm," *Combustion and Flame*, vol. 136, pp. 191–207, 2004.

[32] Xu,F. ; Kim, C.H. ; El-Leathy, A.M. ; Faeth, G.M, "Soot surface oxidation in hydrocarbon/air diffusion flames at atmospheric pressure," *Combustion and Flame*, vol. 132, pp. 43–57, 2003.

[33] Xu,F. ; Faeth, G.M, "Soot formation in laminar acetylene/air diffusion flames at atmospheric pressure," *Combustion and Flame*, vol. 125, pp. 804–819, 2001.

[34] Lin, K.-C.; Sunderland, P.B.; Faeth, G.M, "Soot nucleation and growth in acetylene air laminar coflowing jet diffusion flames," *Combustion and Flame*, vol. 105, pp. 369–375, 1996.

[35] Köylü, U.O. ; Faeth, G.M; Farias, T.L.; Carvalho, M.G., "Fractal and projected structure properties of soot aggregates," *Combustion and Flame*, vol. 100, pp. 621–633, 1995.

[36] Nichols, E. L., "On the temperature of the acetylene flame," *Physical Review (Series I)*, vol. 10, pp. 234252, 1900.

[37] Li, J. ; Khan, A.J. ; Husain, L., "A technique for determination of black carbon in cellulose filters," *Atmospheric Environment*, vol. 36, pp. 4699–4704, 2002.

[38] Yang, X.; Yang, J.M.; Wang, X.Q.; Meng, E.; Tai, Y.C.; Ho, C.M., "Micro machined membrane particle filters," in *The Eleventh Annual International Workshop on Micro Electro Mechanical Systems*. IEEE, 1998, pp. 137–142.

[39] Richards, L.W. ; Alcorn, S.H. ; McDade, C. ; Couture, T. ; Lowenthal, D. ; Chow, J.C. ; Watson, J.C., "Optical properties of the san joaquin valley aerosol collected during the 1995 integrated monitoring study," *Atmospheric Environment*, vol. 33, pp. 4787–4795, 1999.

[40] Yamamoto, H.; Masuda, S., "Electrostatic separation of cvd ultra-fine particles at high temperature," in *Industry Applications Society Annual Meeting*. IEEE, 1992, pp. 1551–1554.

[41] De Loggio, Th. J. ; Letki, A. G., "New directions in centrifuging," *Chemical Engineering*, vol. 101, pp. 70–77, 1994.

[42] Choudhuri, A.R.; Gollahalli, .SR., "Measurement of oh concentrations in turbulent diffusion flames usind combined lif and raman spectroscopy," *AIAA*, vol. AIAA-2000-3001, pp. 1137–1146, 1999.

[43] Starner, S.H.; Bilger, R.W.; Frank, J.H.; Marran, D.F.; Long, M.B., "Mixture fraction imaging in a lifted methane jet flame," *Combustion and Flames*, vol. 107, pp. 307–313, 1996.

[44] Choi, M.Y.; Mulholland, G.W.; Hamins, A.; Kashiwagi, T., "Comparisons of the soot volume fraction using gravimetric and light extinction techniques," *Combustion and Flame*, vol. 102, pp. 162–169, 1995.

[45] Megaridis, C.M.; Dobbins, R.A., "Absorption and scattering of light by polydispere aggregates," *optical Society of America*, pp. 4747–4754, 1991.

[46] McEnally, C.S.; Schaffer, A.M.; Long, M.B.; Pfefferle, L.D.; Smooke, M.D.; Colket, M.B.; Hall, R.J., "Computational and experimental study of soot formation in a coflow, laminar ethylene diffusion flame," in *Twenty-Seventh Symposium (International) on Combustion*. The Combustion Institute, Pittsburgh, 1998, pp. 1497–1505.

[47] Bressloff , N. W. ; Moss, J. B.; Rubini , P. A., "Cfd prediction of coupled radiation heat transfer and soot production in turbulent flame," in *Twenty-Sixth Symposium (International) on Combustion*. The Combustion Institute, Pittsburgh, 1996, pp. 2379–2386.

[48] Moss, J.B.; Steward, C.D.; Syed, K.J., "Flow field modelling of soot formation at elevated pressures," in *Twenty-Second Symposium (International) on Combustion*. The Combustion Institute, Pittsburgh, 1988, pp. 413–423.

[49] Young, K.J.; Steward, C.D.; Moss, J.B., "Soot formation on cvonfined turbulent flames fuelled by pre-vaporized kerosine and by ethylene," in *Proceedings of the Tenth International Symposium on Air breathing Engines*, 1991, pp. 239–248.

[50] Young, K. J. ; Moss, J. B., "Modelling sooting turbulent jet flames using an extended flamelet technique," *Combustion Science and Technology*, vol. 105, pp. 33–53, 1995.

[51] Warnatz, J.; Maas, U.; Dibble, R. W., Ed., *Verbrennung*, Springer Verlag, 2 edition, 1996.

[52] Turns, S. , *Introduction to Combustion*, Pennsylvania State University, Us, 2 edition, 1996.

[53] Glasmann, I., *Combustion*, Academic Press, 3 edition, 1996.

[54] Chomiac, J., Ed., *Turbulence reacting flows*, Chalmers University of Technology, 3 edition, 2000.

[55] Maas, U.; Pope, S.B., "Simplifying chemical kinetics: Intrinsic low-dimensional manifolds in composition space," *Combustion and Flame*, vol. 88, pp. 239–264, 1992.

[56] Peters, N., *Turbulent Combustion*, Cambridge Monographs on Mechanics, 2000.

[57] Rubini, P., "An introduction to turbulence physics," *personal communications*, 2003.

[58] Peters, N., "The turbulent burning velocity for large-scale and small-sclae turbulence," *Journal of Fluid Mechanics*, vol. 384, pp. 107–132, 1999.

[59] Group of Experts OECD Nuclear Energy Agency, Ed., *Flame Acceleration and Deflagration to Detonation Transition in Nuclear Safety*, DCW Industries, Inc., La Canada, CA, 2 edition, 1998.

[60] Wilcox, D.C., *Turbulence Modeling for CFD*, DCW Industries, Inc., La Canada, CA, 2 edition, 1998.

[61] Kolmogororv, A.N., "Equations of turbulent motion of an incompressible fluid," *Physics*, vol. 6, pp. 56–58, 1942, Izvestia Academy of Science.

[62] Saffman, P.G., "A model for inhomogeneous turbulent flow," *Proceedings of the Royal Society of London*, vol. A317, pp. 417–433, 1970.

[63] Smith, B.R., "A new wall model for the k-l two equation turbulence model," *IAA Paper*, p. 2386, 1994.

[64] Launder, B. E.; Priddin,C. H. ; Sharma, B. I., "The calculation of turbulence boundary layers on spinning and curved surfaces," *Transactions of the ASME, Journal of Fluids Engineering*, vol. 99, pp. 231–238, 1977.

[65] Poinsot, T.J.; Veyante,D.; Candel,S., "Quenching process and premixed turbulent combustion diagrams," *Journal of Fluid Mechanics*, vol. 228, pp. 561–606, 1991.

[66] de Bruyn Kops, S.M., *Numerical Simulation of Non-premixed Turbulent Combustion*, Ph.D. thesis, University of Washington, 1999.

[67] Pitsch, H., "Extended flamelet model for les of non-premixed combustion," Tech. Rep., Stanford Univeristy, 2000.

[68] Bilger, R. W., "The structure of diffusion flames," *Combustion Science and Technology*, vol. 13, pp. 155, 1976.

[69] Spalding, D. B. , "A model for inhomogeneous turbulent flow," in *Thirteenth Symposium (International) on Combustion*. The Combustion Institute, Pittsburgh, 1970, p. 649.

[70] Tang, Q.; Xu, J.; Pope, S. B., "Pdf calculations of local extinction and no production in piloted-jet turbulent methane/air flames," in *Twenty-eighth Symposium (International) on Combustion*, 2000, 24, pp. 133–139.

[71] Girimaji, S.S., "On the modeling of scalar diffusion in isotropic turbulence," *Phys. Fluids A*, vol. 4(11), pp. 2529–2537, 1992.

[72] Kim, S.H.; Huh, K.Y.; Bilger, R. W., "Second-order conditional moment closure of local extinction and reignition in turbulent nonpremixed hydrocarbon flames," in *Twenty-Ninth Symposium (International) on Combustion*. The Combustion Institute, Pittsburgh, 2002, p. 595.

[73] Cha, C.M.; Kosaly, G.; Pitsch, H., "Modeling extinction and reignition in turbulent nonpremixed combustion using a doubly-conditional moment closure approach," *Phys. Fluids*, vol. 13(12), pp. 3824–3834, 2001.

[74] Klimenko, A.Y.; Bilger, R. W., "Conditional moment closure for turbulent combustion," *Progress in Energy and Combustion Science*, vol. 25, pp. 595–687, 1999.

[75] Steiner, H.; Bushe W.K., "Large eddy simulation of a turbulent reacting jet with conditional soure-term estimation," *Physics of Fluids*, vol. 11(7), pp. 1896, 1999.

[76] Williams, F.A., *Description of Turbulent Diffusion Flames*, Plenum Press, 1 edition, 1975.

[77] Peters, N., "Laminar diffusion flamelet models in non-premixed turbulent combustion," *Progress in Energy and Combustion Science*, vol. 10, pp. 319, 1984.

[78] Pitsch, H.; Chen, M. ; Peters, N. , "Unsteady flamelet modeling of turbulent hydrogen-air diffusion flames," in *Twenty-Seventh Symposium (International) on Combustion*. The Combustion Institute, Pittsburgh, 1998, p. 1057.

[79] Lahaye; J.; Prado; G., *In: Particulate Carbon Formation During Combustion*, chapter Morphology and Internal Structure of Soot and Carbon Blacks, Plenum Press, 3 edition, 1981.

[80] McKinnon, J.T.; Howard, J.B., "The roles of pah and acetylene in soot nucleation and growth," in *Twenty-Fourth Symposium (International) on Combustion*. The Combustion Institute, Pittsburgh, 1992, pp. 965–971.

[81] Hindsgaul, C.; Schramm, J.; Gratz, L.; Henriksen, U.; Bentzen, J.D., "Physical and chemical characterization of particles in producer gas from wood chips," *Bioresource Technology*, vol. 73, pp. 147–155, 2000.

[82] Megaridis, C.M.; Dobbins, R.A., "Soot aerosol dynamics in a laminar ethylene diffusion flame," in *Twenty-Second Symposium (International) on Combustion*. The Combustion Institute, Pittsburgh, 1988, pp. 353–362.

[83] Kennedy, I .M., "Models of soot formation and oxidation," *Progress in Energy and Combustion Science*, vol. 23, pp. 95, 1997.

[84] Calcote, H.F.; Manos, D.M., "Effect of molecular structure on incipient soot formation," *Combustion and Flame*, vol. 49, pp. 289, 1983.

[85] Gill, R.J.; Olson, D.B., "Estimation of soot thresholds for fuel mixtures," *Combustion Science and Technology*, vol. 40, pp. 307–315, 1984.

[86] Takahashi, F.; Glassman, I., "Sooting correlations for premixed flames," *Combustion Science and Technology*, vol. 37, pp. 1–19, 1984.

[87] Kahn, I.M.; Greeves, G.; Probert, D.M., "?," *Air Pollution Control in transport Engines*, vol. C142/71, pp. 205–217, 1971, The Institution of Mechanical Engineers, London.

[88] Lefebvre, A., "Flame radiation in gas turbine combustion chambers," *Int. J. Heat and Mass Transfer*, vol. 27, pp. 1493–1510, 1984.

[89] Tesner, P.A.; Snegiriova, T.D.; Korre, V.G., "Kinetics of dispersed carbon formation," *Combustion and Flame*, vol. 17, pp. 253–260, 1997.

[90] Tesner, P.A; Tsygankova, E.I.; Guilazetdinov, E.I.; Zuyev, V.P.; Loshakova, G.V., "The formation of soot from aromatic hydrocabons in diffusion flames of hydrocarbon-hydrogen mixtures," *Combustion and Flame*, vol. 17, pp. 279, 1971.

[91] Surovikin,V.F., "Analytical description of the process of nucleus-formation and growth of particles of carbon black in the thermal decomposition of aromatic hydrocarbons in the gas phase," *Khimiya Tverdogo Topliva*, vol. 10, pp. 111–122, 1976.

[92] Magnussen, B.F; Hjertager, B.H.; Olsen, J.G.; Bhaduri, D., "Effects of turbulent structure and local concnetrations on soot formation and combustion in c_2h_2 diffusion flames," in *Sixteenth Symposium (International) on Combustion*. The Combustion Institute, Pittsburgh, 1976, p. 719.

[93] Brown, A.J.; Heywood, J.B., "A fundamentally-based stochastic mixing model methos for predicting *no* and soot emissions from direct injection diesel engines," *Combustion Science and Technology*, vol. 58, pp. 195–207, 1988.

[94] Jensen, D.E., "Prediction of soot formation rates: a new approach," 1974.

[95] Graham, S.C., "The modelling of the growth ofsoot particles during the pyrolysis and partial oxidation of aromatic hydrocarbons," 1981.

[96] Mulholland, G.W., "Global soot growth model," *Fire safety science*, pp. 709–718, 1986.

[97] Young, K.J.; Steward, C.D.; Moss, J.B., ," in *Twenty-Fifth Symposium (International) on Combustion*, 1994.

[98] Syed, K. J.; Steward, C.D.; Moss, J.B., "Modelling soot formation and thermal radiation in buoyant turbulent diffusion flames," in *Twenty-Third Symposium (International) on Combustion*. The Combustion Institute, Pittsburgh, 1992, pp. 1533–1541.

[99] Fairweather, M.; Jones, W.P.; Lindstedt, P., "Predictions of radiative transfer from turbulent reacting jet in a cross-wind," *Combustion and Flame*, vol. 89, pp. 45–63, 1992.

[100] Fairweather, M.; Jones, W.P.; Ledin, H.S.; Lindstedt, P., "Predictions of soot formation in turbulent non-premxed propane flames," in *Twenty-Fourth Symposium (International) on Combustion*. The Combustion Institute, 1992, pp. 1067–1074.

[101] Harris, S.J. ; Kennedy, I.M., "The coagulation of soot particles with van der waals forces," *Combustion Science and Technology*, vol. 59, pp. 443–454, 1988.

[102] Nagel, J.; Strickland-Constable, R.F., *Fifth Carbon Conference*, vol. 1, Pergamon Oxford, 1962.

[103] Smooke, M.D.; Puri, I.K.; Seshadri, K., "A comparison between numerical calculations and experimental measurements of the structure of a counterflow diffusion flame burning diluted methane in diluted air," in *Twenty-First Symposium (International) on Combustion*. The Combustion Institute, Pittsburgh, 1986, pp. 1783–1792.

[104] Frenlach, M.; Wang, H., "Detailled modelin of soot particle nucleation and growth," in *Twenty-Third Symposium (International) on Combustion*. The Combustion Institute, Pittsburgh, 1990, p. 1559.

[105] Kollmann, W.; Kennedy,I. M.; Metternich, M.; Chen, J.-Y., *Soot Formation in Combustion - Mechanisms and Models*, Springer Verlag, Berlin-Heidelberg, 1 edition, 1994.

[106] Kazakov, A.; Frenklach, M., "Soot particle coagulation and aggregation," *Combustion and Flame*, vol. 114, pp. 484–501, 1998.

[107] Gut, A., *An Intermediate Course in Probability*, Springer Verlag, Berlin-Heidelberg, 1 edition, 1995.

[108] Mauss, F., *Entwicklung eines kinetischen Modells der Russbildung mit schneller Polymerisation*, Ph.D. thesis, RWTH Aachen, 1997.

[109] Bittner, J.D.; Howard, J.B., "Composition profiles and reaction mechanisms in a near sooting promixed benzenze/oxygene/argon flame," in *Eighteenth Symposium (International) on Combustion*. The Combustion Institute, Pittsburgh, 1980, p. 1105.

[110] Miller, J.H., "The kinetics of polynuclear aromatic hydrocarbon agglomeration in flames," in *Twenty-Third Symposium (International) on Combustion*. The Combustion Institute, Pittsburgh, 1990, p. 91.

[111] Miller, J.H.; Smyth, K.C.; Mallard, W.G., "Calculations of the dimerization of aromatic hydrocarbons: Implications for soot formation," in *Twentieth Symposium (International) on Combustion*. The Combustion Institute, Pittsburgh, 1984, p. 1139.

[112] Harris, S.J.; Weiner, A.M., "A picture of soot particle inception," in *Twenty-Second Symposium (International) on Combustion*. The Combustion Institute, Pittsburgh, 1988, pp. 333–342.

[113] Slagle, I.R.; Park, J.Y.; Heaven, M.C.; Gutman, D.J., "?," *J. Am. Chem. Soc.*, vol. 82, pp. 151, 1984.

[114] Westmoreland, P.R., "Thermochemistry and kinetics of $c_2h_4 + o_2$ reactions," *Combustion Science and Technology*, vol. 82, pp. 151, 1992.

[115] Chiang, H.M.; Lay, T.H.; Bozelli, J.W., "Kinetic modeling: High pressure propane oxidation: Comparison with experiment," in *Fall Technical Meeting of the Eastern States Section of the Combustion Institute, Worcester*, 1995.

[116] Balthasar, M., *Detailled Soot Modelling in Turbulent Diffusion Flames*, Ph.D. thesis, Lund University, 2000.

[117] Frenlach, M.; Harris, S.J., "Aerosol dynamics modeling using the method of moments," *Journal of Colloid Interface Sciences*, vol. 118, pp. 252, 1987.

[118] Wagner, H. Gg., *Soot in Combustion Systems and its Toxic Properties*, Plenum Press, New York, 1983.

[119] Harris, S.J.; Weiner, A.M., "Surface grwoth of soot particles in premixed ethylene/air flames," *Combustion Science and Technology*, vol. 31, pp. 155, 1983.

[120] Mauss, F.; Trilken, B.; Breitbach , H.; Peters, N., *Soot Formation in Combustion - Mechanisms and Models*, Springer Verlag, Berlin-Heidelberg, 1 edition, 1994.

[121] Frenlach, M.; Wang, H., *Detailed Mechanism and Modeling of Soot Particle Formation*, Springer Verlag, Berlin-Heidelberg, 1 edition, 1994.

[122] Appel, J.; Bockhorn, H.;Frenlach, M., "Kinetic model of soot formation with detailed chemistry and physics: Laminar premixed flames of c_2 hydrocarbons," *Combustion and Flame*, vol. 121, pp. 122–136, 2000.

[123] Harris, S.J. ; Kennedy, I.M., "Soot particle aerosol dynamics at high pressure," *Combustion and Flame*, vol. 78, pp. 390–397, 1989.

[124] Fuchs, N.A., Ed., *Mechanics of Aerosols*, Pergamon New York, 1 edition, 1964.

[125] Pratsini, S.E., "Simultsneous nucleation, condensation and coagulation in aerosols reactors," *Journal of Colloid and Interface Science*, vol. 124, pp. 416–427, 1987.

[126] Samson, R.J.; Mulholland, G.W.; Gentry, J.W., "Structural analysis of soot agglomerates," *Langmuir*, vol. 3, pp. 272–281, 1987.

[127] Mulholland, G.W.; Samson, J.R.; Mountain, R.D .; Gentry, J.W., "Cluster size distribution for free molecular and continuum flow regimes," *Energy Fuels*, vol. 2, pp. 481–486, 1988.

[128] Dobbins, R.A.; Fletcher, R.A.; Lu, W., "Laser microprobe analysis of soot precursor particles and carbonaceous soot," *Combustion and Flame*, vol. 100, pp. 301–309, 1995.

[129] Cai, J.; Lu, N.; Sorensen, C.M., "Analysis of fractal cluster morphology parameters: Structural coefficient and density autocorrelation function cutoff," *Journal of Colloid and Interface Science*, vol. 171, pp. 470–473, 1995.

[130] Mountain, R.D.; Mulholland, G.W.; Baum, H., "Simulation of aerosol agglomeration in the free-molecular and continuum flow regimes," *J. Colloid Interface Sci.*, vol. 114, pp. 67, 1986.

[131] Mandelbrot, B.B., *The Fractal Geometry of Nature*, Freeman, New York, 1 edition, 1983.

[132] Dobbins, R.A.; Santorro, R.J.; Semeerjian, H.G., "Analysis of light scattering from soot using optical cross sections for aggregates," in *Twenty-Third Symposium (International) on Combustion, Combustion Institute*, 1991, pp. 1525–1532.

[133] Rogak, S.N.; Flagan, R.C.; Nguyen, H.V., "The mobility and structure of aerosol agglomerates," *Aerosol Science and Technology*, vol. 18, pp. 25–47, 1993.

[134] Kruis, F.E.; Kusters, K.A.; Pratsinis, S.E., "A simple model for the evolution of the characteristics of aggregate particles undergoing coagulation and sintering," *Aerosol Science and Technol*, vol. 19, pp. 514–526, 1993.

[135] Pels Leusden, C., *Experimentelle und Theoretische Untersuchung der Rußbildung in Laminaren Gegenstromflammen, Ph.D. Thesis*, Ph.D. thesis, RWTH Aachen, 2001.

[136] Hirschfelder, J.O. ; Curtiss, C.F., "Transport properties of multicomponent gas mixtures," in *Symposium on Combustion and Flame and Explosion Phenomena*, 1949, p. 121.

[137] Rosner, D.E.; Mackowski, D.W.; Garcia-Ybarra, P., "Size- and structure-intensivity of thermophoretic transport of aggregated "soot" particles in gases," *Combustion Science and Technology*, vol. 80, pp. 87–101, 1991.

[138] Paul, P.H.; Warnatz, J., "A re-evaluation of the means used to calculate transport properties of reacting flows," in *Twenty-Fifth Symposium (International) on Combustion*. The Combustion Institute, Pittsburgh, 1998, pp. 495–504.

[139] Rosner, D.E.; Israel, R.S.; La Mantia, B., ""heavy" species ludwig-soret transport effects in air-breathing combustion," *Combustion and Flame*, vol. 123, pp. 547–560, 2000.

[140] Pitsch, H., *Modellierung der Zündung und Schadstoffbildung bei der dieselmotorischen Verbrennung mit Hilfe eines interaktiven Flamelet-Modelles, Ph.D. Thesis*, Ph.D. thesis, RWTH Aachen, 1998.

[141] Veyante, D.; Vervisch, L., "Turbulent combustion modeling," *Progress in Energy Science*, vol. 28, pp. 193–266, 2002.

[142] Kim, J. S.; Williams, F. A., "Structures of flow and mixture fractionfields for counterfow diffusion flames with small stoichiometric mixture," *SIAM J. Appl. Math.*, vol. 53, pp. 1551–1566, 1993.

[143] Pope, S.B. , "Df methods for turbulent reactive flows," *Progress in Energy and Combustion Science*, vol. 11, pp. 119–192, 1985.

[144] Bai, X.S.; Fuchs, L., "Sensitivity study of turbulent reacting flow modeling in gas turbine combustors.," *AIAAJ.*, vol. 33, pp. 1857–1864, 1995, No.10.

[145] De Ris, J.; Orloff, L., "The role of buoyancy direction and radiation in turbulent diffusion flames on surfaces," in *Fifteenth Symposium (International) on Combustion, Combustion Institute*, 1974, pp. 175–182.

[146] Leung K.M.; Lindstedt, P.D.; Jones, W.P., "A simplified reaction mechanism for soot formation in nonpremixed flames," *Combustion and Flame*, vol. 87, pp. 289–305, 1991.

[147] De Ris, J., "Upward turbulent fire spread and bruning of fuel surface," in *Seventeenth Symposium (International) on Combustion, Combustion Institute*, 1979, pp. 1003–1016.

[148] Saric, F.; Dederichs, A.S., "Automatic reduction of chemical mechanisms applied to rif calculations," *To be published*, 2004.

[149] X. Zhou, "Wavelets-galerkin scheme for a stokes problem," *Numerical Methods for Partial Differential Equations*, vol. 20, pp. 193–198, 2002.

[150] Pope, S.B., "Computationally efficient implementation of combustion chemistry using in situ adaptive tabulation," *Combustion and Flame*, vol. 1, pp. 41–63, 1997.

[151] Chen, J.-Y.; Blasco, J.A. ; Fueyo N. ; Dopazo, C., "An economical strategy for storage of chemical kinetics: Fitting in situ adaptive tabulation with artificial neural networks," in *Twenty-Eighth Symposium (International) on Combustion.* The Combustion Institute, Pittsburgh, 2000, pp. 1–10.

[152] Friedman, J. H., "Multivariate adaptive regression splines," *Annals of Statistics*, vol. 19, pp. 1–67, 1991.